



Expedition 395 methods¹

Contents

- 1 Introduction
- 10 Lithology
- 16 Igneous petrology
- 23 Alteration petrology and structural geology
- 25 Micropaleontology
- 33 Physical properties
- 39 Stratigraphic correlation
- 42 Paleomagnetism
- 47 Geochemistry and microbiology
- 56 Downhole measurements
- 66 Age model
- 67 References

Keywords

International Ocean Discovery Program, IODP, *JOIDES Resolution*, Expedition 395, Expedition 384, Expedition 395C, Reykjanes Mantle Convection and Climate, Earth Connections, Earth in Motion, Site U1554, Site U1555, Site U1562, Site U1563, Site U1564, Site U1602, contourite drifts, mantle plume, hydrothermal alteration, oceanic gateways, climate record, Northern Hemisphere glaciation

Core descriptions

Supplementary material

References (RIS)

MS 395-102

Published 21 January 2025

Funded by NSF OCE1326927, ECORD, and JAMSTEC

R.E. Parnell-Turner, A. Briais, L.J. LeVay, Y. Cui, A. Di Chiara, J.P. Dodd, T. Dunkley Jones, D. Dwyer, D.E. Eason, S.A. Friedman, S.R. Hemming, K. Hochmuth, H. Ibrahim, C. Jasper, B.T. Karatsolis, S. Lee, D.E. LeBlanc, M.R. Lindsay, D.D. McNamara, S.E. Modestou, B. Murton, S. OConnell, G.T. Pasquet, P.N. Pearson, S.P. Qian, Y. Rosenthal, S. Satolli, M. Sinnesael, T. Suzuki, T. Thulasi Doss, N.J. White, T. Wu, and A. Yang Yang²

¹ Parnell-Turner, R.E., Briais, A., LeVay, L.J., Cui, Y., Di Chiara, A., Dodd, J.P., Dunkley Jones, T., Dwyer, D., Eason, D.E., Friedman, S.A., Hemming, S.R., Hochmuth, K., Ibrahim, H., Jasper, C., Karatsolis, B.T., Lee, S., LeBlanc, D.E., Lindsay, M.R., McNamara, D.D., Modestou, S.E., Murton, B., OConnell, S., Pasquet, G.T., Pearson, P.N., Qian, S.P., Rosenthal, Y., Satolli, S., Sinnesael, M., Suzuki, T., Thulasi Doss, T., White, N.J., Wu, T., and Yang Yang, A., 2025. Expedition 395 methods. In Parnell-Turner, R.E., Briais, A., LeVay, L.J., and the Expedition 395 Scientists, *Reykjanes Mantle Convection and Climate. Proceedings of the International Ocean Discovery Program, 395: College Station, TX (International Ocean Discovery Program)*. <https://doi.org/10.14379/iodp.proc.395.102.2025>

² **Expedition 395 Scientists' affiliations.**

1. Introduction

This chapter provides an overview of the procedures and methods employed for coring operations and in the shipboard laboratories of the research vessel (R/V) *JOIDES Resolution* during International Ocean Discovery Program (IODP) Expeditions 384, 395C, and 395. Hereafter, the expeditions will be known jointly as Expedition 395 unless otherwise specified. The laboratory information applies only to shipboard work described in the Expedition Report section of the Expedition 395 *Proceedings of the International Ocean Discovery Program* volume that used the shipboard sample registry, imaging and analytical instruments, core description tools, and the Laboratory Information Management System (LIMS) database. Methods used by investigators for postcruise shore-based analyses of Expedition 395 project data will be documented in separate publications.

Shipboard and shore-based scientists contributed to this volume with the following primary responsibilities (authors are listed in alphabetical order; see **Expedition 395 scientists** for contact information):

- Summary chapter: Expedition 395 Scientists
- Methods and site chapters:
 - Background and objectives: A. Briais, R. Parnell-Turner
 - Operations: K. Grigar, L. LeVay
 - Lithostratigraphy: H. Ibrahim, C. Jasper, D. LeBlanc, S. Lee, S. Modestou, S. OConnell, T. Thulasi Doss
 - Igneous petrology: D. Eason, B. Murton, N. White, T. Wu
 - Alteration petrology and structural geology: D. McNamara, G. Pasquet
 - Micropaleontology: T. Dunkley Jones, B. Karatsolis, P. Pearson, T. Suzuki
 - Physical properties: D. Dwyer, S. Hemming, K. Hochmuth, D. McNamara, M. Sinnesael, N. White
 - Stratigraphic correlation: S. Hemming, M. Sinnesael
 - Paleomagnetism: A. Di Chiara, D. Dwyer, S. Friedman, S. Satolli
 - Geochemistry and microbiology: Y. Cui, J. Dodd, M. Lindsay, G. Pasquet
 - Downhole measurements: K. Hochmuth, D. McNamara
 - Age model: A. Di Chiara, T. Dunkley Jones, S. Friedman, B. Karatsolis, P. Pearson, S. Satolli, T. Suzuki

This introductory section provides an overview of drilling and coring operations, core handling, curatorial conventions, depth scale terminology, and the sequence of shipboard analyses. Subsequent sections of this chapter document specific laboratory instruments and methods in detail.

1.1. Operations

The IODP Environmental Protection and Safety Panel (EPSP) approved the six primary and seven alternate drilling sites for Expedition 395 described in the Scientific Prospectus (Parnell-Turner et al., 2020) and Scientific Prospectus Addendum (Parnell-Turner et al., 2023). The shipboard global navigation satellite system (GNSS) (WGS84 datum) was used to position the vessel at the Expedition 395 sites. Once the vessel was positioned at a site, the thrusters were lowered, and a seafloor positioning beacon was prepared for deployment in case it was needed. Dynamic positioning control of the vessel was constrained by the navigational input from the GNSS system (Figure F1). No seafloor positioning beacons were deployed during this expedition. The final hole position was calculated as the mean position of at least 1000 GNSS position fixes while the hole was occupied. The ship's position is resolved with an accuracy of less than 1 m, but the exact position of the hole is less well known because of the deviation of the pipe below the ship, which can vary depending on water currents, tides, and water depth; the hole position is thus known typically within 10 m accuracy. The precision depth recorder (PDR) was used to estimate the depth of the seafloor.

Drilling sites were numbered according to the series that began with the first site drilled by the drilling vessel (D/V) *Glomar Challenger* in 1968. Starting with Integrated Ocean Drilling Program Expedition 301, the prefix "U" designates sites occupied by *JOIDES Resolution*. When drilling multiple holes at a site, hole locations were offset from each other by ~10–20 m. A letter suffix distinguishes each hole drilled at the same site. The first hole drilled is assigned the site number modified by the suffix "A," the second hole takes the site number and the suffix "B," and so forth. During Expedition 395, six sites were occupied (U1554, U1555, U1562, U1563, U1564, and U1602) and 27 holes were drilled (see Table T1 in the Expedition 395 summary chapter [Parnell-Turner et al., 2025]).

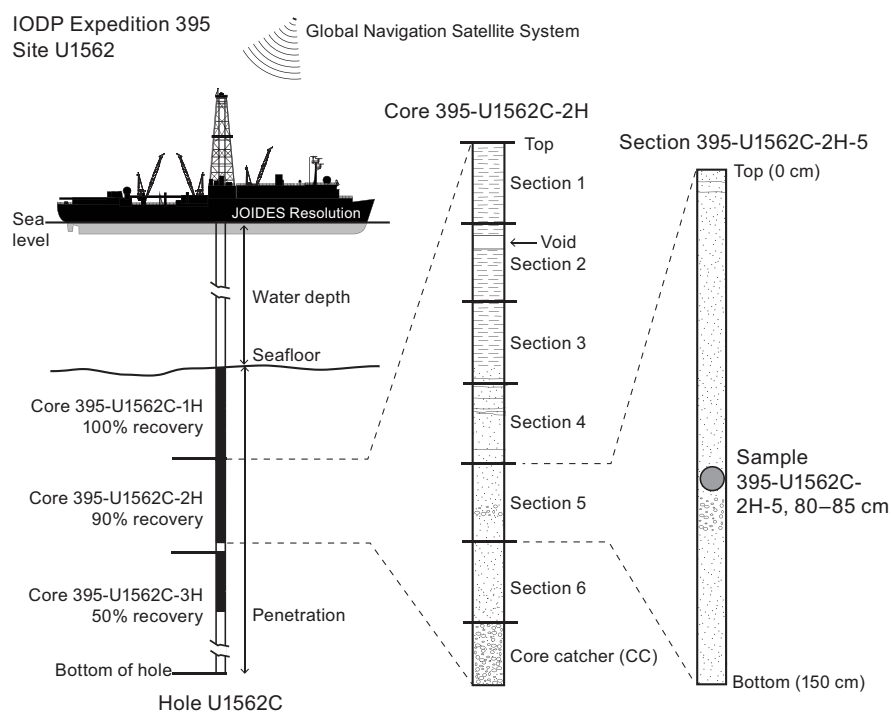


Figure F1. IODP convention for naming sites, holes, cores, sections, and samples. Ship positioning while coring was accomplished with the global navigation satellite system. Cores from Hole 395-U1562C are used as an example; actual recovery percentages differ.

1.2. JOIDES Resolution standard coring systems

The advanced piston corer (APC), half-length APC (HLAPC), extended core barrel (XCB), and rotary core barrel (RCB) systems were used during Expedition 395. These tools and other drilling technology are documented in Graber et al. (2002).

The APC and HLAPC systems cut soft-sediment cores with minimal coring disturbance relative to other IODP coring systems. After the APC/HLAPC core barrel is lowered through the drill pipe and lands above the bit, the inside of the drill pipe is pressured up until one or two shear pins that hold the inner barrel attached to the outer barrel fail. The inner barrel then advances into the formation at high speed and cuts a core with a diameter of 6.6 cm (2.6 inches) (Figure F2). The driller can detect a successful cut, or full stroke, from the pressure gauge on the rig floor because the excess pressure accumulated prior to the stroke drops rapidly. The depth limit of the APC system, often referred to as APC refusal, is indicated in two ways: (1) the piston fails to achieve a complete stroke (as determined from the pump pressure and recovery reading) because the formation is too hard or (2) excessive force (>60,000 lb) is required to pull the core barrel out of the formation. When a full stroke could not be achieved, one or more additional attempts were typically made, and each time the bit was advanced by the length of the core recovered (note that for these cores, this results in a nominal recovery of ~100%). When a full or partial stroke is achieved but excessive force is insufficient to retrieve the core barrel, it can be drilled over, meaning that after the inner core barrel was successfully shot into the formation the drill bit is advanced to total depth to free the APC barrel.

The standard APC system uses a 9.6 m long core barrel, whereas the HLAPC system uses a 4.7 m long core barrel. The HLAPC typically is deployed after the standard APC has repeated partial strokes. Occasionally, the HLAPC is interchanged with the APC to offset coring gaps for strati-

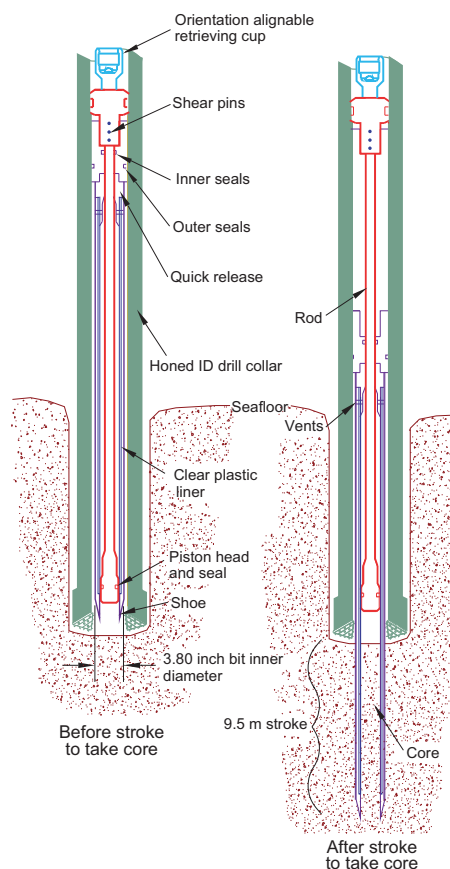


Figure F2. APC system used during Expedition 395 (see Graber et al., 2002). The HLAPC uses the same equipment, but the core barrel is 4.7 m in length. ID = inner diameter.

graphic correlation. While using the HLAPC, the same criteria is applied in terms of refusal as for the APC system.

The XCB system is typically used when the APC/HLAPC system has difficulty penetrating the formation and/or damages the core liner or core. The XCB system can also be either used to initiate holes where the seafloor is not suitable for APC coring or interchanged with the APC/HLAPC when dictated by changing formation conditions. For example, the XCB system was deployed during Expedition 395 to better recover the sediment/basement interface. The XCB system has a small cutting shoe that extends below the large APC/XCB bit (Figure F3). The smaller bit can cut a semi-indurated core with less torque and fluid circulation than the main bit, optimizing recovery. The XCB cutting shoe extends ~30.5 cm ahead of the main bit in soft sediment but retracts into the main bit when hard formations are encountered. It cuts cores with a nominal diameter of 5.87 cm (2.31 inches), slightly less than the 6.6 cm diameter of APC cores. XCB cores are often broken (i.e., torqued) into biscuits, which are disc-shaped pieces a few to several centimeters long with remolded sediment (including some drilling slurry) interlayering the discs and packing the space between the discs and the core liner. This type of drilling disturbance may give the impression that the XCB cores have the same diameter (6.6 cm) as the APC cores.

The bottom-hole assembly (BHA) used for APC and XCB coring during Expeditions 384 and 395C was composed of an 11 $\frac{1}{16}$ inch (~29.05 cm) bit, a bit sub, a seal bore drill collar, a landing saver sub, a modified top sub, a modified head sub, a variable number of 8 $\frac{1}{4}$ inch control length drill collars, a tapered drill collar, two stands of 5 $\frac{1}{2}$ inch transition drill pipe, and a crossover sub to the drill pipe that extended to the surface. The same BHA was used during Expedition 395 except for the drill bit, which was a 9 $\frac{7}{8}$ inch polycrystalline diamond compact bit.

The RCB system is designed to recover firm to hard sediments and basement rocks. The BHA, including the bit and outer core barrel, is rotated with the drill string while bearings allow the inner core barrel to remain stationary (Figure F4).

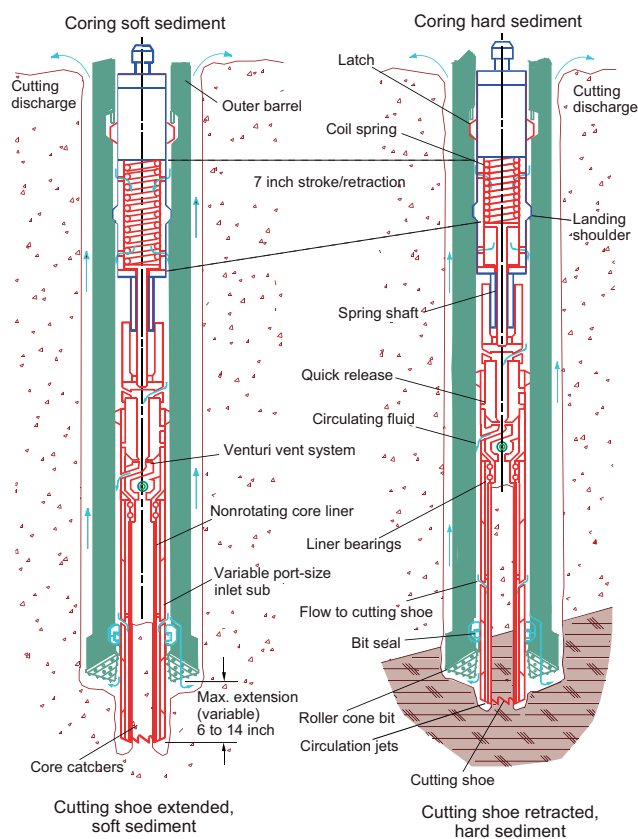


Figure F3. XCB system used during Expedition 395 (see Graber et al., 2002).

A typical RCB BHA includes a 9 $\frac{7}{8}$ inch drill bit, a mechanical bit release, a bit sub, an outer core barrel, a modified top sub, a modified head sub, a variable number of 8 $\frac{1}{4}$ inch control length drill collars, a tapered drill collar, two stands of 5 $\frac{1}{2}$ inch drill pipe, and a crossover sub to the drill pipe that extends to the surface.

Nonmagnetic core barrels were used for all APC, HLAPC, and RCB coring. APC cores were oriented with the Icefield MI-5 core orientation tool when coring conditions allowed (see Operations in each site chapter for more information). During Expedition 384, the FlexIT core orientation tool was also used (Blum et al., 2020). Formation temperature measurements were taken with the third-generation advanced piston corer temperature (APCT-3) tool (see [Downhole measurements](#)). Information on recovered cores, drilled intervals, downhole tool deployments, and related information are provided in Operations, Paleomagnetism, and Downhole measurements in each site chapter.

1.3. Drilling disturbance

Cores may be significantly disturbed by the drilling process and contain extraneous material because of the coring and core handling process. In formations with loose granular layers (e.g., sand, ash, foraminifer ooze, and clasts), granular material from intervals higher in the hole may settle and accumulate in the bottom of the hole because of drilling circulation and be sampled with the next core. The uppermost 10–50 cm of each core must therefore be examined critically for potential fall-in. Several cores recovered during Expedition 395 have large clasts at the top of the first section, which likely fell in from above.

Common coring-induced deformation includes the concave-downward appearance of originally horizontal bedding. Piston action may result in fluidization (flow-in) at the bottom of, or sometimes within, APC cores. Retrieval of unconsolidated cores from depth to the surface typically results to some degree in elastic rebound, and gas that is in solution at depth may become free and drive core segments in the liner apart. When gas content is high, pressure must be relieved for

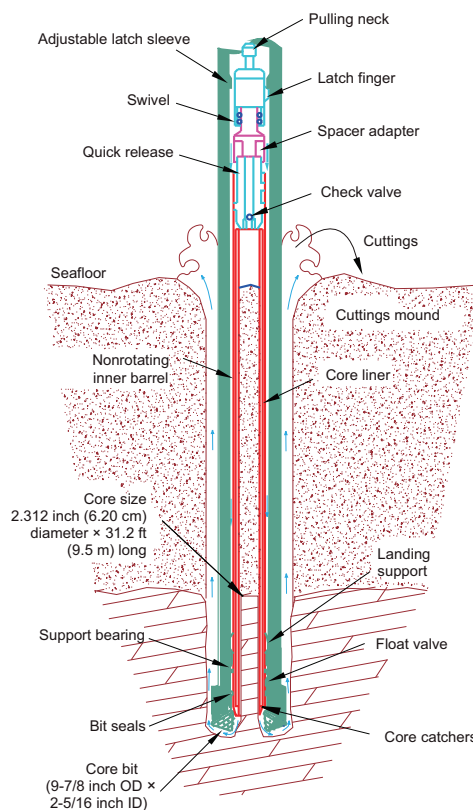


Figure F4. RCB system used during Expedition 395 (see Graber et al., 2002). OD = outer diameter, ID = inner diameter.

safety reasons before the cores are cut into segments. Holes are drilled into the liner, which forces some sediment and gas out of the liner. As noted above, XCB coring typically results in biscuits mixed with drilling slurry. Drilling disturbances are described in Lithostratigraphy in each site chapter and are indicated on the graphic core summary reports, also referred to as visual core descriptions (VCDs).

1.4. Downhole measurements

1.4.1. Formation temperature

Formation temperature measurements were taken with the APCT-3 tool (see [Downhole measurements](#)) embedded in the APC cutting shoe at specified intervals. These measurements were used to obtain temperature gradients and heat flow estimates. Information on downhole tool deployments is provided in Operations and Downhole measurements in each site chapter.

1.4.2. Wireline logging

During wireline logging operations, the logs were recorded with Schlumberger and IODP logging tools combined into tool strings, which were lowered into the hole after the completion of coring operations. Four tool strings were run across the three expeditions: the triple combination (triple combo), Formation MicroScanner (FMS)-sonic, Ultrasonic Borehole Imager (UBI), and Versatile Seismic Imager (VSI). A full description of the logging tools used can be found in Downhole measurements in each site chapter.

In preparation for logging, the boreholes were flushed of debris by circulating drilling fluid and were at least partially filled with seawater-based logging gel (sepiolite mud mixed with seawater). Only one hole, U1555I, was displaced with heavy mud (weighted with barite; density = ~ 1258 kg/m³) to help stabilize the borehole walls in sections where instability was expected from drilling and coring disturbance. The BHA was pulled up to a suitable depth below seafloor, where it protected the unstable upper part of the hole. For holes in which the RCB system was used, the bit was either dropped on the seafloor or at the bottom of the hole prior to setting the BHA at depth. The tool string was then lowered downhole on a seven-conductor wireline cable before being pulled up at a constant speed of 550 m/h (or 250 m/h for the UBI) to provide continuous log measurements of several properties simultaneously. Further details on the logging operations are described in Downhole measurements in each site chapter.

1.5. Core and section handling

1.5.1. Whole-round cores

When the core barrel reached the rig floor, the core catcher from the bottom of the core was removed and taken to the core receiving platform (catwalk). When coring sediment, a sample was extracted for paleontological (PAL) analysis from the core catcher (Figure F5). Next, the sediment core was extracted from the core barrel in its plastic liner. The liner was carried from the rig floor to the core processing area on the catwalk outside the core laboratory, where it was split into ~ 1.5 m sections. The exact section length was noted and entered into the database as created length using the Sample Master application. This number was used to calculate core recovery.

Once the core was cut into sections, whole-round sediment samples were immediately taken for interstitial water (IW) extraction and chemical analyses from the bottom of selected core sections. Headspace samples were taken from the top of a selected section (typically one per core) using a syringe for immediate gas analyses according to the IODP hydrocarbon safety monitoring protocol. Samples for microbiological analysis of sediment and basalt were also collected at this stage. The resulting sediment residues (squeeze cakes) from the IW analyses were used for bulk geochemistry measurements.

When catwalk sampling was complete for sediment cores, liner caps (blue = top, colorless = bottom, and yellow = top of section where a whole-round sample was removed) were glued with acetone onto liner sections, and the sections were labeled and laser engraved with their section identification numbers. The whole rounds were then placed in core racks for analysis. Oxygen probe measurements were taken from selected core sections (see [Geochemistry and microbiol-](#)

ogy). For the basalt intervals, the cores were brought directly from the catwalk to the core splitting room without adhering endcaps. The basalt cores were shaken out of the core liner into alcohol-cleaned split liner sections. Whole-round samples (~5 cm length) were selected for microbiological studies and photographed. The basalt pieces were marked for orientation, rinsed with freshwater, and placed in split liners. Core cut lines, or split lines, were drawn on the hard rock pieces and then aligned as working and archive halves.

The curated length of the sediment cores was set equal to the created length and was updated very rarely (e.g., in cases of data entry errors or when section length expanded by more than ~2 cm). The curated length of the hard rock is measured after the rock pieces are placed in individual bins in the core liner. Depth in hole calculations are based on the curated section length (see [Depth calculations](#)).

The workflow for the whole-round sediment and hard rock cores differs. Most sediment cores were immediately run through the Special Task Multisensor Logger (STMSL) to collect 5 cm resolution magnetic susceptibility (MS) and gamma ray attenuation (GRA) bulk density data for stratigraphic correlation. The whole-round sections were run through the Natural Gamma Radiation Logger (NGRL) and X-ray imaged using the X-Ray Linescan Logger (XSCAN) prior to thermal equilibration. When the core sections reached equilibrium with laboratory temperature (typically after 4 h), they were run through the Whole-Round Multisensor Logger (WRMSL) for MS, GRA bulk density, and P -wave velocity (V_p). Thermal conductivity measurements were taken once per core when the material was suitable. See [Physical properties](#) for more information.

Following the binning of hard rock sections, the cores were imaged using the Section Half Imaging Logger (SHIL) in 360° mode. The split core liners were then held together with electrical tape while the whole rounds were run through the NGRL and, following thermal equilibration, the WRMSL for MS and GRA bulk density.

1.5.2. Core section halves

After completion of whole-round analyses, the sections were split lengthwise into working and archive halves (Figure F5). Soft-sediment cores were split with a wire; investigators should note that older material can be transported upward on the split face of a section during splitting using this method. Harder sediment and hard rock were cut using a saw. Following cutting, the pieces of hard rock were dried and individual labels were adhered to each piece.

Discrete samples were then taken from the working half of each core for moisture and density (MAD), paleomagnetic (PMAG), carbonate (CARB), smear slide, and thin section analysis for the

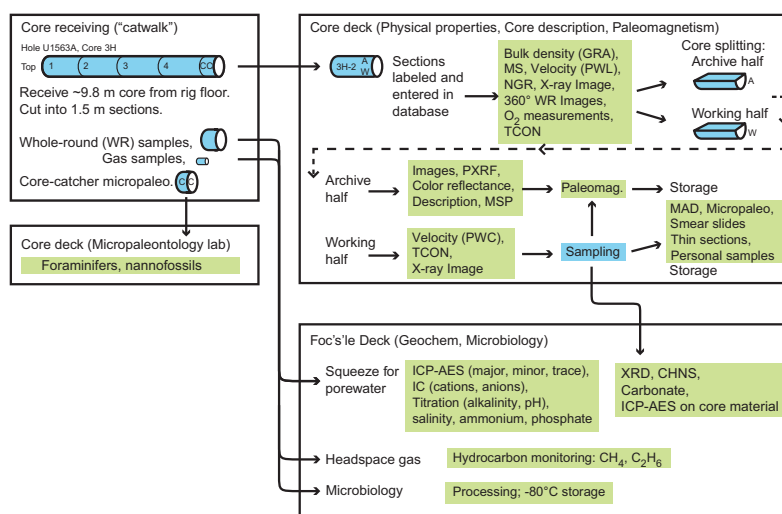


Figure F5. Overall flow of cores, sections, analyses, and sampling implemented during Expedition 395. All the measurements listed were implemented at some stage during the three expeditions. Refer to individual site chapters for more information. TCON = thermal conductivity, IC = ion chromatography.

sedimentary section. Samples for PMAG, thin sections, and inductively coupled plasma–atomic emission spectroscopy (ICP-AES) analyses were selected from the hard rock. PMAG samples from the hard rock were used for MAD analysis. Selected working half core sections were X-ray imaged and measured for thermal conductivity. V_p was measured using the caliper and/or bayonets on the physical properties gantry.

During the expeditions, samples for personal postcruise research were taken only where they concerned ephemeral properties (e.g., IW and microbiology). Personal sampling of the sedimentary sections was deferred to a postcruise sampling party. During Expedition 395, personal sampling for hard rock was permitted to avoid having to cut samples at the postcruise sampling party.

The archive half of each core was scanned on the SHIL to provide linescan images and then measured for point MS (MSP) and reflectance spectroscopy and colorimetry on the Section Half Multisensor Logger (SHMSL). Hard rock cores were imaged with both wet and dry surfaces. Labeled foam pieces were used to denote missing whole-round intervals in the SHIL images. The archive halves were then described visually and by means of smear slide for sedimentology and thin section for petrology. Hard rock cores were point scanned using the portable X-ray fluorescence spectrometer (pXRF). Finally, the magnetization of archive half sections and working half discrete pieces was measured with the superconducting rock magnetometer (SRM) and spinner magnetometer.

When all steps were completed, cores were wrapped, sealed in plastic D-tubes, boxed, and transferred to cold storage space aboard the ship. At the end of Expedition 395, all the working half core sections were shipped to the IODP Bremen Core Repository (BCR) (Germany). The archive halves were sent to the IODP Gulf Coast Repository (GCR) in College Station (USA) for X-ray fluorescence (XRF) scanning, with the exception of archive halves collected at Site U1602, which were shipped to Scripps Institution of Oceanography (USA) for XRF scanning. All core sections from Expeditions 384 and 395C were shipped to the GCR for visual description and XRF scanning and partial U-channel sampling.

1.6. Sample identifiers

Sample naming in this volume follows standard IODP procedure. A full sample identifier consists of the following information: expedition, site, hole, core number, core type, section number, section half, and offset in centimeters measured from the top of the core section (Figure F1). For example, a sample identification of “395C-U1554E-5H-3W, 10–12 cm,” represents a sample taken from the interval between 10 and 12 cm below the top of the working half (“W”) of Section 3 of Core 5 (“H” designates that this core was taken with the APC system) of Hole U1554E during Expedition 395C. The archive half is designated by an “A” following the section number.

The drilling system used to obtain a core is designated in the sample identifiers as follows: H = APC, F = HLAPC, X = XCB, and R = RCB. Integers are used to denote the core type of drilled intervals (e.g., a drilled interval between Cores 2H and 4H would be denoted by Core 31, where 1 is the core type).

When working with data downloaded from the LIMS database or physical samples that were labeled on the ship, three additional sample naming concepts may be encountered: text ID, label ID, and printed labels.

1.6.1. Text ID

Samples taken on *JOIDES Resolution* are uniquely identified for use by software applications using a text ID, which combines two elements:

- Sample type designation (e.g., TSB for thin section billet) and
- A unique sequential number for any sample and sample type added to the sample type code (e.g., TSB22072522).

The text ID is not particularly helpful to most users but is critical for machine reading and troubleshooting.

1.6.2. Label ID

The label ID is used throughout the *JOIDES Resolution* workflows as a convenient, human-readable sample identity. However, a label ID is not necessarily unique. The label ID is made up of two parts: primary sample identifier and sample name.

The primary sample identifier is very similar to the full sample identifier described above, with two notable exceptions:

- Section halves always carry the appropriate identifier (395-U1602B-22F-1-A and 395-U1602B-22F-1-W for archive and working halves, respectively).
- Sample top and bottom offsets, relative to the parent section, are indicated as “35/37” rather than “35–37 cm.”

1.7. Depth calculations

Sample and measurement depth calculations were based on the methods described in IODP Depth Scales Terminology v.2 (<https://www.iodp.org/policies-and-guidelines/142-iodp-depth-scales-terminology-april-2011/file>). The definition of multiple depth scale types and their distinction in nomenclature should keep the user aware that a nominal depth value at two different depth scale types (and even two different depth scales of the same type) generally does not refer to the exact same stratigraphic interval in a hole. The SI unit for all depth scales is meters.

Depths of cored intervals were measured from the drill floor based on the length of drill pipe deployed beneath the rig floor and referred to as drilling depth below rig floor (DRF); it is traditionally referred to with custom units of meters below rig floor (mbrf). The depth of each cored interval, measured on the DRF scale, can be referenced to the seafloor by subtracting the seafloor depth measurement (on the DRF scale) from the cored interval (on the DRF scale). This seafloor referenced depth of the cored interval is reported on the drilling depth below seafloor (DSF) scale. In the case of APC coring, the seafloor depth was calculated as the length of pipe deployed minus the length of the mudline core recovered.

Depths of samples and measurements in each core were computed based on a set of rules that result in the core depth below seafloor, Method A (CSF-A), depth scale. The two fundamental rules for this scale are that (1) the top depth of a recovered core corresponds to the top depth of its cored interval (top DSF depth = top CSF-A depth) regardless of type of material recovered or drilling disturbance observed and (2) the recovered material is a contiguous stratigraphic representation even when core segments are separated by voids when recovered, the core is shorter than the cored interval, or it is unknown how much material is missing between core pieces. When voids were present in the core on the catwalk, they were closed by pushing core segments together whenever possible. The length of missing core should be considered a depth uncertainty when analyzing data associated with core material.

When core sections were given their curated lengths, they were also given a top and a bottom depth based on the core top depth and the section length. Depths of samples and measurements on the CSF-A scale were calculated by adding the offset of the sample (or measurement from the top of its section) to the top depth of the section.

Per IODP policy established after the introduction of the IODP Depth Scales Terminology v.2, sample and measurement depths on the CSF-A depth scale may be referred to with the custom unit meters below seafloor (mbsf). In this volume, mbsf is not used. The reader should be aware that different depth scales may be assigned to the same stratigraphic interval. For example, a soft-sediment core from less than a few hundred meters below seafloor often expands upon recovery (typically by a few percent to as much as 15%), and the length of the recovered core exceeds that of the cored interval. Therefore, a stratigraphic interval in a particular hole may not have the same depth on the DSF and CSF-A scales. When recovery in a core exceeds 100%, the CSF-A depth of a sample taken from the bottom of the core will be deeper than that of a sample from the top of the subsequent core (i.e., some data associated with the two cores overlap on the CSF-A scale). To overcome the overlap problem, core intervals can be placed on the core depth below seafloor,

Method B (CSF-B), depth scale. The CSF-B approach scales the recovered core length back into the interval cored, from >100% to exactly 100% recovery. If cores had <100% recovery to begin with, they are not scaled. When downloading data using the *JOIDES Resolution* Science Operator (JRSO) LIMS Reports (<http://web.iodp.tamu.edu/LORE>), depths for samples and measurements are by default presented on both the CSF-A and CSF-B scales. The CSF-B depth scale can be useful for data analysis and presentations at sites with a single hole.

Wireline logging data are collected at the wireline log depth below rig floor (WRF) scale, from which a seafloor measurement is subtracted to create the wireline log depth below seafloor (WSF) scale. Immediately after data collection was completed, the wireline logging data were transferred to the Lamont-Doherty Earth Observatory Borehole Research Group (LDEO-BRG), where multiple passes and runs were depth matched using the gamma radiation logs. The data were returned to the ship at the wireline log matched depth below seafloor (WMSF) scale, which is the final and official logging depth scale type for investigators.

During Expedition 395, all core depths below seafloor were initially calculated according to the CSF-A depth scale. Unless otherwise noted, all depths presented are core depths below seafloor calculated as CSF-A and reported as “m CSF-A.”

Core composite depth below seafloor (CCSF) depth scales are constructed for sites with two or more holes to create as continuous a stratigraphic record as possible through correlation between the various holes. This also helps to mitigate the CSF-A core overlap problem and the coring gap problem. Using shipboard core logger-based physical property data verified with core photos, core depths in adjacent holes at a site are vertically shifted to correlate between cores recovered in adjacent holes. This process produces the CCSF depth scale. The correlation process was achieved with the Correlator program Version 4.0 and resulted in affine tables, indicating the vertical shift of cores on the CCSF scale relative to the CSF-A scale. Once the CCSF scale is constructed, a splice can be defined that best represents the stratigraphy of a site by utilizing and splicing the most representative portions of individual sections and cores from each hole. Because of core expansion, the CCSF depths of stratigraphic intervals are typically 10%–15% deeper than their CSF-A depths. CCSF depth scale construction also reveals that coring gaps on the order of 1.0–1.5 m typically occur between two subsequent cores, despite the apparent >100% recovery. For more details on construction of the CCSF depth scale, see [Stratigraphic correlation](#).

2. Lithology

This section outlines the procedures for documenting the sedimentology of cores recovered during Expeditions 384, 395C, and 395, including core description, smear slide description, and color spectrophotometry. All observations and data were uploaded directly to the IODP LIMS database using the GEODESC application. The LIMS Information Viewer (LIVE) is a graphic display for core data (e.g., digital images of section halves, principal lithology, and drilling disturbance) that was used for quality control of the uploaded data sets.

2.1. Core preparation and digital color imaging

Prior to core description and high-resolution digital color imaging, the quality of the split core surface of the archive half of each core was assessed and the surface was scraped lightly with a metallic or glass plate as needed. Cleaned core sections were then described in conjunction with images obtained by the SHIL, results of smear slide observations, and measurements obtained from the SHMSL (see [Physical properties](#)).

Cleaned archive halves were imaged with the SHIL as soon as possible to avoid sediment color changes caused by oxidation and drying. In cases of watery or soupy sediment, the surface was dried, either with the assistance of fans or by blotting with a paper towel, to avoid light reflection during scanning. Two images, a high-resolution JPEG image with grayscale and depth ruler and a low-resolution cropped JPEG image showing only the core section surface, were created from the high-resolution TIFF files. These images were uploaded to the LIMS database under Images >

Core sections, and the red-green-blue (RGB) colorimetry data was uploaded to the LIMS database under Physical properties > RGB channels.

2.2. Smear slide summary

Smear slide examination was used to determine the biogenic and terrigenous constituents and their relative abundances to aid in lithologic classification. Toothpick samples were taken from each lithology at a frequency of at least two per core. Slides were prepared by mixing the sediment with a drop of deionized water on a glass slide and drying on a hot plate at 80°C. A sufficient amount of Norland optical adhesive Number 61 was dropped onto the dried slide, and a cover slip was placed over the sediment. The coverslip was fixed to the slide in an ultraviolet light box. Smear slides were examined with a transmitted-light petrographic microscope equipped with a standard eyepiece micrometer. Biogenic and mineral components were identified following standard petrographic techniques as described in Rothwell (1989), Marsaglia et al. (2013), and Marsaglia et al. (2015). Several fields of view (FOVs) were examined with a 10× eyepiece and some combination of 5×, 10×, 20×, and 40× objectives in a transversal section to assess the abundance of detrital, biogenic, and authigenic components. The relative abundance percentages of the sedimentary constituents were visually estimated using the techniques of Rothwell (1989). Type and relative abundance of biogenic and terrigenous components were estimated for each smear slide. Data were entered in the LIMS database using a custom template in GEODESC. Biogenic components observed in smear slides were categorized as follows:

- T = trace (<1%).
- R = rare (1% to <5%).
- C = common (5% to <20%).
- A = abundant (20% to <50%).
- D = dominant (≥50%).

2.3. Lithologic description and classification of sediments and sedimentary rocks

The principal lithologic name was assigned on the basis of the relative abundances of biogenic and terrigenous clastic grains. The name assigned to a sediment/rock with <50% biogenic grains was based on the grain size characteristics of the terrigenous clastic fraction (Figure F6). Sediment/rocks with >50% biogenic material were named based on the type and abundance of biogenic material and degree of lithification/diagenesis. Sediments were also characterized by degree of lithification as follows: (1) soft biogenic sediments that deformed under finger pressure were classified as oozes, (2) diagenetic/lithified carbonate sediments (which no longer deform under finger pressure) were described as chalk, and (3) solid/lithified carbonate sediments were described as limestone. The suffix “-stone” was also added to predominantly terrigenous beds which had become lithified. Sediments were classified using the Wentworth (1922) scale to define grain size classes as follows:

- The principal name of a sediment with <50% biogenic grains was based on the predominant grain size of both the terrigenous and biogenic grains. Grain size was largely determined by analysis of smear slides.

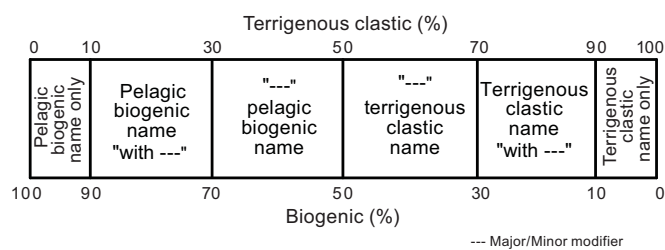


Figure F6. Lithologic classification based on percentage terrigenous and percentage biogenic in the sediment core, Expedition 395.

- The principal name of a sediment with $\geq 50\%$ biogenic grains was classified as an ooze, modified by the most abundant specific biogenic grain type that formed 50% or more of the sediment. For example, if nannofossils exceeded 50%, then the sediment was classified as a nannofossil ooze. Biogenic constituents of similar composition were grouped together to exceed this 50% abundance threshold. For example, if nannofossils were 40% of the sediment and foraminifers were 20%, then the sediment was termed carbonate ooze or, in the case where the two components were clearly distinguishable and of relatively equal proportions, foraminifer-nannofossil ooze.

Major and minor modifiers were applied to any of the principal granular sediment names as follows:

- Minor modifiers were those components with abundances between 10% and $<30\%$ and were used in the lithology suffix preceded by “with.” When more than one minor modifier was present, the component with the higher abundance was followed by the component with less abundance and so forth. When several biogenic components were present and in total exceeded 10%, the term “biogenics” was used. For example, a sediment with 35% silt, 45% clay, 6% nannofossils, 6% foraminifers, 6% diatoms, and 2% sponge spicules was classified as “silty clay with biogenics.”
- Major modifiers were those components with abundances between 30% and 50% and were used in the lithology prefix. For example, a sediment with 35% nannofossils, 30% silt, and 35% clay would be classified as a nannofossil silty clay.

Component abundances and the resulting principal lithologic name were noted in the microscopic and macroscopic sediment templates in GEODESC DataCapture (Figure F7). For cores collected during Expeditions 384 and 395C and described at the GCR, sediments within the range of silty clay to clayey silt were described using the combined term “silty clay or clayey silt” for the following holes:

- Holes U1554A–U1554F,
- Holes U1555H and U1555I,
- Holes U1562A and U1562B,
- Hole U1563A, and
- Holes U1564A–U1564C.

Where a given site was revisited during Expedition 395 and the same sedimentary sequences were recovered, intervals of sediment originally classified as “silty clay or clayey silt” were reexamined.

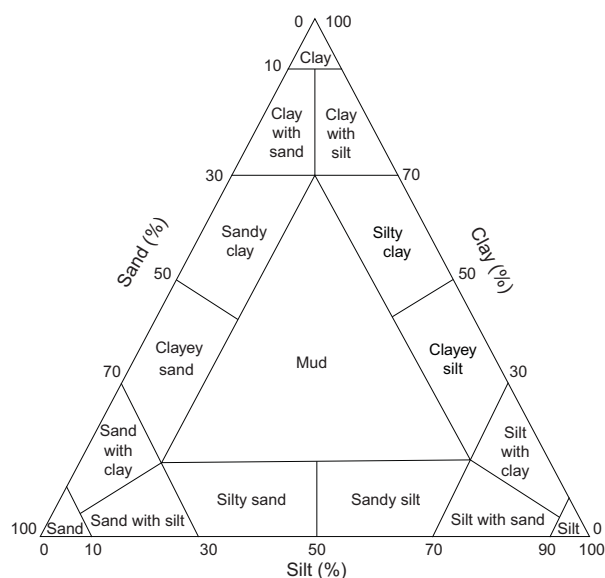


Figure F7. Ternary diagram used to determine the name of the lithology of terrigenous sediment, Expedition 395.

This additional analysis allowed for refinement of the “silty clay or clayey silt” lithology to either “silty clay” or “clayey silt” at most sites. In most instances, refinement to “silty clay” was prevalent. This refinement has been applied where possible to the lithologic summaries documented in this volume.

2.4. Sedimentary structures

The presence of sedimentary structures was noted in the macroscopic sediment template in GEODESC Data Capture as follows:

- Fault: a discrete surface or zone of discrete surfaces separating two sedimentary units across which one mass has slid past the other. An offset is clearly observed based on textures and/or colors.
- Fracture: any separation in the sediment core, inclusive of faults and joints, when there was no clear offset on either side of the feature.
- Soft-sediment deformation: sediment which appears waved or otherwise deformed by post-depositional physical movement.
- Graded bed: a layer that displays a gradual and progressive change, either in color or in particle size. If the bed was only graded by color, it was noted in the sedimentary structure comments.
- Contacts: contacts between lithologies were described and assigned to the base of the interval in which they appeared. Contacts include, but are not limited to, color transitions and other boundaries disturbed by bioturbation, as well as obvious lithologic boundaries.

2.5. Clast abundance

Clasts that were visible on the surface of the cores were documented. Clasts between 0.5 and 2 cm were counted, and their depth within the section was recorded. If a clast was more than 2 cm long on its major axis, it was removed from the section half, cleaned, examined and put back before the section was imaged on the SHIL. If removal of the clast would cause obvious disturbance to the core material, the clast was removed after imaging. The size, composition, and depth in core were also recorded for clasts >2 cm.

2.6. Spectrophotometry and colorimetry

The SHMSL employs multiple sensors for the measurement of bulk physical properties in a motorized and computer-controlled section-half logging machine. The sensors included in the SHMSL are reflectance spectroscopy and colorimetry, MS, and a laser surface analyzer. Spectrophotometry and MS were measured at 2 or 2.5 cm resolution. Reflectance spectroscopy (spectrophotometry) was carried out using an Ocean Insight QE-Pro spectrophotometer. This instrument measures the reflectance spectra of the split core from the ultraviolet to near-infrared range. Colorimetric information is extracted from the reflectance data to the $L^*a^*b^*$ color space system. The $L^*a^*b^*$ color space expresses color as a function of lightness (L^*) and color values, where a^* reflects the balance between red (positive a^*) and green (negative a^*) and b^* reflects the balance between yellow (positive b^*) and blue (negative b^*). When a^* and b^* are 0, there is no color and L^* determines grayscale. MS was measured on the SHMSL with a Bartington MS2 meter and MS2K contact probe. Additional instrument details and instrument resolution for each hole are given in [Physical properties](#).

Accurate spectrophotometry using the SHMSL demands a direct and level contact between the instrument sensors and the split core surface. A built-in laser surface analyzer aids the recognition of irregularities in the split core surface (e.g., cracks and voids), and data from this tool were recorded to provide an independent check on the fidelity of SHMSL measurements.

2.7. Visual core description and standard graphic report

Information from macroscopic standard sedimentologic observations for each core was recorded directly into GEODESC DataCapture. Two templates were constructed (drilling disturbance and macroscopic sediment), and data entry columns were customized to include relevant descriptive information categories. For the macroscopic sediment template, these categories include lithology,

sedimentary structures, bioturbation intensity, Munsell color, macrofossils, and clast counts. A summary description was created for each core.

A simplified one-page graphical representation of each core, referred to as a VCD (Figure F8), was generated using the LIMS2Excel application and the commercial program Strater (Golden Software). VCDs are presented with the CSF-A depth scale; age; shipboard samples; split core photographs; graphic lithology; and columns for core disturbance, bioturbation, sedimentary structures, color reflectance ($L^*a^*b^*$), clast count (including only clasts with a long axis greater than 2 cm), MS, GRA bulk density, and natural gamma radiation (NGR) counts. The graphic lithologies, sedimentary structures, and other visual observations are represented on the VCDs by graphic patterns and symbols (Figure F9). Each VCD also contains the summary description for the core. Only major lithologies are shown on the summary figure for each chapter.

2.8. Shipboard samples

Samples for shipboard analyses were taken from the working half of cores, from the residues of whole-round IW squeeze cakes, or from the whole-round core catcher section. These samples are indicated in the shipboard samples column on the VCDs as follows:

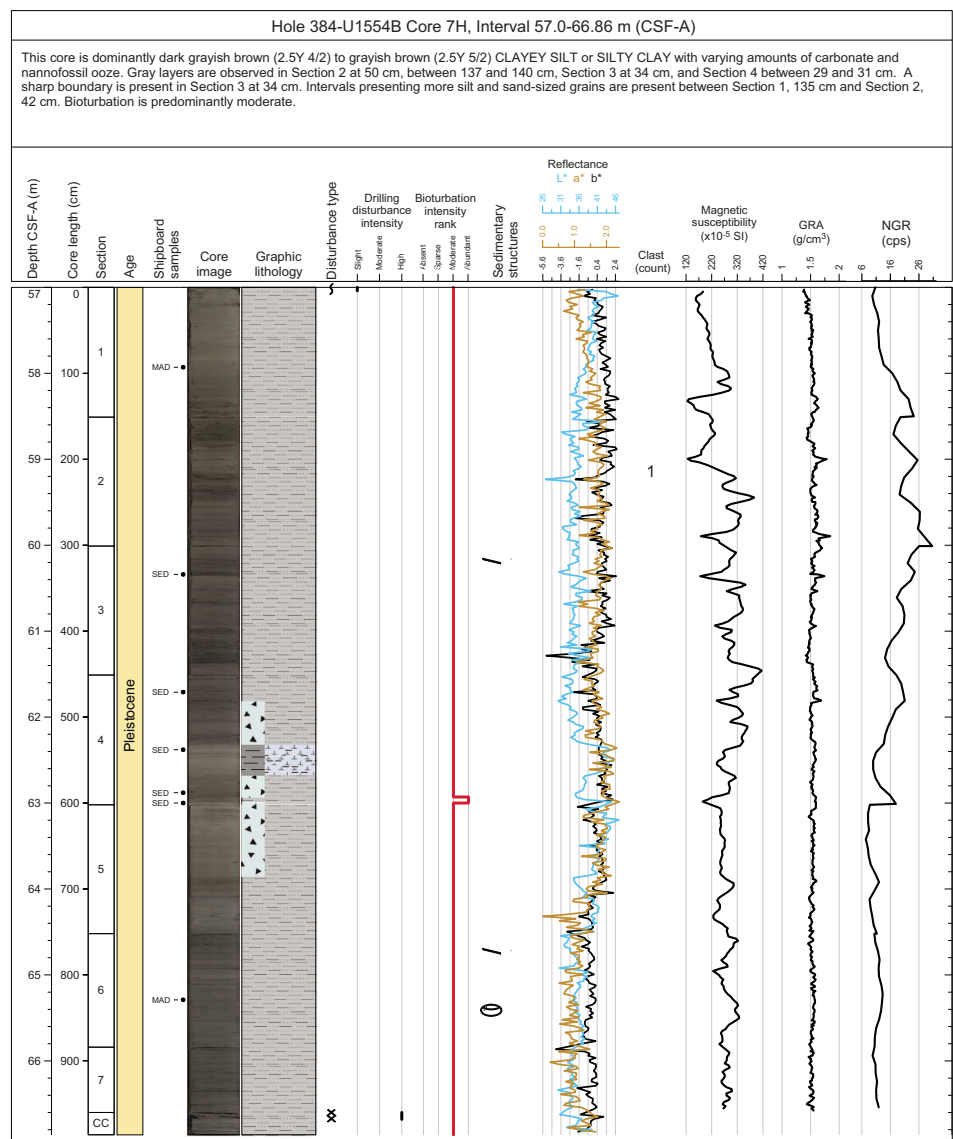


Figure F8. Example VCD, Expedition 395.

- CARB = sample to measure weight percent calcium carbonate.
- HS = headspace sample, to measure formation gas concentrations (see [Geochemistry and microbiology](#)).
- IW = interstitial water sample, whole round removed from the core; residues from this sample were often used for other analyses such as XRD (see below).
- MAD = moisture and density sample.
- SED = smear slide sample.
- PAL = portion of core catcher for biostratigraphy.
- PMAG = paleomagnetic cube taken for postcruise research.
- NANNO = smear slide taken to identify nannofossils (in addition to PAL samples).
- FORAM = sample taken to identify foraminifers (in addition to PAL samples).
- XRD = sample taken for shipboard XRD analysis, usually a split of the IW residue (see [Geochemistry and microbiology](#)).
- NOTESTS = whole-round sample, not generally used for analyses as taken, but split into samples for other analyses previously listed in instances when IW samples were not collected.

2.9. Bioturbation

Bioturbation was noted in the macroscopic sediment template in GEODESC DataCapture. Four levels of bioturbation were identified:

- Absent: no visible bioturbation. This could mean no bioturbation or complete homogenization of the sediment from bioturbators.
- Sparse: 1%–10% of split core surface area contains visible bioturbation.
- Moderate: >10%–50% of split core surface area contains visible bioturbation.
- Abundant: >50% of split core surface area contains visible bioturbation.

2.10. Drilling disturbance

Deformation and disturbances of sediment that clearly resulted from the coring process were described in a separate template in GEODESC DataCapture. Deformation and disturbances of

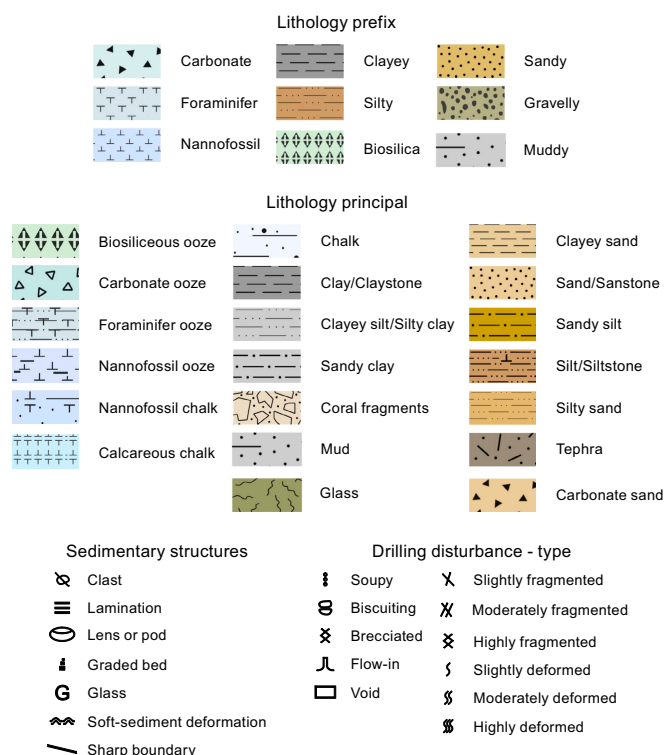


Figure F9. VCD legend, Expedition 395.

sediment are illustrated in the Disturbance type column of the VCDs, and the intensity of the drilling disturbance is plotted in the Drilling disturbance intensity column (Figure F9). Drilling disturbance intensity was classified into four categories:

- Absent (<1%),
- Slightly disturbed (1%–10%),
- Moderately disturbed (>10%–50%), and
- Highly disturbed (>50%–100%).

The definitions of drilling disturbance terms are consistent with nomenclature of Jutzeler et al. (2014) and the method of Expedition 339 Scientists (2013) unless otherwise noted and are as follows:

- Biscuiting: breakage of semilithified core into disc-shaped pieces, often separated by remolded mud (also known as gravy) that is a mixture of pulverized sediment and drilling fluid.
- Brecciated: firm sediments that are pervasively broken and may be displaced or rotated.
- Deformed: soft-sediment bedding contacts that are disturbed and bent.
- Fall-in: debris in the top of a core that fell into the borehole from shallower depths during the coring process.
- Fragmented: indurated sediment displaying breakage.
- Uparching: soft-sediment layers in the plastic core liner bending down around the cut periphery due to friction between the sediments and core liner; this is generally observed in piston cores.
- Soupy: intervals that are water saturated and have lost all aspects of original bedding.
- Void: an interval that has no core material. A polystyrene foam spacer may be added to the core after splitting to preserve the integrity of the remaining material.

2.11. Expeditions 384 and 395C

Because of the COVID-19 pandemic, only IODP technical staff sailed on Expeditions 384 and 395C. A simplified workflow was adapted for shipboard measurements including all physical properties measurements and imaging with the track systems. A subset of the Expedition 395 science party traveled to the GCR for core description after these two expeditions in 2022. As a result of the time lapse between core collection and description, significant sediment oxidation may have occurred. Consequently, color descriptions may not be consistent between Expedition 395 and Expeditions 384 and 395C. Moreover, additional scraping of core surfaces was required for cores from Expeditions 395C and 384 prior to description.

3. Igneous petrology

We adapted rock core description procedures from Expeditions 367/368 (Sun et al., 2018) and 385 (Teske et al., 2021) with the primary goal of systematically describing the physical appearance, petrology, mineralogy, and alteration of recovered igneous rock material. Phenocryst abundance and appearance, vesicularity, extent of alteration, igneous textures, and morphological characteristics were first described at a macroscopic level and then investigated in more detail using thin sections.

Because of COVID-19 protocols during Expeditions 384 and 395C, cores from these expeditions were described at the GCR during May 2022. One benefit of this approach is that it allowed most of the petrology team to visually examine the cores together and reach a general consensus regarding methods and observations. To the extent possible, we used the same procedures and terminology for shipboard core description during Expedition 395 (Site U1564). The resulting core description data were entered into the customized GEODESC software application.

3.1. Core description

For all igneous rock cores, we conducted a visual core description, thin section sampling and description, digital color imaging, and color reflectance spectrophotometry. During Expeditions

395 and 395C, we also measured V_p and conducted shipboard pXRF and ICP-AES analysis (see **Geochemistry and microbiology**). Prior to splitting the cores into working and archive halves, each whole-round section was subjected to nondestructive physical properties analysis (see **Physical properties**). During Expedition 384, additional whole-round samples were taken from Holes U1555F and U1555G for engineering tests (Blum et al., 2020) and whole-round imaging was not conducted. During Expeditions 395C and 395, each whole-round section was imaged using the SHIL (see **Physical properties**) on a wet surface at four different angles (0°, 90°, 180°, and 270°). These images were then combined to create a 360° whole-round image for each core section. Whole-round core samples selected for microbiological analysis and partial sampling were photographed using a high-resolution digital single-lens reflex camera. This step was necessary because the whole-round microbiological sample—generally ~5 cm in length, depending on the abundance of veins and amygdules—was taken before the core sections were imaged (see **Geochemistry and microbiology**). Following subsampling of the microbiological whole-round core pieces, the leftover material was returned and the presampling photograph was used to help reconstruct the section interval. After microbiological sampling, splitting lines were drawn using a wax crayon by a shipboard technician (Expeditions 384 and 395C) and/or a petrologist (Expedition 395) to preserve compositional and structural features in archive and working halves. The cores were then split using a diamond-impregnated saw along the splitting lines. Afterward, fragments of igneous rock that fit together were assigned a joint number and labeled with a letter in consecutive order downsection (e.g., 1A, 1B, and 1C). Plastic spacers were mounted in the split liners to separate pieces with different numbers. For single pieces that showed no evidence of rotation, an arrow pointing to the top of the section was added to the labels to indicate orientation.

We used the archive half for macroscopic investigation and the working half for sampling (either shipboard or at the core repository, as required). Scanning the cut dry and wet archive-half surfaces using the SHIL produced high-resolution color images. Then, color reflectance and MSP were measured at steps of 2 or 2.5 cm on the archive-half surfaces using the SHMSL (see **Physical properties**), and pXRF analyses were conducted (see **Geochemistry and microbiology**). The working halves were sampled for destructive shipboard analyses such as paleomagnetic and MAD measurements, thin section preparation, and geochemical analyses using ICP-AES. Most of the samples chosen for ICP-AES analyses were from the same piece taken for thin section petrography.

We first examined the archive-half sections of each core at the macroscopic level (aided by a 10× magnification field hand lens and a binocular microscope), describing primary (igneous) and secondary (alteration) petrologic characteristics. Afterward, the sampled thin sections were observed and described using a petrographic microscope (up to 40× magnification). For both macroscopic and microscopic observations, we used GEODESC to record igneous characteristics (e.g., groundmass, phenocryst mineralogy, and vesicle size and abundance) and alteration features (e.g., color, vesicle filling, secondary minerals, and vein/fracture fillings; see **Alteration petrology and structural geology**).

3.2. Macroscopic visual core description

VCDs present select macroscopic core observations and features. For consistency, we used the same VCD format for all three expeditions. The hard rock VCDs include the following features, from left to right (Figures **F10**, **F11**):

- CSF-A depth scale (meters below seafloor);
- Core length scale from 0 to 150 cm;
- Location of shipboard samples, including thin sections (TS), inductively coupled plasma spectroscopy (ICP), cubes for magnetics (PMAG), microbiological samples (MBIO), and engineering samples (ENG);
- Scanned digital image of the archive half;
- Graphic representation of lithology;
- Symbol “G” (next to the graphic lithology), which indicates the presence of volcanic glass in the glassy rind of chilled margins or as fragments (e.g., in volcanic breccia);
- Igneous lithologic unit number;

- Symbols denoting vein type and connectivity, as well as the location of major vesicle bands;
- Graphic representation of average vesicle abundance;
- Stacked line chart displaying percent phenocryst abundance for olivine (OL; green line), plagioclase (PLAG; red line), and clinopyroxene (CPX; blue line), if present;
- Line chart displaying groundmass grain size categorization;
- Line chart displaying alteration intensity;
- Color bar denoting alteration color;
- Plot showing whole-round MS measurements; and
- Description summary of the section and each igneous lithologic unit identified therein.

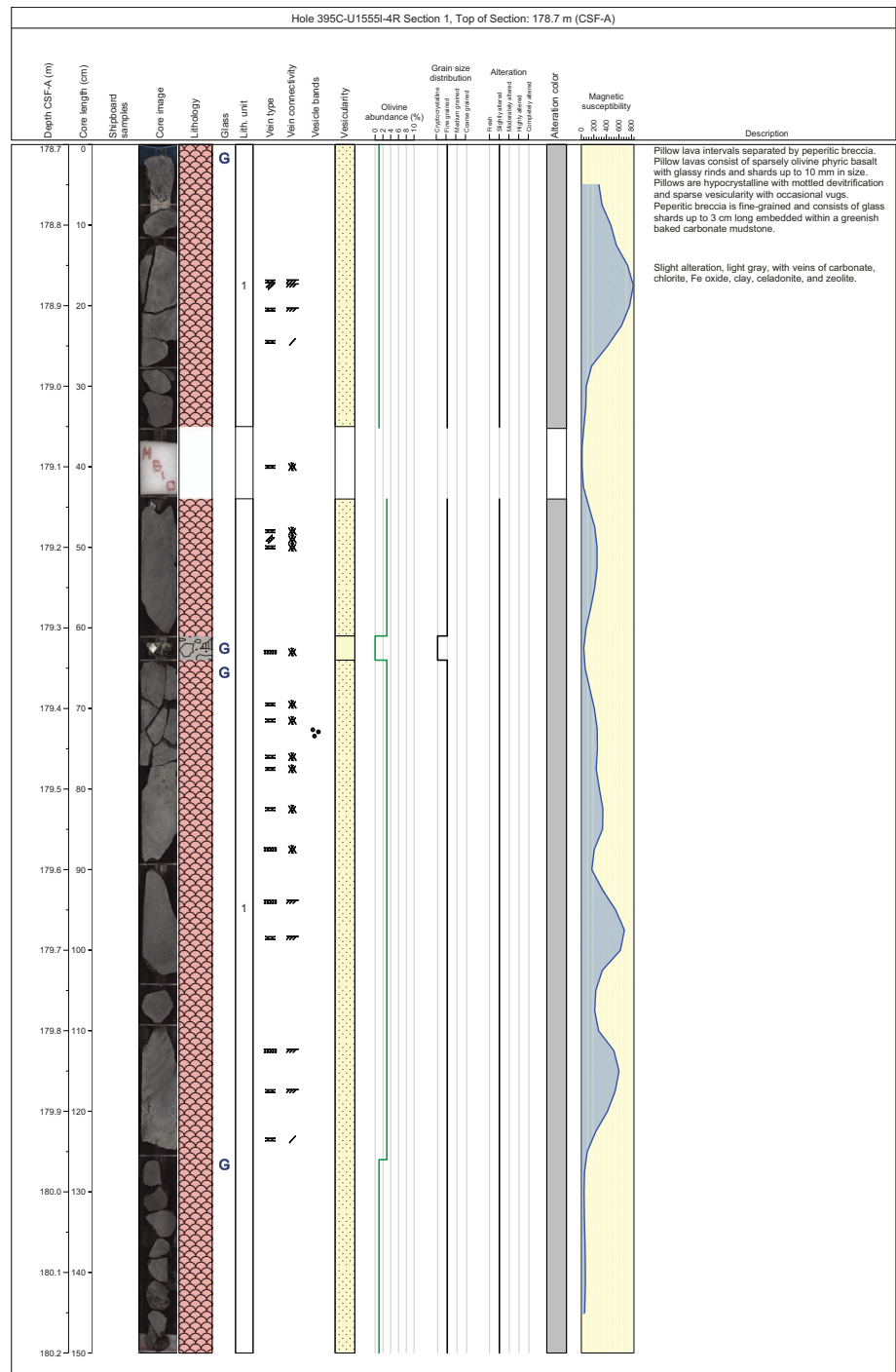


Figure F10. Example igneous rock VCD. See Figure F11 for legend.

3.3. Igneous lithologic units

Igneous units were classified on the basis of primary modal composition, groundmass texture, and any identifiable flow morphology. We defined igneous lithologic unit boundaries when there were significant changes in rock type (e.g., a transition from basalt to a sediment-rich horizon) or phenocryst assemblage (e.g., olivine phyric to plagioclase phyric). In practice, most sites exhibited minimal variations in mineral assemblage at the hand specimen scale, so the majority of lithologic unit divisions were based on the presence of significant carbonate mudstone or peperite horizons. Closely intercalated intervals were grouped to avoid repetitive entry at the small-scale level with dubious significance (e.g., a pillow lava unit with multiple horizons of intercalated peperite near the top or bottom, grading to sediment-poor basalts).

Because of incomplete recovery and a general lack of well-defined contacts, these unit boundary locations are approximate and preliminary. All igneous units were numbered downhole (i.e., Igneous Lithologic Unit 1, 2, 3, and so on).

3.3.1. Rock classification and description

Igneous rocks were classified based on the International Union of Geological Sciences (IUGS) system (Le Maitre et al., 2002). We assigned rock names based on macroscale observations of groundmass texture/color and dominant phenocryst phases, if present. All basement rocks recovered during Expeditions 384, 395C and 395 were classified as basalt because of their dark gray color and micro- to cryptocrystalline groundmass with minor amounts of olivine and plagioclase; this designation was later confirmed through geochemical analysis. Porphyritic rocks were named by phenocryst type and relative abundances as follows:

- Aphyric: phenocrysts constitute <1% of the rock volume.
- Sparsely phyric: phenocryst content ranges 1% to <5%.
- Moderately phyric: phenocryst content ranges 5%–10%.
- Highly phyric: phenocryst content >10%.

When phenocrysts were observed, we documented the mineral, abundance, and shape (e.g., anhedral, subhedral, and euhedral).

3.3.1.1. Groundmass

We characterized the groundmass of all igneous rock core sections based on average grain size and extent of crystallization. All rock core intervals were described macroscopically, and a subset was assessed microscopically where thin sections were taken (see [Microscopic description](#)).

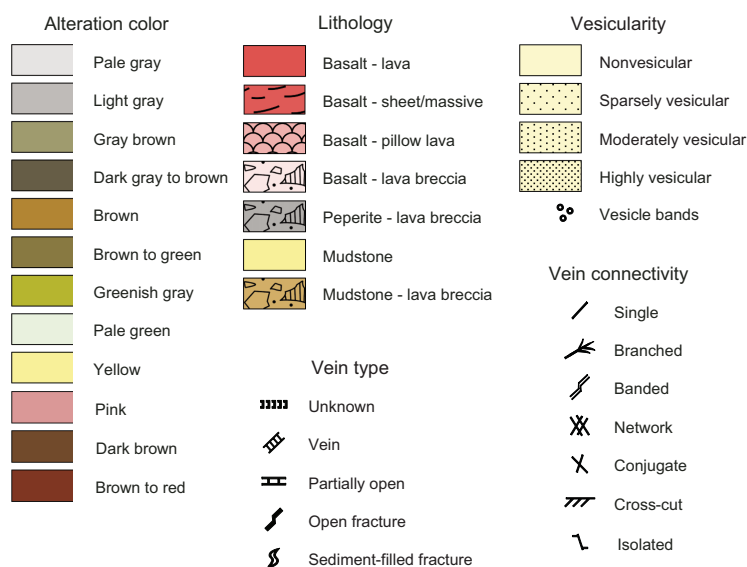


Figure F11. Igneous rock VCD legend, Expedition 395.

The average grain size was assigned at the macroscale using the following schema, with more detailed description of groundmass texture provided through thin section observation:

- Cryptocrystalline (<0.1 mm),
- Fine grained (>0.1–1 mm),
- Medium grained (>1–2 mm), and
- Coarse grained (>2 mm).

Groundmass crystallinity was characterized using the following categories:

- Holohyaline (vitric; only glass),
- Hypohyaline (comprising both crystals [minor component] and glass),
- Hypocrystalline (comprising both crystals [major component] and glass), and
- Holocrystalline.

When glass was present in an interval, we estimated the proportion of fresh and altered glass and noted the form of its occurrence (e.g., thin glass rinds, shards, or larger fragments). Other features of interest, such as particularly abundant fresh glass, devitrification, or gradations in grain size, were noted in the groundmass comments for that interval.

3.3.1.2. Vesicularity

Vesicles were primarily characterized by their size and abundance. Vesicles were often filled with secondary minerals, which were described in more detail during alteration logging (see [Alteration petrology and structural geology](#)). Abundance categories were defined as follows:

- Nonvesicular (<1% of the rock volume),
- Sparsely vesicular (1%–<10%),
- Moderately vesicular (10%–20%), and
- Highly vesicular (>20%).

Additional observations regarding vesicle shape (e.g., spherical, irregular vugs, and pipe vesicles) and general distribution were also noted. Vesicle concentration can vary significantly within a single lava flow or pillow lobe, and we commonly encountered bands and patches with higher vesicle concentrations in the core sections. We estimated the vesicle abundance within these bands and noted their location to distinguish them from the lower overall vesicularity of the interval.

3.3.2. Rock interpretation

To examine the nature of volcanic processes in the recovered core sequence, we further categorized basaltic intervals by their flow morphology. We applied the following classification scheme for lava flow types (for example images, see [Figure F12](#)):

- Pillow lava: 0.1–1 m in thickness with curved chilled margins (often glassy), spherulitic textures, and cryptocrystalline groundmass that decreases in grain size toward the glassy rims.
- Sheet/massive flows: thicker flows (1–3 m or more) that are more texturally uniform, sparsely vesicular, and characterized by a gradual increase in grain size toward the center of the flow. In addition to sheet flows associated with high-discharge rates, this category may include ponded lavas and similar forms in which individual lobes tend to coalesce.
- Lava: a generic term used when flow morphology is ambiguous and/or transitional between pillow lavas and sheet flows. This category likely includes many large pillows or lobate flows (1–2 m thick).
- Lava breccia: lava clasts within a sedimentary matrix. This category includes peperite, a sediment-matrix igneous breccia likely formed by lava mingling with or intruding into wet and/or unconsolidated sediment (after White et al., 2000).

3.3.3. Contact types

Glassy margins, chilled margins, and contact boundaries were documented for the top and bottom of each interval when observed. Contacts may be curved, irregular, or planar in shape, with sharp or gradational boundaries. We also noted whether they were (sub)horizontal, inclined, steeply dipping, or vertical. The following contact types were defined and described:

- Baked contact: boundary with sediments overprinted (baked).
- Chilled contact: lava that has clearly chilled against sediment or another rock unit.
- Chilled margin: rapidly chilled margin, for example with a cryptocrystalline border, or incomplete variolitic to glassy selvage.
- Contact not recovered.

We also noted our interpretation of contacts during the core description (e.g., the top or bottom of a lava flow, a unit boundary, the edge of a pillow lobe, and so on). Because it can be difficult to distinguish the top of a flow or lobe from the top of an eruptive unit, particularly in core sections with abundant pillow basalts and incomplete recovery, we caution that contacts designated as the top of a flow should not be interpreted as a boundary between eruptive units (although some likely are).

3.4. Microscopic description

We used thin section observations to complement and refine macroscopic rock core observations (Figure F13). Thin section descriptions include both primary (igneous) rock-forming minerals (including phenocrysts and groundmass) and a brief description of the nature and extent of alter-

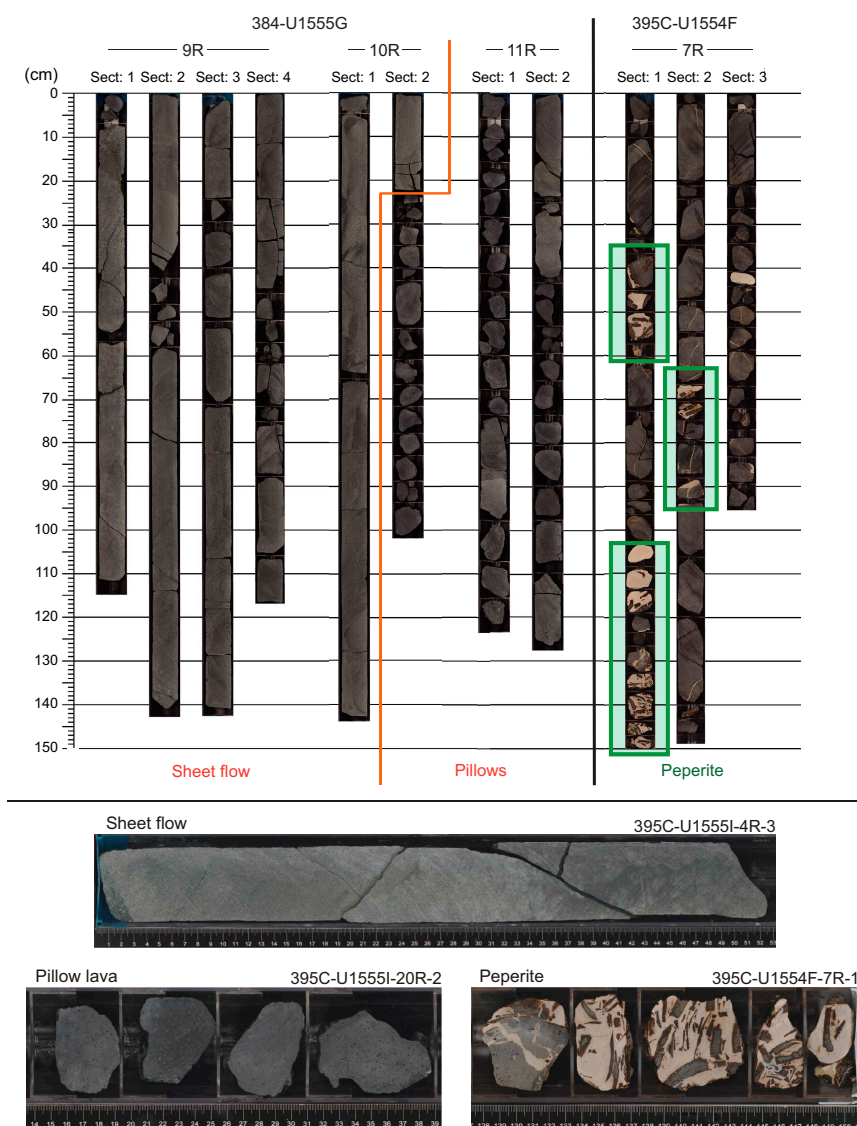


Figure F12. Sheet flows, pillow lavas, and peperite, Expedition 395. Orange line = transition from fairly continuous pieces of sheet flow lava to small pillow lava fragments.

ation. For each thin section, we documented the minerals present, their abundance (modal volume percent), size, shape, habit, and textural relationships. We also described the groundmass mineralogy and texture, vesicularity (abundance, size, and shape), glass abundance, and alteration. All thin section observations were entered into GEODESC using a customized thin section template.

Thin section descriptions include the following terms:

- Thin section domain: a summary description of the thin section or of each domain on the slide if it contains multiple domains (e.g., a slide that shows a large sedimentary vein [25% of the slide] in a basaltic matrix [75% of the slide]).
- Mineral shape: the dominant (>50% of crystals) shape of the olivine (ol), plagioclase (plag), and clinopyroxene (cpx) crystals in euhedral, subhedral, and anhedral shapes.
- Mineral habit: the dominant (>50% of crystals) habit of olivine, plagioclase, clinopyroxene crystals in equant, subequant, tabular, rounded, elongate, skeletal, acicular, hopper, or swallowtail.
- Plagioclase zoning: not observed, variable extinction, undulose extinction, oscillatory, sector zoning, patchy zonation, and other related observations.
- Plagioclase extinction: when measured, extinction angles are provided along with the estimated anorthite (An) content.
- Clinopyroxene habit: description of (groundmass) clinopyroxene, including interstitial, dendritic, mesostasis, and subophitic texture.

Additional features such as glomerocrysts and other aggregated clusters, alteration features and extent, and inclusions are also noted in the comments.

3.5. Chemical analysis

A handheld pXRF unit was used to conduct rapid in situ chemical analysis of rock surfaces (archive half) during Expeditions 395C and 395 (see [Geochemistry and microbiology](#)). Previous

THIN SECTION LABEL ID: 395C-U15551-27R-2-W 104/107-TSB-TS 1 Observer: Callum Pearman, Gabriel Pasquet, Tao Wu, David McNamara Piece no.: Lithology: sparsely olivine phyric basalt Thin section summary: Nearly phenocryst-free. Very few small olivines (<0.5 mm) are observed (<5%). Plagioclases (0.1-2 mm) are most abundant crystals (30%). Most of them are elongate (80%) with some grains that are skeletal tabular to prismatic (20%). Zone texture is not observed in plagioclase. Groundmass shows intergranular and intersertal texture. Space between plagioclases occupied by olivine microcrystals, mesostasis, altered cpx mesostasis, opaque oxides, and altered glass. Phenocrysts heavily altered into saponite±chlorite. Altered saponite mesostasis may contain cpx. Saponite, celadonite and FeO/OH vesicle infilling.							
Plane-polarized:				Cross-polarized:			
							
Igneous Petrology							
Groundmass: Olivine, mesostasis, altered cpx mesostasis, opaque oxides magnetite and altered glass.							
Alteration: Moderate-high. Groundmass is altered to saponite and FeO/OH. Olivine phenocrysts heavily altered to saponite±chlorite. Oxidized and saponitized groundmass. 100% filled vesicles by saponite and some celadonite+FeO/OH.							
Mineral	%	Size min. (mm)	Size max. (mm)	Size ave. (mm)	Shape	Habit	Comments
Olivine	2	0.025	0.5	0.1	subhedral	subequant	
Plagioclase	30	0.03	2	1	subhedral	elongate	Thin crystals, skeletal/swallowtail grains common
Clinopyroxene							Mesostasis

Figure F13. Example igneous rock thin section report, Expedition 395.

IODP expeditions demonstrated the utility of pXRF to provide quick chemical characterization of igneous rocks encountered in the core (e.g., Reagan et al., 2015; Ryan et al., 2017). Such data can be valuable for assessing broad chemical variations, determining potential unit boundaries, and helping target areas of interest for sample selection. In addition, samples were taken for shipboard ICP-AES analyses, usually coincident with thin section sampling (average of 1 sample per ~10 m when material was suitable). See [Geochemistry and microbiology](#) for pXRF and ICP-AES analytical procedures and calibrations.

4. Alteration petrology and structural geology

This section describes the procedures used for visual observations of alteration style, mineralogy, fracturing, and fracture and vesicle filling mineralogy in basalt cores from Expeditions 384, 395C, and 395. Descriptions were based on visual assessment of split cores, optical microscopy of sampled thin sections, and analysis using a scanning electron microscope (SEM) coupled with energy dispersive spectrometry (EDS) on selected thin sections. The resulting alteration observations, structural features, and thin section descriptions were recorded in GEODESC and are summarized in the site chapters.

4.1. Alteration

Estimates of the degree of alteration of the basalt core are reported for Holes U1554E, U1554F, U1555F–U1555I, U1562A, U1562B, U1563A, U1563B, and U1564F. Degree of alteration is assessed based on a visual estimate of the percentage of a core interval that has been altered to a secondary mineral assemblage; it is then assigned a corresponding rank (Table T1).

For a given core interval, the total percent of altered core is divided by the relative proportions of bulk disseminated alteration, alteration occurring in patches, or alteration occurring as a halo around a fracture (termed background, patch, and halo, respectively). A descriptive color is assigned to the alteration of the core interval. If more than one color is observed, the reported color is the dominant alteration color. Alteration mineralogy (Fe-oxide/oxyhydroxide, chlorite, clay, celadonite, quartz/silica, zeolite, carbonate, and sulfide) is visually assessed and presented as a modal percent of the total degree of alteration. It should be noted that for Sites U1554, U1555, U1562, and U1563, chlorites and different clays have been grouped together and described under the term “phyllosilicate.”

Finally, vesicles and vug spaces in a given core interval are visually assessed for the percent of these spaces that are filled with secondary minerals, the dominant color of these mineral fills, and secondary mineral assemblage where identifiable. For the latter, vesicles and vugs that show multiple mineral fills or variable color in their mineral fill are reported as zoned.

Table T1. Core alteration, Expedition 395. [Download table in CSV format.](#)

Percent of core altered	Descriptor	Rank	Description
0	Fresh	1	Core interval is fresh and contains no visible secondary mineralization or is basaltic glass.
>0 to ≤25	Slightly altered	2	Core interval displays mostly preserved texture and mineral composition, with small amounts of secondary mineralization weakly disseminated throughout the core or concentrated in small patches or as narrow halos around a fracture/vein. Core may display slight color variations from its original fresh state.
>25 to ≤50	Moderately altered	3	Core interval displays weak preservation of primary texture and mineral composition. Secondary mineral assemblages are more pervasive throughout the sample or as large patches or wide halos around fractures/veins. Core displays a color different from that of fresh rock.
>50 to ≤75	Highly altered	4	Core interval displays limited preservation of original texture or mineral composition, and secondary mineralization is pervasive or exists as very wide alteration halos around fractures/veins that comprise most of the observable core. Core color is markedly changed from its fresh color.
>75 to ≤100	Completely altered	5	Core interval shows little to no primary texture or mineral composition preservation, and secondary mineralization dominates the core composition. Core color is markedly different from that of fresh basalt core.

4.2. Structural geology

The term fracture is used here to refer to any observed mineral vein or any natural break in the core. The latter are identified only when a broken surface shows mineralization, slickensides, or observable and traceable offset geologic features across it. Top and bottom depths of each fracture are recorded as they occur in the core assuming that all core pieces are in their in situ orientation with respect to the borehole axis. Fracture properties were individually assessed for Holes U1554E, U1554F, U1555F–U1555I, U1562A, U1562B, U1563A, and U1563B. Individual fracture measurements are detailed in Table T2.

For Holes U1554E, U1554F, U1555F–U1555I, U1562A, U1562B, U1563A, and U1563B, individual fractures were visually assessed to identify alteration minerals present and estimate the percent abundance of the total fracture fill. Mineral species visibly assessed with confidence from core are carbonate, phyllosilicates (or clay and chlorite), epidote, Fe-oxides/oxyhydroxides, quartz/silica, celadonite, and zeolite. Finally, the width (to the nearest millimeter) and color of alteration halos around fractures are reported where present.

4.3. Thin section analysis

Thin sections of basalt core sampled from Holes 395C-U1554F, 395C-U1555I, 395C-U1562B, 395C-U1563B, and 395-U1564F were examined and described for alteration using a Zeiss Stereo binocular microscope. Thin sections of basalt core from Holes 384-U1555F and 384-U1555G were unavailable for examination during Expedition 395 and were therefore described on shore using a Nikon LV150ND optical microscope. Thin sections were examined under plane-polarized light (PPL), cross-polarized light (XPL), and reflected light (RL). PPL and XPL permit the identification of most minerals in the alteration mineral assemblage, and RL allows investigation and identification of optically opaque minerals. Alteration descriptions of the thin sections focused on identifi-

Table T2. Fractures, Expedition 395. [Download table in CSV format.](#)

Fracture descriptor group	Description	Fracture descriptors
Fracture type	Degree of mineral fill in structure	Unknown: only one side of the fracture is observable (unmated), which is mineralized or bears slickenlines Partially open: the fracture is not completely mineralized; some open space remains Vein: the fracture is completely mineralized; no open space remains
Fracture color	Dominant mineral fill color	
Fracture width (mm)	Measured perpendicular across structure (true width)	Measured with ruler in mm when width is ≥ 1 mm; recorded as 0.5 for fractures < 1 mm wide Null value when only one side of a structure is observable (unmated fractures)
Fracture shape	Morphology of individual fractures	Planar: single, isolated fracture has a simple planar structure Curvilinear: single, isolated fracture has a simple curvilinear structure Parallel: single planar to curvilinear fracture has a parallel to near-parallel orientation to another nearby single planar to curvilinear fracture Anastomosing: single fracture has a complex morphology Y-shaped: single fracture displays a single Y-shaped splay morphology at either or both ends T-shaped: single fracture displays a single T-shaped splay morphology at either or both ends Splayed: single fracture displays multiple morphologically complex splays at either or both ends Stepped: single fracture displays a stepped-like morphology along its length En echelon: single fracture displays an en echelon morphology
Fracture connectivity	How a structure interacts with other structures on the drill core	Crosscut: single fracture observed to cut across or be cut across by another fracture Network: single fracture forms a morphologically complex network with more than one other fracture
Fracture mineral texture	Macroscopic appearance of mineral fill	Single: single fracture with no connection to another fracture Amorphous: vein fill appears amorphous Crypto-microcrystalline: vein fill is crystalline but not large enough to measure Crystalline: vein fill is crystalline with crystal sizes ≥ 0.5 mm Layered: vein fill shows obvious layering of one or more minerals
Fracture attitude	Visual description of the orientation of a structure with respect to the core axis	Horizontal: fracture oriented 80° – 90° to core axis Subhorizontal: fracture oriented 60° – 80° to core axis Inclined: fracture is oriented 30° – 60° to core axis Subvertical: fracture is oriented 10° – 30° to core axis Vertical: fracture is oriented 0° – 10° to core axis
Average fracture mineral crystal size (mm)	Average crystal size of observable vein fill	Measured to the nearest mm if crystals are obviously ≥ 0.5 mm to the naked eye, otherwise a null value is reported

cation of the alteration mineral assemblages of both the groundmass and phenocrysts, as well as description of minerals found within vesicles and fractures.

4.4. Scanning electron microscope and energy dispersive spectrometry

During Expedition 395, an SEM with an EDS detector was used to perform analyses on a selection of basalt core thin sections sampled from Holes 395C-U1554E, 395C-U1555I, 395C-U1562B, and 395C-U1563B (SNE-4500M Plus SEM with a Bruker Quantax EDS detector). The SEM scans the surface of a thin section with a focused electron beam generated from a tungsten filament under vacuum. This beam causes the sample to emit electrons, which are collected by detectors in the SEM and used to produce an image. The same electron beam that images the thin section surface excites the sample, causing it to dissipate absorbed energy by ejecting a core-shell electron. This ejected electron is replaced by a higher energy outer-shell electron, releasing energy as an X-ray as it does so. The X-ray generated by this process has a characteristic spectrum based on the elemental atom it comes from. The positions of the peaks in the generated X-ray spectrum identify a sample's elemental composition, and the intensity of the signal corresponds to concentration of the element. As the electron beam is rasterized across a zone of interest on the sample surface, it generates a map of approximate elemental abundances that, for geologic samples, can be used to identify mineralogy and texture.

Selected basalt thin sections were carbon coated via a single carbon thread evaporation in a Leica EM ACE200 under vacuum using 15 pulses to generate a sufficiently thick coating. The Nanoeye software was used for SEM operation. Thin sections were imaged and analyzed with EDS at a working distance from the electron beam of 6 mm using an accelerating voltage of 15 kV and an emission current of 110 μ A. Images were acquired using a secondary electron detector.

Once an image was captured, the Esprit Compact software was launched to perform EDS data acquisition. The EDS detector was configured for pulse throughput, maximum energy (which was set automatically for Expedition 395 analyses), and dwell time (which was set at 16 μ s).

For the analyses performed during Expedition 395, we selected Si, O, Mg, Fe, Al, Ca, Na, K, S, Cl, Ti, Mn, Sr, and Ba. Carbon (C) was automatically detected and can be useful for characterizing carbonate minerals in samples but has a strong presence across the entire sample due to the carbon coating.

During Expedition 395, specific elements were chosen to define specific minerals: Si for quartz or amorphous silica, Mg for olivine, Al for plagioclase, Fe for oxides or groundmass pyroxene, Ca for calcite, and K for celadonite. Other altered phases like saponite or chlorite were shaded based on Mg abundance. Also, minor elements were useful to display zonation in a single phase and/or mineral.

Multiple options for EDS data acquisition were available: “map mode” collects EDS across the entire imaged portion of the sample, “object mode” collects EDS data from single points and defined polygons of the imaged sample, and “line mode” generates EDS data along a defined line across a region of interest on the imaged sample. This SEM-EDS methods guide was adapted from the SEM-EDS Bruker Quick Start Guide available on the Laboratory Manuals, Guides, and Resources page on the *JOIDES Resolution* Laboratories website (<https://tamu-eas.atlas-sian.net/wiki/spaces/LMUG/pages/7341015792/SEM-EDS+Bruker+Quick+Start+Guide>).

5. Micropaleontology

Biostratigraphy was based on calcareous nannofossils, planktonic foraminifers, and bolboforms that were studied in core catcher samples from all sites. Additional samples were taken from section halves at some sites to provide more refined age determinations or investigate particular levels of interest. Because of the COVID-19 pandemic, samples from Expedition 395C were shipped to participating micropaleontology laboratories for processing and study at the end of the expedi-

tion rather than being studied shipboard. Samples from Expedition 395 were processed and analyzed for microfossil content on board during the expedition.

Biostratigraphy focused mainly on the identification of biostratigraphic horizons (biohorizons) in the cores, generally the top (T) or base (B) of the stratigraphic range of a species but also including top common (Tc) and base common (Bc) occurrences. For nannofossils, we used the top acme (Ta), base acme (Ba), base paracme (Bpa), top paracme (Tpa), and crossover in abundance between two species (X). For planktonic foraminifers, we used coiling direction changes (X_{d-s} for dextral to sinistral and X_{s-d} for sinistral to dextral, as viewed upsection) in certain species. Biohorizons are assumed to result from biological events (bioevents) such as migrations, extinctions, and evolutionary transitions. These biohorizons have been assigned absolute ages based on calibrations from other sites, mainly referenced to the paleomagnetic reversal sequence. These ages may or may not be accurate for the study sites because of diachrony and/or imprecise calibration, especially when applying tropical or subtropical calibrations to these high-latitude successions. Identification of biohorizons in stratigraphic order allowed the identification of biostratigraphic zones (biozones, often referred to simply as zones). Details of the schemes for calcareous nannofossils, foraminifers, and bolboforms are provided in [Calcareous nannofossils](#), [Planktonic foraminifers](#), and [Bolboforms](#), respectively.

For each site and each fossil group, a table of biohorizon depths was prepared. These tables were used in conjunction with the paleomagnetic reversal records to construct age versus depth plots for each site (see [Age model](#)).

For each site, the paleomagnetic and biostratigraphic data were collated on a common geologic timescale (see [Age model](#)). For the Paleogene, calibrated ages from Agnini et al. (2014) for calcareous nannofossils and Wade et al. (2011) for planktonic foraminifers were updated to the geomagnetic polarity timescale (GPTS) of Speijer et al. (2020).

For division of the formal series of the timescales and their geochronologic equivalent epochs, we use informal subseries/subepoch terms such as upper Pliocene when referring to strata and late Pliocene when referring to time. These have a lower case modifier to emphasize their informal status.

5.1. Calcareous nannofossils

Calcareous nannofossil assemblages were examined and described from standard smear slides made from core catcher samples (at about 10 m intervals) during Expedition 395 in multiple holes at each site. Additional toothpick samples were taken between core catcher samples from section halves, where possible, to refine the stratigraphic position of bioevents. Standard smear slides were made from bulk sediment. Slides were fixed with Norland optical adhesive Number 61 and cured under UV light for immediate biostratigraphic examination using a Zeiss Axioscope. Samples were analyzed under plane-transmitted, cross-polarized, phase contrast, and/or circular-polarized light using oil immersion at 1000 \times magnification. All photomicrographs were taken using a Spot Flex camera with IODP Image Capture 3.0 and Spot commercial software. Additional observations of sediment samples from some sites were made with a Hitachi TM3000 tabletop SEM to identify *Emiliana huxleyi* and verify the preservation state of calcareous nannofossils.

Nannofossil taxonomy follows Perch-Nielsen (1985), Young (1998), and Young and Bown (2014) as compiled in the online Nannotax 3 (<https://www.mikrotax.org/Nannotax3>) database. The zonal scheme of Martini (1971) was used for calcareous nannofossil biostratigraphy (Neogene NN code; Paleogene NP code) (Figure [F14](#); Table [T3](#)). This zonation represents a general framework for the biostratigraphic classification of middle- to low-latitude nannofossil assemblages. The zonal scheme of Backman et al. (2012) as modified by Raffi et al. (2020) (CNPt-CNPI-CNM code), along with that of Agnini et al. (2014) for the Paleogene (Oligocene CNO code), providing a secondary framework that is more detailed in some intervals, is also shown. Zone NN13/14 is undifferentiated due to difficulties placing base common occurrence *Discoaster asymmetricus* and the poor calibration of this event (see discussion in Backman et al., 2012).

Biohorizons and bioevents, including age assignments, follow the latest compilation of Raffi et al. (2020) (Table T3). To this compilation we add two markers for the Oligocene/Miocene boundary: the top of *Cyclicargolithus abisectus* larger than 11 µm and top *Reticulofenestra bisecta*. Although neither of these bioevents are well calibrated and both may show some degree of latitudinal diachrony, they do have a long history of being used to broadly mark the Oligocene/Miocene boundary and/or as a temporal equivalent of the calcareous nannofossil Zone NP25/NN1 boundary across the Southern Ocean, equatorial Atlantic and Indian Oceans, and the Mediterranean Sea. Okada and Bukry (1980) noted an acme of large *C. abisectus* morphotypes at the top of the Oligocene in the Pacific and used the top of this event (the last common occurrence) as a subzonal marker. In the Indian Ocean, the top of these large forms, defined as >10 µm, consistently falls close to top *Furcatolithus ciproensis* (24.35 Ma on timescale of Speijer et al., 2020) and top *R. bisecta* (Ocean Drilling Program [ODP] Sites 707–710 and 714), and at all these sites it falls below base *Sphenolithus delphix* (23.73 Ma) (Rio et al., 1990). A larger size cutoff of 11 µm was suggested for the biostratigraphic use of *C. abisectus* (Olafsson, 1992) based on the detailed morphometric

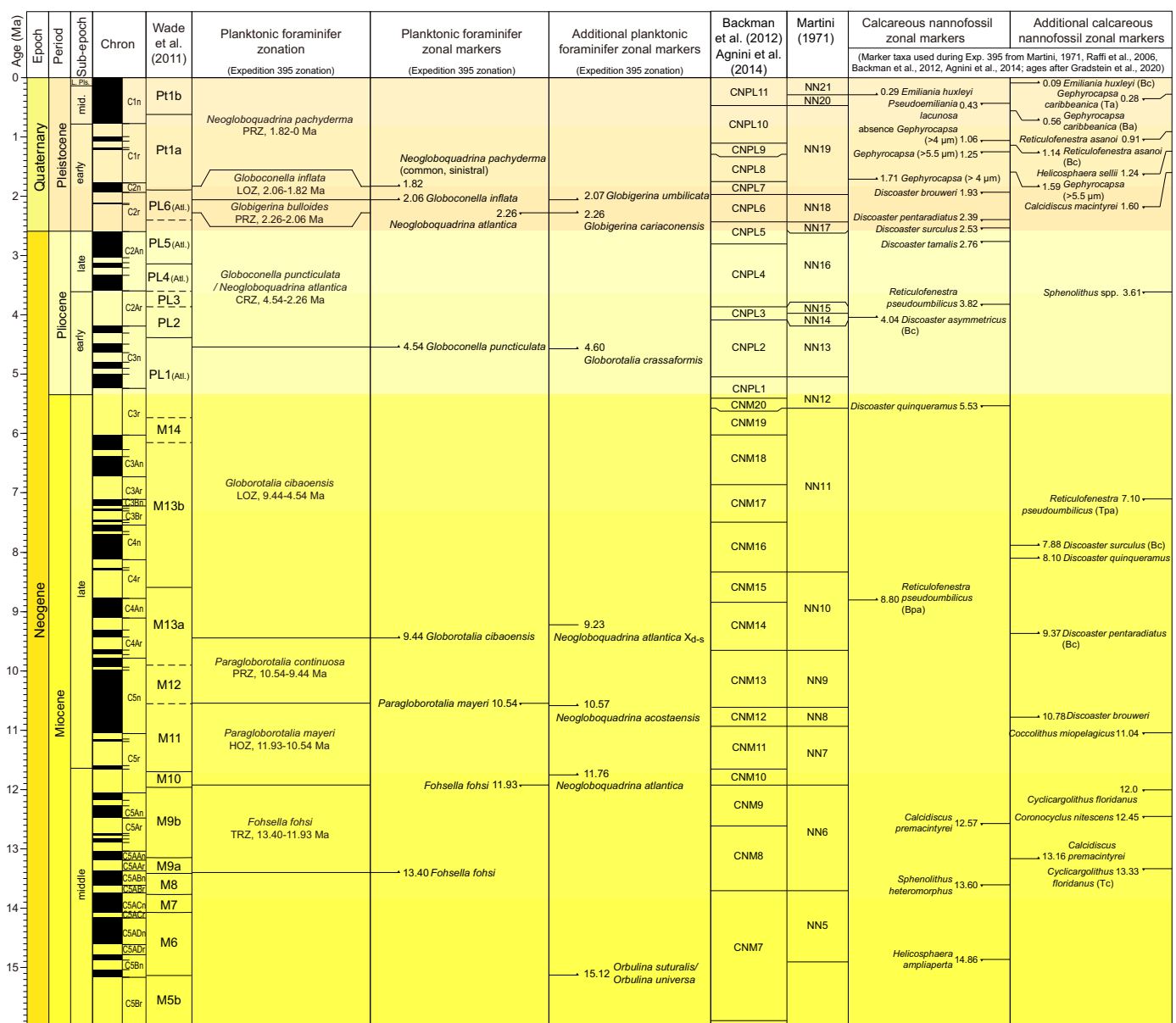


Figure F14. Biostratigraphic framework used during Expedition 395 (0–35 Ma). Bioevent calibrations for nannofossils and planktonic foraminifers are adjusted to those of *Geologic Time Scale 2020* (Gradstein et al., 2020). (Continued on next page.)

study of ODP Site 667A in the equatorial Atlantic and ODP Site 709C in the equatorial Indian Ocean. With this size definition, Bown and Dunkley Jones (2012) determined the top common occurrence of *C. abisectus* to be immediately below top *F. ciproensis* at eastern equatorial Pacific Integrated Ocean Drilling Program Site U1334, and this is the size definition we use herein. Similarly, although rare occurrences of *C. abisectus* >10 µm were recorded into the lower Miocene at ODP Site 900A on the Iberian margin, the last consistent occurrence of *C. abisectus* (>10 µm) is at the top of Zone NP25 (de Kaenel and Villa, 1996). From the same study, it is also noted that top *R. bisecta* (<10 µm) is coincident with top *F. ciproensis* with the conclusion that this event can be of use in approximating the Oligocene/Miocene boundary. In the Mediterranean, Fornaciari and Rio

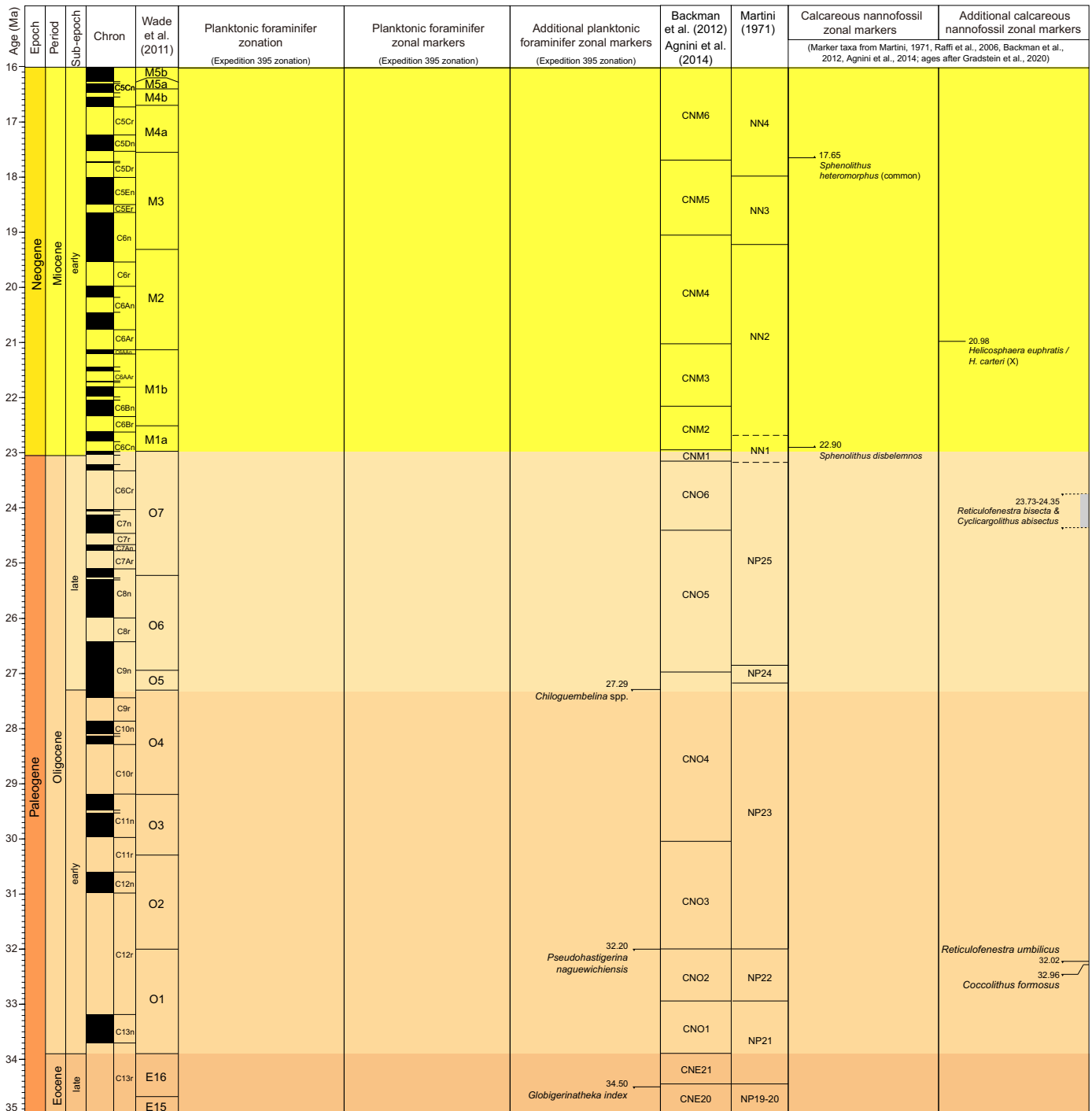


Figure F14 (continued).

(1996) find the top common occurrence of *R. bisecta* between top *F. ciproensis* and base *S. delphix*. Although some latitudinal diachrony has been suggested for top *R. bisecta* (Wei and Wise, 1989; Fornaciari et al., 1993), Berggren et al. (1995) places this event in Subchron C6Cn.2r (23.040–23.212 Ma) at high midlatitude ODP Site 703 (47°S) (based on the study of Wei [1991]), which is only slightly younger than its position in low- and midlatitude locations. In summary, although there is not a definitive calibration age for the two events in question, their consistent stratigraphic position relative to each other and between top *F. ciproensis* and base *S. delphix* gives some confidence in using the age range of the later two bioevents (23.73–24.35 Ma) as an age constraint for both top *R. bisecta* and top *C. abisectus*.

Table T3. Cenozoic calcareous nannofossil bioevents, Expedition 395. B = base, Bc = base common, Ba = base acme, Bpa = base paracme, T= top, Tc = top common, Ta = top acme, Tpa = top paracme, X = abundance crossover. [Download table in CSV format.](#)

Bioevent	Event	Age (Ma)	Zone/Subzone base		Calibration references
			Zone base (Martini, 1971; Sissingh, 1977) and Agnini et al. [2014]	(Raffi et al. [2020] after Backman et al. [2012])	
1	Bc <i>Emiliana huxleyi</i>	0.09			Raffi et al. (2020)
2	Ta <i>Gephyrocapsa caribbeanica</i>	0.28			Baumann and Freitag (2004)
3	B <i>Emiliana huxleyi</i>	0.29	NN21		Raffi et al. (2020)
4	T <i>Pseudoemiliana lacunosa</i>	0.43	NN20	CNPL11	Raffi et al. (2020)
5	Ba <i>Gephyrocapsa caribbeanica</i>	0.56			Baumann and Freitag (2004)
6	T <i>Reticulofenestra asanoi</i>	0.91			Raffi et al. (2020)
7	T absence <i>Gephyrocapsa</i> (>4 µm)	1.06		CNPL10	Raffi et al. (2020)
8	Bc <i>Reticulofenestra asanoi</i>	1.14			Raffi et al. (2020)
9	T <i>Helicosphaera sellii</i> (Atlantic)	1.24			Raffi et al. (2020)
10	T <i>Gephyrocapsa</i> (>5.5 µm)	1.25		CNPL9	Raffi et al. (2020)
11	B <i>Gephyrocapsa</i> (>5.5 µm)	1.59			Raffi et al. (2020)
12	T <i>Calcidiscus macintyreii</i>	1.60			Raffi et al. (2020)
13	B <i>Gephyrocapsa</i> (>4 µm)	1.71		CNPL8	Raffi et al. (2020)
14	T <i>Discoaster brouweri</i>	1.93	NN19	CNPL7	Raffi et al. (2020)
15	T <i>Discoaster pentaradiatus</i>	2.39	NN18	CNPL6	Raffi et al. (2020)
16	T <i>Discoaster surculus</i>	2.53	NN17		Raffi et al. (2020)
	Base Pleistocene	2.59			
17	T <i>Discoaster tamalis</i>	2.76		CNPL5	Raffi et al. (2020)
	Base upper Pliocene	3.60			
18	T <i>Sphenolithus</i> spp.	3.61			Raffi et al. (2020)
19	T <i>Reticulofenestra pseudoumbilicus</i>	3.82	NN16	CNPL4	Raffi et al. (2020)
20	Bc <i>Discoaster asymetricus</i>	4.04		CNPL3	Raffi et al. (2020)
	Base Pliocene	5.33			
21	T <i>Discoaster quinqueramus</i>	5.53	NN12	CNM20	Raffi et al. (2020)
22	Tpa <i>Reticulofenestra pseudoumbilicus</i>	7.10			Raffi et al. (2020)
23	Bc <i>Discoaster surculus</i>	7.88			Raffi et al. (2020)
24	B <i>Discoaster quinqueramus</i>	8.10			Raffi et al. (2020)
25	Bpa <i>Reticulofenestra pseudoumbilicus</i>	8.80		CNM15	Raffi et al. (2020)
26	Bc <i>Discoaster pentaradiatus</i>	9.37			Raffi et al. (2020)
27	B <i>Discoaster brouweri</i>	10.78			Raffi et al. (2020)
28	T <i>Coccolithus miopelagicus</i>	11.04			Raffi et al. (2020)
	Base upper Miocene	11.65			
29	T <i>Cyclicargolithus floridanus</i>	~12.0			Raffi et al. (2020)
30	T <i>Coronocyclus nitescens</i>	12.45			Raffi et al. (2020)
31	T <i>Calcidiscus premacintyreii</i>	12.57		CNM9	Raffi et al. (2020)
32	B <i>Calcidiscus premacintyreii</i>	13.16			Raffi et al. (2020)
33	Tc <i>Cyclicargolithus floridanus</i>	13.33			Raffi et al. (2020)
34	T <i>Sphenolithus heteromorphus</i>	13.60	NN6	CNM8	Raffi et al. (2020)
35	T <i>Helicosphaera ampliaptera</i>	14.86	NN5		Raffi et al. (2020)
	Base middle Miocene	15.99			
36	Bc <i>Sphenolithus heteromorphus</i>	17.65		CNM6	Raffi et al. (2020)
37	X <i>Helicosphaera euphratis</i> – <i>Helicosphaera carteri</i>	20.98		CNM4	Raffi et al. (2020)
38	B <i>Sphenolithus disbelemnos</i>	22.90		CNM2	Raffi et al. (2020)
	Base Miocene	23.04			
39	T <i>Reticulofenestra bisecta</i>	23.73–24.35			See Methods text
40	T <i>Cyclicargolithus abisectus</i>	23.73–24.35			See Methods text
41	T <i>Furcatolithus predistentus</i>	26.93		CNO5	Agnini et al. (2014) updated to Speijer et al. (2020)
	Base upper Oligocene	27.29			
42	T <i>Reticulofenestra umbilicus</i>	32.02	NP23	CNO3	Agnini et al. (2014) updated to Speijer et al. (2020)
43	T <i>Coccolithus formosus</i>	32.96	NP22	CNO2	Agnini et al. (2014) updated to Speijer et al. (2020)
	Base Oligocene	33.90			

The following qualitative abundance codes were used in the GEODESC data entry program and uploaded to the LIMS database.

Total calcareous nannofossil abundance in the sediment was recorded as follows:

- D = dominant (>90% of sediment particles).
- A = abundant (>50%–90% of sediment particles).
- C = common (>10%–50% of sediment particles).
- F = few (1%–10% of sediment particles).
- R = rare (<1% of sediment particles).
- B = barren (none present).

Abundance of individual calcareous nannofossil taxa is based on specimens per FOV at 1000× magnification:

- V = very abundant (>100 specimens per FOV).
- A = abundant (10–100 specimens per FOV).
- C = common (1–9 specimens per FOV).
- F = few (1 specimen per 2–10 FOV).
- R = rare (1 specimen per 11–100 FOV).
- P = present (1 specimen per >100 FOV).

Preservation of calcareous nannofossils was recorded as follows:

- VG = very good (no evidence of dissolution and/or recrystallization; no alteration of primary morphological characteristics; specimens identifiable to the species level).
- G = good (little or no evidence of dissolution and/or recrystallization; primary morphological characteristics unaltered or only slightly altered; specimens identifiable to the species level).
- M = moderate (specimens exhibit some etching and/or recrystallization; primary morphological characteristics somewhat altered; however, most specimens identifiable to the species level).
- P = poor (specimens severely etched or overgrown; primary morphological characteristics largely destroyed; fragmentation has occurred; specimens often not identifiable at the species and/or generic level).

5.2. Planktonic foraminifers

Planktonic foraminifers were examined from core catcher samples and selected samples taken from split cores. Planktonic foraminifers were also examined from mudline samples from the top of selected holes. Mudline samples were stained with rose bengal to highlight living cells. Sample volumes of 10 or 20 cm³ were washed over 63 μm sieves. Harder samples were dried at ~40°C for ~12 h before washing in a sediment shaker. Some samples were treated with hydrogen peroxide. Very hard samples were frozen for 24 h and then placed in a freeze drier to remove all moisture before washing. Empty sieves were soaked in blue dye and then cleaned in an ultrasonic bath to minimize and identify any cross contamination between samples. Dried residues (>63 μm) were transferred to labeled glass vials, from which subsamples were examined on metal trays using a binocular Zeiss Discovery V8 stereomicroscope. Because the >63 μm residues are so variable in their nonforaminifer composition, a representative area of each residue was photographed. Apart from planktonic foraminifers, the following particle categories were recorded: siliceous plankton, spicules, quartz, rock fragments, glauconite/phosphate, pyrite, and tephra. For each of these, the following abundance categories relative to total sediment particles were estimated from visual examination of the dried sample in the >63 μm fraction as follows:

- D = dominant (>30% of sediment particles).
- A = abundant (10%–30% of sediment particles).
- F = few (5% to <10% of sediment particles).
- R = rare (1% to <5% of sediment particles).
- P = present (<1% of sediment particles).
- B = barren.

Planktonic foraminifer preservation as viewed under the light microscope was recorded as follows and is based on the Expedition 363 methods chapter (Rosenthal et al., 2018):

- E = excellent (most specimens have a glassy appearance, indicating very little recrystallization and very little evidence of overgrowth or dissolution, and little abrasion).
- VG = very good (some show minor evidence of diagenetic overgrowth, dissolution, or abrasion; recrystallization may or may not have occurred).
- G = good (some specimens show signs of significant overgrowth, dissolution, or abrasion and may show some infilling with cement or indurated sediment).
- M = moderate (most specimens show evidence of overgrowth, dissolution, and abrasion; tests generally infilled with cement or indurated sediment obscuring apertures).
- P = poor (substantial diagenetic overgrowth, dissolution, and abrasion; foraminifers can be fragmentary and difficult to identify because of major overgrowth and/or dissolution).

Most work focused on the sieved >150 μm size fraction for biostratigraphic purposes, but the 63–150 μm fraction was also examined for marker species, to assess fragmentation, and to scan for the smaller species. Selected specimens were imaged using a QImaging Image Capture system.

Abundances of planktonic foraminifer species in the >150 μm size fraction were estimated using the following scheme:

- D = dominant (>50% of the planktonic foraminifer assemblage).
- A = abundant (>20%–50% of the planktonic foraminifer assemblage).
- C = common (>10%–20% of the planktonic foraminifer assemblage).
- F = few (>5%–10% of the planktonic foraminifer assemblage).
- R = rare (1%–5% of the planktonic foraminifer assemblage).
- P = present (<1% of the planktonic foraminifer assemblage).

Abundances were not estimated for the 63–150 μm size fraction, for which species were simply recorded as present (P), even if they are numerically dominant.

Previous drilling in Pliocene to recent sediments of the high-latitude North Atlantic demonstrates that few of the standard planktonic foraminifer marker species used in the standard global tropical and subtropical biozonation are likely to be present at $\sim 60^\circ\text{N}$, or if present they may occur only very rarely as occasional immigrants. Even in the warmer Miocene epoch, when latitudinal differences in assemblages are less marked, many tropical species are likely to be absent. As a result, there have been repeated efforts to develop regionally applicable biostratigraphic schemes for the North Atlantic based on endemic cold-water tolerant taxa (Poore and Berggren, 1975; Poore, 1979; Weaver and Clement, 1986; Spiegler and Jansen, 1989; Flower, 1999; Anthonissen, 2009; Sierro et al., 2009). We have reviewed these previous biostratigraphic schemes in light of a substantial body of work published on Mediterranean planktonic foraminifer biostratigraphy (e.g., Rio et al., 1984; Iaccarino, 1985; Lourens et al., 1996; Pasini and Colalongo, 2004; Hilgen et al., 2005; Lirer et al., 2019) and abstracted a list of 12 primary biohorizons covering the last 12 My. These biohorizons were numbered and, where necessary, recalibrated to the GPTS of Ogg (2020) with additions from Kochhann et al. (2016) as used herein, taking into account the errors produced by the sampling resolution of the biostratigraphy and paleomagnetism of the original published data. This biohorizon list was used to derive the Expedition 395 planktonic foraminifer biozonation, which is based principally on previous high-latitude biozonations of Poore and Berggren (1975) and Weaver (1987) with elements of the standard (sub)tropical biozonation of Wade et al. (2011) as updated by Raffi et al. (2020) combined with two new suggested zones (the *Globorotalia cibaoensis* and *Paragloborotalia continuosa* Zones) inserted to make a coherent scheme that is locally applicable. The list of datums is provided in Table T4. A detailed discussion of individual calibrations is reserved for a dedicated study. The list of biozone definitions is as follows (note that we use the terms bottom and top for the endpoints of stratigraphic ranges, rather than lowest occurrence, highest occurrence, first appearance datum, or last appearance datum):

- *Neogloboquadrina pachyderma* Partial Range Zone (PRZ), 1.82 Ma–recent.
 - Definition: partial range of the nominate taxon between the bottom common occurrence of sinistral encrusted *N. pachyderma* and the recent (Weaver and Clement, 1986, modified).
- *Globoconella inflata* Lowest Occurrence Zone (LOZ), 2.06–1.82 Ma.
 - Definition: biostratigraphic interval from the bottom occurrence of *G. inflata* to the bottom common occurrence of sinistral encrusted *N. pachyderma* (Weaver and Clement, 1986, modified).
- *Globigerina bulloides* PRZ, 2.26–2.06 Ma.
 - Definition: partial range of the nominate taxon between the top occurrence of *Neogloboquadrina atlantica* and the bottom occurrence of *G. inflata* (Weaver and Clement, 1986).
- *Globoconella puncticulata*/*N. atlantica* Concurrent Range Zone (CRZ), 4.54–2.26 Ma.
 - Definition: biostratigraphic interval between the bottom occurrence of *G. puncticulata* and the top occurrence of *N. atlantica* (Weaver and Clement, 1986, modified).
- *Globorotalia cibaoensis* LOZ, 9.44–4.54 Ma.
 - Definition: biostratigraphic interval between the bottom occurrence of *G. cibaoensis* and the bottom occurrence of *G. puncticulata* (this study).
- *Paragloborotalia continuosa* PRZ, 10.54–9.44 Ma.
 - Definition: partial range of the nominate taxon between the top occurrence of *Paragloborotalia mayeri* and the bottom occurrence of *G. cibaoensis* (this study).
- *Paragloborotalia mayeri* Highest Occurrence Zone (HOZ), 11.93–10.54 Ma.
 - Definition: biostratigraphic interval between the top occurrence of *Fohsella fohsi* and the top occurrence of *P. mayeri* (Poore and Berggren, 1975, modified).
- *Fohsella fohsi* Taxon Range Zone (TRZ), 13.40–11.93 Ma.
 - Definition: Total range of the nominate taxon (Wade et al., 2011).

Table T4. Calibration ages of North Atlantic planktonic foraminifer (F) and bolboform (B) bioevents from the upper Miocene to recent, Expedition 395. B = bottom, Bc = Base common, T = top, X = coiling reversal, d-s = dextral to sinistral. [Download table in CSV format.](#)

Biohorizon	Marker species	GTS2020 age (Ma)	Calibration	(Sub)zone base
F1	Bc <i>Neogloboquadrina pachyderma</i> (sin)	1.82	This study, based on Flower (1999), ODP Site 982	<i>N. pachyderma</i> PRZ
F2	B <i>Globoconella inflata</i>	2.06	This study, based on Flower (1999), ODP Site 982	<i>G. inflata</i> LOZ
F3	B <i>Globigerina umbilicata</i>	~2.07	This study, based on Rio et al. (1984), Mediterranean	
F4	T <i>Neogloboquadrina atlantica</i>	2.26	This study, based on Flower (1999), ODP Site 982	<i>G. bulloides</i> PRZ
F5	B <i>Globigerina cariacensis</i>	~2.26	This study, based on Poore and Berggren (1975), DSDP Site 116	
	Base Pleistocene	2.59		
	Base upper Pliocene	3.60		
F6	B <i>Globoconella puncticulata</i>	4.54	This study, based on Weaver and Clement (1987), DSDP Site 609	<i>G. puncticulata</i> / <i>N. atlantica</i> CRZ
F7	B <i>Globorotalia crassaformis</i>	~4.60	This study, based on Weaver (1987), DSDP Site 606	
	Base Pliocene	5.33		
F8	X d-s <i>Neogloboquadrina atlantica</i>	9.23	This study, based on Aksu and Kaminski (1989) and Shipboard Scientific Party (1987), DSDP Site 646	
F9	B <i>Globorotalia cibaoensis</i>	9.44	Raffi et al. (2020), based on Chaisson and Leckie (1993), ODP Site 806	<i>G. cibaoensis</i> LOZ
F10	T <i>Paragloborotalia mayeri</i>	10.54	Raffi et al. (2020), based on Chaisson and Pearson (1997), ODP Site 925	<i>P. continuosa</i> PRZ
F11	B <i>Neogloboquadrina acostaensis</i>	10.57	Raffi et al. (2020), based on Lourens et al. (2004), Mediterranean sites	
	Base upper Miocene	11.65		
F12	B <i>Neogloboquadrina atlantica</i>	11.76	This study, based on <i>Neogloboquadrina</i> group of Hilgen et al. (2003), Monte dei Corvi, Italy	
F13	T <i>Fohsella fohsi</i>	11.93	Raffi et al. (2020) based on Pearson and Chaisson (1997), ODP Site 925	<i>P. mayeri</i> HOZ
F14	B <i>Fohsella fohsi</i>	13.40	Raffi et al. (2020) based on Pearson and Chaisson (1997), ODP Site 925	<i>F. fohsi</i> TRZ
F15	B <i>Orbulina universa</i> / <i>O. suturalis</i>	15.12	Raffi et al. (2020)	
	Base middle Miocene	15.99		
	Base Miocene	23.04		
F16	Tc <i>Chiloguembelina</i> spp.	27.29	Wade et al. (2011) updated to Speijer et al. (2020)	
	Base upper Oligocene	27.29		
F17	T <i>Pseudohastigerina nagewichiensis</i>	32.20	Wade et al. (2011) updated to Speijer et al. (2020)	
	Base Oligocene	33.90		
F18	T <i>Globigerinatheka index</i>	34.50	Wade et al. (2011) updated to Speijer et al. (2020)	
	Base Pliocene	5.33		
B1	T <i>Bolboforma intermedia</i>	5.85	This study, based on Spiegler (1999) and Drury et al. (2018)	<i>B. costairregularis</i> HOZ
B2	T <i>Bolboforma metzmacheri</i>	8.15	This study, based on Spiegler (1999) and Drury et al. (2018)	
B3	B <i>Bolboforma intermedia</i>	8.18	This study, based on Spiegler (1999) and Drury et al. (2018)	<i>B. intermedia</i> TRZ
B4	B <i>Bolboforma metzmacheri</i>	9.89	This study, based on Spiegler (1999) and Drury et al. (2018)	<i>B. metzmacheri</i> LOZ
B5	T <i>Bolboforma subfragoris</i>	10.82	This study, based on Spiegler (1999) and Drury et al. (2018)	<i>B. capsula</i> PRZ
	Base upper Miocene	11.65		

5.3. Bolboforms

Bolboforms (members of genus *Bolboforma*) are an extinct group of small (generally <150 μm) mostly single-chambered microfossils, possibly produced by Chrysophyte algae (Spiegler and Spezzaferri, 2005). They occur in temperate to high-latitude sediments of both hemispheres and range in age from early Eocene to late Pliocene. Despite a somewhat patchy stratigraphic and geographic distribution, they provide a useful supplement to the biostratigraphy of the other main calcareous microfossil groups. They were studied in the samples taken for foraminifers using the same scales for preservation and relative abundance described in [Planktonic foraminifers](#).

Bolboforms have been used to provide biostratigraphic age control at a number of sites across the North Atlantic, the most detailed record being that of Spiegler (1999) from ODP Site 982 in the Hatton-Rockall Basin. We used the record of Spiegler (1999) in combination with the updated interhole splice and astronomical age model for Site 982 of Drury et al. (2018) to calibrate a series of biohorizons to the expedition timescale (Table T4). The following bolboform biozonation is based on that of Spiegler (1999) adjusted to eliminate ambiguous “and/or” criteria in the biozone definitions:

- *Bolboforma costairregularis* HOZ, 5.85 Ma–? upper Pliocene, uncalibrated.
 - Definition: biostratigraphic interval between the top occurrence of *Bolboforma intermedia* and the top occurrence of *B. costairregularis* (Spiegler, 1999, modified).
- *Bolboforma intermedia* TRZ, 8.18–5.85 Ma.
 - Definition: total range of *B. intermedia* (Spiegler, 1999).
- *Bolboforma metzmacheri* LOZ, 9.89–8.18 Ma.
 - Definition: biostratigraphic interval between the lowest occurrence of *B. metzmacheri* and the lowest occurrence of *B. intermedia* (Spiegler, 1999, modified).
- *Bolboforma capsula* PRZ, 10.82–9.89 Ma.
 - Definition: biostratigraphic interval between the top occurrence of *Bolboforma subfragoris* and the lowest occurrence of *B. metzmacheri* (Spiegler, 1999, modified).
- *Bolboforma subfragoris* TRZ, ? upper Miocene, uncalibrated–10.82 Ma.
 - Definition: total range of *B. subfragoris* (Spiegler, 1999).

6. Physical properties

Physical properties measurements are acquired to characterize the physical, chemical, and structural properties of the recovered sediment and basalt cores. The acquired data sets are also used for correlation between holes from the same sites, as well as with downhole logging data. Physical properties data sets include track scan measurements on whole-round sections (GRA bulk density, MS, *P*-wave logger [PWL], NGR, and X-ray imaging) and on section halves (MSP, color spectrometry [RGB], reflectance spectroscopy and colorimetry [RSC], and X-ray imaging). Discrete MAD, thermal conductivity, and V_p caliper (PWC) measurements are made on specific sediment core samples (Table T5). The data cleaning process is detailed in the description of each measurement type and in [Note on data cleaning](#).

6.1. Laboratory workflow

After initial curation, whole rounds from sedimentary depth intervals were first measured on the STMSL to provide MS and formation density data for stratigraphic correlation. During Expedition 395, measurements of O_2 concentration and temperature were performed on selected whole rounds after STMSL scanning. Cores were then left to equilibrate to room temperature (~ 4 h), during which X-ray images of the whole rounds were acquired on the XSCAN. Once the temperature was equilibrated, the core was measured on the WRMSL, which measures GRA bulk density, V_p , and MS, and then on the NGRL. Whole-round thermal conductivity measurements were typically made on core Section 4 after WRMSL scanning was complete; in deeper cores where sediment compaction made using whole-round cores impractical, thermal conductivity was measured on split core surfaces instead. Following completion of whole-round measurements, the core was split and moved to the SHIL and SHMSL, which measure RGB, MSP, and RSC. Subsequently, dis-

crete V_p measurements were collected on section halves on the Section Half Measurement Gantry (SHMG). MAD was measured on samples collected from working halves.

For basalt core intervals, whole-round core was first cleaned and examined by the petrology team, and sections were prepared by the technicians and imaged in several orientations on the SHIL to construct a 360° view of the samples. Following imaging on the SHIL, the cores were placed back in the core liner before passing through a series of whole-round measurements on the WRMSL (GRA bulk density and MS) and the NGRL (NGR). The section halves were imaged using the XSCAN. Once the data were collected from the WRMSL and NGRL, thermal conductivity was measured on a piece of the split core. Discrete V_p values and MAD were measured using the SHMG and pycnometer, respectively, on the cut sample cubes after magnetic measurements were made (See [Paleomagnetism](#)).

6.2. Multisensor core loggers

Expedition 384, 395C, and 395 STMSL measurements (MS and GRA bulk density) on the recovered sediments were made at 5 cm resolution (fast-track mode) to facilitate rapid stratigraphic correlation. Hard rock cores (lithified sediments and basement material) are sometimes recovered as disaggregated pieces rather than as continuous core, reducing the rock volume in the core liner. Therefore, GRA bulk density and MS measurements on these rock types may be underestimated but can still provide useful information for later stratigraphic correlation and can eventually be compared to discrete MAD and MSP measurements. QA/QC was monitored and maintained by running a core liner with freshwater through the STMSL after each full core length was measured.

Table T5. Measurement resolution, Expeditions 384, 395C, and 395. MSPOINT = MSP, PWB = *P*-wave bayonet, TCON = thermal conductivity. * = some variability in the measurement resolution that is dependent on the core recovery and changes in lithology. — = corresponding property was not measured. [Download table in CSV format.](#)

Exp	Site	Hole	Type	GRA (cm)	MAD (m)	MS (cm)	MSPOINT (cm)	NGR (cm)	RGB (cm)	RSC (cm)	PWL (cm)	PWC (m)	PWB (m)	TCON (m)
384	U1554	A	Sediment	5.0	~10	2.5	2.5	10	1	2.5	2.5	—	—	—
384	U1554	B	Sediment	2.5	~10	1.5	2.5	10	1	2.5	2.5	—	—	—
384	U1554	C	Sediment	2.5	—	2.5	2.5	10	1	2.5	2.5	—	—	—
395C	U1554	E	Sediment	2.5	~10	2.5	2.0	10	1	2.0	2.5	—	—	—
395C	U1554	F	Basalt	2.5	—	2.5	2.0	10	1	2.0	—	—	—	—
395	U1554	G	Sediment	2.5	~5	2.5	2.5	10	1	2.0	2.5	~10	~10	—
395	U1554	H	Sediment	2.5	—	2.5	2.5	10 or 20	1	2.0	2.5	~10	—	~10
384	U1555	F	Sediment	2.5	—	2.5	2.5	10	1	2.5	2.5	—	—	—
384	U1555	F	Basalt	2.5	—	2.5	2.5	10	1	2.5	—	—	—	—
384	U1555	G	Basalt	2.5	—	2.5	2.5	10	1	2.5	—	—	—	—
395C	U1555	H	Sediment	2.5	~10	2.5	2.0	10	1	2.0	2.5	—	—	~10
395C	U1555	I	Sediment	2.5	2 samples	2.5	2.0	10	1	2.0	~10*	—	—	~10*
395C	U1555	I	Basalt	2.5	—	2.5	2.0	10	1	2.0	—	~10	—	~10*
395C	U1562	A	Sediment	2.5	~10	2.5	2.5	10	1	2.5	2.5	—	—	~10
395C	U1562	A	Basalt	2.5	—	2.5	2.5	10	1	2.5	—	1 sample	—	1 sample
395C	U1562	B	Sediment	2.5	—	2.5	2.0	10	1	2.0	2.5	~1 per core	—	—
395C	U1562	B	Basalt	2.5	—	2.5	2.0	10	1	2.0	2.5	~1 per core	—	~10*
395	U1562	C	Sediment	2.5	—	2.5	2.5	10	1	2.5	2.5	~1 per core	—	~5–10
395C	U1563	A	Sediment	2.5	~10	2.5	2.5	10	1	2.5	2.5	—	—	~10
395C	U1563	A	Basalt	2.5	—	2.5	2.5	10	1	2.5	—	—	—	—
395C	U1563	B	Basalt	2.5	—	2.5	2.0	10	1	2.0	—	~10	—	~10
395C	U1564	A,B,C	Sediment	2.5	—	2.5	2.5	20	1	2.5	2.5	—	—	—
395	U1564	D	Sediment	2.5	~5	2.5	2.5	10	1	2.5	2.5	~10	~10	~10
395	U1564	E	Sediment	2.5	~5	2.5	2.5	10	1	2.5	2.5	~10	—	~10
395	U1564	F	Sediment	2.5	~5	2.5	2.5	10	1	2.5	—	~10	—	~10
395	U1564	F	Basalt	2.5	~10	2.5	2.5	10	1	2.5	—	~5	—	~5
395	U1602	A	Sediment	2.5	—	2.5	2.5	10	1	2.5	2.5	—	—	—
395	U1602	B	Sediment	2.5	~5	2.5	2.5	10	1	2.5	2.5	~10	~10	~10
395	U1602	C	Sediment	2.5	~5	2.5	2.5	10	1	2.5	2.5	2 samples	—	—
395	U1602	D	Sediment	2.5	~5	2.5	2.5	10 or 20	1	2.5	2.5	~10*	—	~10*
395	U1602	E	Sediment	2.5	~2–10	2.5	2.5	10	1	2.5	2.5	~10*	—	~10

Expedition 385, 395C, and 395 WRMSL measurement (MS, GRA bulk density, and PWL) resolution was 2.5 cm for both sediment and basalt cores. QA/QC was monitored and maintained by running a core liner with freshwater through the WRMSL after each full core length was measured. WRMSL measurements are most accurate on a liner completely filled with core that experienced minimal drilling disturbance. A core liner diameter of 66 mm is assumed for hard rock density (GRA bulk density) calculations, despite the fact that the liner is often filled less than 100%, usually resulting in underestimated values. WRMSL PWL measurements are susceptible to error depending on the quality of the coupling of the sensors with the core through the liner. When air or fluid is present around the rock in the liner, PWL measurements are of lower confidence. This issue is more common when the core is biscuited during cutting with the XCB system or when using a RCB bit (e.g., lithified sediments and basalt core). Accordingly, WRMSL PWL was used only for the sediment intervals.

6.2.1. Gamma ray attenuation

The GRA densitometer on the WRMSL operates by passing gamma rays from a ^{137}Cs source down through a whole-round core section into a 75 mm × 75 mm sodium iodide detector located directly below the core. Gamma rays with an energy peak at 662 keV are attenuated by Compton scattering as they pass through the core (Evans, 1965; Harms and Choquette, 1965). The resultant gamma ray count is proportional to bulk density and shows clear variations with sediment composition and compaction and within the basalts. Calibration of the GRA densitometer is performed using core liners filled with seawater and aluminum density standards. Recalibration is performed as needed if the value of the freshwater QA/QC standard run, which is run as a pusher after every full core, deviates significantly (more than ~2%) from 1 g/cm³. The spatial resolution of the GRA densitometer is <1 cm.

GRA bulk density data were cleaned by removing values that coincide with foam pieces and physically improbable data such as values below water density (1 g/cm³). These spurious values were changed to NaN to designate not a number, and the cleaned data were used to generate the plots used in the Physical properties and Lithostratigraphy sections in the site chapters (see PHYSPROP in [Supplementary material](#)). Further evaluation of the measurements can be made by comparing the GRA bulk density and MAD measurements against density wireline logs.

6.2.2. Magnetic susceptibility

MS (k) is a dimensionless measure of the degree to which a material can be magnetized by an external magnetic field, given by

$$k = \frac{M}{H},$$

where M is the magnetization induced in the material by an external field strength H . MS responds to variations in the type and concentration of magnetic grains, making it useful for identifying compositional variations and alteration in sediment and hard rock core. In the case of sediments, MS can often be related to mineralogical composition (e.g., siliciclastic versus carbonate material). Water and plastics (e.g., core liner) have a slightly negative MS. Both the STMSL and WRMSL incorporate a Bartington Instruments MS2 meter coupled to an MS2C sensor coil with a diameter of 8.8 cm that operates at a frequency of 565 Hz (Bartington Instruments, 2011).

STMSL and WRMSL MS measurements are reported in instrument units (IU) because the core mass is not measured prior to data acquisition and the internal volume cannot be determined until the core is split. The correction for the volume does not change the order of magnitude of the measured susceptibility values, so the results are comparable with the susceptibility measured using the paleomagnetism equipment, which also reports data using instrument units.

The MS2C coil was calibrated with a homogeneous mixture of magnetite and epoxy in a 40 cm long piece of core liner to an accuracy of ±5%. The loop sensor averages across an interval of ~8 cm of a section, creating a smoothed data set for a continuous core section. A result of this smoothing is that MS is underestimated in sections that do not contain continuous core over a given 8 cm interval. MS data were cleaned post acquisition by removing unrealistic values ≤0 and data acquired on foam pieces and core gaps. Such erroneous data were set to NaN in the cleaned

data set. The cleaned data are presented in the figures here; however, note that the LIMS database contains the uncleaned record.

6.2.3. P-wave velocity

The V_p of whole-round sediment core was measured with the PWL, which is incorporated into the WRMSL. The PWL uses a 500 kHz compressional wave pulse transmitted across the core liner (orthogonal to depth) between two transducer-coupled calipers. Coupling between the calipers and the core liner is aided by water continuously dripping across the caliper surfaces. The pulse waveform is bandpass filtered between 0.4 and 1.0 MHz, stacked, summed, and ensemble-averaged to allow for automatic first arrival picking by the integrated WRMSL software. The PWL measurements were automatically corrected for the effects of the acrylic liner and calibrated using known velocities of a freshwater-filled liner and aluminum standards. XCB and RCB coring often yield core that does not fill the core liner, leading to air-filled voids, so WRMSL PWL measurements made on sediment cores collected using the XCB system should be treated with caution, and WRMSL PWL data were not measured on core recovered with the RCB system. WRMSL PWL data were cleaned by removing unrealistic V_p measurements below that of water (1490 m/s), as well as measurements made on foam pieces and core gaps. Where erroneous data were removed, they were replaced in the cleaned data set by the value NaN as presented in the figures; the LIMS database contains the full, uncleaned record.

6.2.4. Natural Gamma Radiation Logger

NGR occurs primarily as the result of the decay of ^{238}U , ^{232}Th , and ^{40}K . The NGRL detector unit was calibrated using ^{137}Cs and ^{60}Co sources and identifying their peaks at 662 and 1330 keV, respectively. A single NGRL run consists of two sets of measurements by eight sensors, spaced 20 cm apart. The two sets of measurements are offset by 10 cm, which yields a total of 16 measurements equally spaced 10 cm apart over a 150 cm long section of core. In some instances, for operational reasons when time was limited, the core sections were only measured at one position (20 cm) in the NGRL for faster processing. For Expeditions 384, 395C, and 395, each measurement was acquired using 300 s of count, resulting in a measurement time of 600 s per core for most cores. The quality of the energy spectrum measured from a core depends on the concentration of radionuclides in the sample and on the counting time, with higher times yielding more clearly defined spectra. Sections less than 50 cm in length were not typically measured with the NGRL because of the constraints imposed by the sensor geometry.

6.2.5. X-Ray Linescan Logger

The XSCAN was installed aboard *JOIDES Resolution* in 2023 and was used during Expedition 395 but not during Expeditions 384 or 395C.

The XSCAN collects linescan X-radiographs from whole-round and split cores. The XSCAN source and detector can be rotated around the core material to produce linescans with different view angles to create pseudo-CT core scans. The XSCAN is comprised of an X-ray scanner with a 210 W, 160 kV, 1.3 mA constant potential X-ray source and linescan detector. The source is a Spellman XRBD 160PN210 Monoblock X-ray generator with a 0.5 mm focal spot. The beam angle is $90^\circ \times 12^\circ$ and is located ~ 36 cm from the source. The detector is a Hamamatsu C12300-321, composed of a charge-coupled device sensor with a ~ 22 cm FOV using time-delayed integration and a resolution of 48 μm per pixel. Imaging acquisition and processing were completed in the IMS system (Version 14). Processing of images from Expedition 395 consisted of black and white correction and image cropping. XSCAN images can facilitate the imaging of geologic structures and objects such as fractures, ice-rafted debris, and materials with distinct densities (e.g., alteration zones and oxide and sulfide concentrations). Sediment cores were measured using energies between 90–100 kV and 0.80–0.90 mA, and basalt cores were measured using energies between 100–110 kV and 0.90 mA. Additional processing was applied to images of the basalt sections by modifying smoothing functions on the image histograms so that features such as veins, fractures, and altered zones are more apparent.

6.3. Section Half Multisensor Logger

Following core splitting, photography, and description, archive-half sections were passed through the SHMSL. The SHMSL nondestructively collects MSP, RGB, and RSC data. Measurements were made every 1.0, 2.0, or 2.5 cm for both sediment and basalt, as detailed in the site chapters (Table T5). SHMSL measurements are most accurate on cores that completely fill the liner and have a flat split surface with minimal drilling disturbance.

6.3.1. Point magnetic susceptibility

MSP was measured using a Bartington Instruments MS2E point sensor. A flush contact between the probe and the archive halves and protection of the probe and core is facilitated by covering sediment section halves with low-density polyethylene wrap. The instrument collects and averages three measurements made at 1 s intervals to an accuracy of 5%. Before each measurement, the probe is zeroed in air and a background magnetic field is measured and removed from the data. A built-in laser surface analyzer aids in the recognition of irregularities in the split core surface (e.g., cracks and voids) and provides an independent check on the fidelity of SHMSL measurements, which is especially crucial in the basalt sections. Differences may arise between the SHMSL and WRMSL MS data from differences in their frequency (Dearing et al., 1996), as well as the averaging point data compared to continuous loop sensor measurements, which averages across ~8 cm of core. Because it is difficult to isolate these factors, absolute differences between the two MS systems are expected. MSP data were cleaned by removing unrealistic values ≤ 0 and removing measurements made on foam pieces and over core gaps, which were replaced by the value NaN. The cleaned data are presented in the figures; the LIMS database contains the full uncleaned record.

6.3.2. Digital imaging: color reflectance and colorimetry

The reflectance of visible light from the archive halves of sediment and basalt cores was measured using an Ocean Optics USB4000 spectrophotometer mounted on the automated SHMSL. Measurements were taken at 1.0–2.5 cm spacing (resolution is specified in the site chapters; Table T5) to provide a high-resolution stratigraphic record of color variation for visible wavelengths. Empty intervals, voids, and cracks were skipped to avoid spurious measurements. Intervals where the tops of flat hard rock surfaces were below the level of the core liner were raised by adding support matting or foam beneath each hard rock piece to ensure good contact with the sensor. Each measurement was recorded in 2 nm wide spectral bands from 400 to 700 nm. The colorimetry and reflectance data are reported using the $L^*a^*b^*$ color system, in which L^* is lightness, a^* is redness (positive) versus greenness (negative), and b^* is yellowness (positive) versus blueness (negative). The color reflectance spectrometer calibrates on two spectra, pure white (reference) and pure black (dark). Color calibration was conducted approximately once every 6 h. Data cleaning of these data sets consisted of removing unrealistic values, especially from intervals measured over foam pieces and core gaps. The cleaned color reflectance data are presented in the figures here; the LIMS database contains the full uncleaned record.

6.4. Discrete measurements

6.4.1. Moisture and density

Discrete (~ 10 cm³) sediment sample cubes were taken from the working halves of sediment cores for MAD measurements. In indurated sediment and basalt, discrete cubes were extracted for MAD analyses, which can also be used for discrete PWC measurements and paleomagnetism where desired. MAD samples were used to measure the wet and dry bulk density, grain density, water content, and porosity following methods presented in Blum (1997), which are briefly outlined below.

Prewighed and numbered 16 mL Wheaton glass vials were used to process and store the sediment samples. Following measurement of wet mass, samples were dried in a convection oven for 24 h at $105^\circ \pm 5^\circ\text{C}$. Dried samples were then cooled in a desiccator for at least 2 h before the dry mass and volume were measured. Wet and dry sample masses were measured to a precision of 0.005 g using a dual Mettler Toledo (XS204) electronic balances apparatus, with one balance act-

ing as a reference. A standard with a comparable mass to the sample was placed on the reference balance, and the computer averaging system compensated for the ship's motion by taking multiple measurements, typically 300 per sample.

Dry sample volumes were determined using the hexapycnometer system of a six-celled custom-configured Micrometrics AccuPyc 1330TC helium-displacement pycnometer. The system measures dry sample volume using pressurized He-filled chambers, where the precision of each cell is 1% of the full-scale volume. Volume measurements are preceded by three purges of the sample chamber with helium. For each measurement, five cells containing unknowns and one cell containing two stainless steel calibration spheres with a total volume of $\sim 10 \text{ cm}^3$ were run. Calibration spheres were sequentially cycled through the cells to identify any systematic error and/or instrument drift. The volumes occupied by the numbered Wheaton vials were calculated before the expedition by multiplying each vial's weight against the average density of the vial glass. The fundamental relation and assumptions for the calculations of all physical properties parameters such as wet bulk density (ρ_{wet}), dry bulk density (ρ_{dry}), sample grain density (ρ_{solid}), porosity (ϕ), and void ratio (VR) were included in the MADMax shipboard program set with the Method C calculation process (Blum, 1997).

Because of time and staff constraints, MAD was not measured on core collected during Expedition 384. During Expedition 395C, one MAD sample was processed per recovered sediment core. During Expedition 395, MAD sample selection did not duplicate depths across the holes drilled during Expedition 395C.

6.4.2. Discrete *P*-wave velocity

Discrete triaxial V_p was measured using the SHMG on working halves with a typical frequency of one measurement per 10 m of core. PWC was measured using Panametrics-NDT Microscan delay line transducers transmitting at 0.5 MHz. The signal received through the section half or discrete sample was recorded by the Velocity Gantry 2.0.5.0 IODP software, where the peak of the first *P*-wave arrival was either automatically or manually chosen. In case of a weak signal, manual picking of the first arrival was performed. The distance between transducers was measured with a built-in linear voltage displacement transformer (LDVT). Calibration was performed daily with a series of acrylic cylinders of differing thicknesses and a known V_p of $2750 \pm 20 \text{ m/s}$. The system time delay determined from calibration was subtracted from the picked arrival time to give a traveltime of the *P*-wave through the sample. The thickness of the sample (calculated using the LDVT, in meters) was divided by the traveltime (in seconds) to calculate V_p in meters per second. A clean first *P*-wave arrival can be difficult to pick depending on the material; therefore, distilled water was applied to the contacts between section half or sample cube and calipers to improve the reading. PWC measurements were acquired on average once per 5 m of core. For the basalts, PWC was measured on the cut cubes in all orthogonal directions to determine any velocity dependent anisotropy.

6.5. Thermal conductivity

Thermal conductivity is the coefficient of proportionality relating conductive heat flow to a thermal gradient (Blum, 1997). Thermal conductivity was measured aboard *JOIDES Resolution* during Expeditions 395C and 395 using the transient needle probe method in whole- or half-space geometry (Von Herzen and Maxwell, 1959) on a Teka Bolin TK04 system. Thermal conductivity measurements made with the needle probe were typically taken on the third or fourth section of each sediment core after whole-round sections had equilibrated to room temperature and prior to core splitting. The needle probe method was used in full-space configuration for soft sediments (Von Herzen and Maxwell, 1959). The needle probe was inserted into the unconsolidated sediment through 2 mm diameter holes drilled into the core liner roughly once per core. To measure a representative undisturbed interval, WRMSL MS data were used to determine appropriate locations because MS is generally lower in carbonate-rich intervals and higher in clay-rich intervals. Both were targeted to assess the thermal conductivity of these end-member lithologies. During Expedition 395, the needle probe did not yield reliable data, so the decision was made to change to the half puck probe early on. The half puck probe was placed on the working-half section and secured with a Velcro strap to ensure good contact between the core and the probe during measuring.

Table T6. Edge effect cleaning, Expedition 395. Resolution denotes edges that were cleaned from the tops and ends of every section to account for soupy behavior and instrument response function. [Download table in CSV format.](#)

Physical properties data	Edge effect cleaning resolution (cm)
MS (WRMSL)	10
MS (SHMSL)	10
GRA (WRMSL)	10
<i>P</i> -wave logger	10
NGR	10
PWC	NA
PWL	NA
PWB	NA
MAD	NA
RGB (SHMSL)	5
Colorimetry (SHMSL)	5

For hard rock, thermal conductivity measurements were made on split core pieces ≥ 10 cm long. The split samples were first saturated in ambient temperature seawater for 4 h with a vacuum pump to aid in the full saturation of pore space. A puck with the measurement probe attached was placed on the split face of the core piece and secured with a rubber band. Three steps of heating and cooling were completed to make the thermal conductivity measurement, and the mean of these three values was used as the final thermal conductivity value.

Combining core thermal conductivity measurements of the sediments with downhole formation temperatures collected using the APCT-3 tool enabled calculation of an approximated heat flow. First, depth (using the CSF-A scale) was divided by the thermal conductivity estimate ($W/[m \cdot K]$) to yield thermal resistance (m^2K/W). A linear trendline was fit to the thermal resistance against temperature plot to estimate thermal resistance for depths where the formation temperature measurements were acquired. The heat flow (W/m^2) was estimated as the slope of the thermal resistance against temperature (in K).

6.6. Note on data cleaning

Physical properties figures presented in each site chapter were cleaned to account for section edge effect (Table T6). In addition, the observations presented for the downcore figures for each whole round were also subjected to a secondary filtering process to remove anomalous and unreasonable values; these corrections were specific to sites and can be found in the respective site chapters. The cleaned data sets are available in PHYSPROP in [Supplementary material](#).

7. Stratigraphic correlation

Many of the Expedition 395 scientific objectives depend on the recovery of complete stratigraphic sections. Such sections cannot be recovered from a single IODP borehole because core recovery gaps or additions occur between successive cores despite 100% or more nominal recovery (e.g., Ruddiman, Kidd, Thomas, et al., 1987; Hagelberg et al., 1995; Acton et al., 2002a). The construction of a complete composite section, referred to as a splice, therefore requires the combination of stratigraphic intervals from two or more holes cored at the same site over similar depths. To maximize the probability of bridging gaps between successive cores in individual holes, the starting depths below seafloor from which cores are recovered are offset between holes. This practice ensures that most missing sedimentary sections from intercore gaps in a given hole are recovered in one or more adjacent holes. Usually, at least two complete holes and a third partial hole must be cored to recover a complete section using the APC system at a site.

The composite section and splice construction methodology employed during Expedition 395 follows the basic strategy originally developed during ODP Leg 138 (e.g., Hagelberg et al., 1992, 1995) and later refined during many other ODP legs and IODP expeditions, specifically Expedition 397 (Abrantes et al., 2024). This strategy is now common practice on all high-resolution paleoceanographic expeditions. Assembly and verification of a complete composite stratigraphic section

requires construction of the core composite depth below seafloor, Method A (CCSF-A), depth scale. The CCSF-A depth scale provides a common scale for the holes at a site that is different from the original CSF-A depth scale, which uses drilling measurement as the top depth and curated length as the bottom depth. It is also different from the DSF depth scale because of deviations in the length of core recovery as a result of expansion (common), compression, and core loss. The DSF, CSF-A, and CCSF-A depth scales are unique to each hole.

7.1. Depth scale for individual holes

The depth to the top of each core is based on the DSF depth scale, which is determined by the length of drill string below the rig floor to the top of the cored interval minus the length of drill string from the rig floor to the mudline (assumed to be the seafloor). The depth to a point along the core is determined by adding the position at which the point occurs to the core top depth. This is referred to as the CSF-A depth scale, which is equivalent to the ODP mbsf depth scale.

The zero-depth point of the mbsf scale is defined by the mudline in the first core of each hole. However, it is often difficult to tell whether this empirical mudline recovers the true sediment/water interface. Some holes are inadvertently (or purposely) started below this interface. In this case, the zero-depth point on the mbsf scale may be substantially offset from the zero-depth point in adjacent holes that successfully recover the sediment/water interface. The mbsf scale may also be inaccurate because of ship heave, tidal variations in sea level, and other sources of error. Tidal influence on depth was first predicted during ODP Leg 138 (Hagelberg et al., 1995) and was proven by correlation of affine offset changes and tide height during ODP Leg 202 (Shipboard Scientific Party, 2003). Tidal influence was not considered for the construction of the splices during Expedition 395.

7.2. Depth scale from composite holes

The goal of constructing a composite depth scale is to place coeval, laterally continuous stratigraphic features onto a common depth. This objective is achieved by shifting the CSF-A depth scales of individual cores to optimize correlation between holes. On the CCSF-A depth scale, the depths of the individual cores can only be shifted by one tie point between any two cores; it is therefore not corrected for differential expansion or contraction of the relative depth scale between the holes. Ultimately, this approach provides a good first-order correlation between cores from different holes. The CCSF-A scale provides a basis on which higher order correlations can be built to connect off-splice cores to the splice.

The mudline for the CCSF-A scale is the top of the first core with the most representative or best-preserved mudline. This mudline establishes the top of the stratigraphic section, and the core with this mudline becomes the anchor for the CCSF-A scale. It is typically the only core for which the depths are the same on both the CSF-A and CCSF-A scales. Each core downhole is tied to the composite section by adding or subtracting a depth offset (a constant) that best aligns the observed lithologic variations to the correlative variations for cores from adjacent holes. Provided that gaps between cores do not occur at the same stratigraphic position in offset holes and recovery is high, it should be possible to correlate each successive core downhole to a core from an adjacent hole. Gaps common to all holes cored at a site can occur, in which case there is a gap in the splice. In this case, cores farther down the hole can be appended to the composite section with the depth offset for the appended core adjusted to convey an estimate of the true size of the coring gap. For example, one could use the average growth factor (i.e., expansion) of the CCSF-A scale relative to the CSF-A scale, or where logging is available one could use continuous logging data from a hole at the site or observations from other nearby sites.

In the process of constructing the composite section, the CCSF-A scale is nearly always expanded relative to the CSF-A scale. This expansion, which is typically ~5%–15%, is mostly caused by decompression of the cores as they are brought to the surface, by stretching that occurs as part of the coring process, and/or by the curation practice in which material that has fallen downhole or gas expansion voids are curated as part of the core (e.g., Hagelberg et al., 1995; Acton et al., 2002a).

7.3. Goals

The goals for stratigraphic correlation for Expedition 395, in order of priority, are as follows:

- Guide the drilling process to ensure recovery of the most complete possible stratigraphic section.
- Establish a composite depth scale.
- Define a stratigraphically complete and representative sampling splice.

This first-order ship-based correlation is expected to be refined postcruise with the generation of adjusted or revised composite depth scales based on XRF data, which may also be used to refine linkages between core and logging depths at sites where logging was done.

7.4. Splice

The splice is a composite stratigraphic section that represents the complete record through intervals at a site and is composed of core sections from adjacent holes such that coring gaps in one hole are filled with core from an adjacent hole. An effort is also made to minimize the inclusion of disturbed sections or intervals of sediment fall-in (typically the uppermost ~10–100 cm of a core) or flow-in. Disturbed sections are identified by examining the cores and their photographs and X-rays. The splice ultimately should guide core sampling for high-resolution studies.

We tried to adhere to the following guiding principles while making the splice:

- Tie points were defined, where possible, close to stratigraphic intervals that showed reduced variability to minimize the possibility that splice jumps occur during important climate transitions.
- Where possible, we avoided using the first and last sections of cores where disturbance due to drilling artifacts (even if not apparent in core logging data) is most likely.
- We attempted to incorporate those parts of the stratigraphic sequence that in our judgment were most representative of the holes recovered and appeared to be the least disturbed.
- Where possible, we also considered future XRF core scanning efforts by making the splice between two holes only, even if more holes were available for the covered stratigraphy. Likewise, where possible, preference was given to records from Expedition 395 over Expedition 395C to allow for a spliced X-ray image record because those were not acquired during Expedition 395C. However, the highest priority was to not compromise the quality of the splice, so when needed, intervals of a third hole were included to ensure stratigraphic continuity.

7.5. Measurements and methods specific to Expedition 395

MS data from whole-round measurements were used for near real-time correlation during coring operations. These data often reveal strong contrasts between lithologic sequences, and the data can be obtained shortly after the core is recovered on deck at 5.0 cm resolution on the STMSL to guide operational decisions. The whole-round MS data collected at 2.5 cm resolution using the WRMSL were used to construct the final shipboard splices. Final correlation was always primarily based on the WRMSL MS profiles, but when in doubt it was occasionally supplemented by whole-round density, NGR, and paleomagnetic data.

Hole-to-hole correlations were accomplished using the Correlator software (Version 4.0.1). Using Correlator, we generated standard affine tables, which list the offset that is added to each core to place it in the CCSF-A scale, and splice tables, which give the intervals that comprise the splice. The tables were uploaded to the LIMS database using the Stratigraphic Correlator Data Management application SCORS, which will provide composite depths in the CCSF-A scale.

If overlapping small gaps in recovery between holes were identified but at least two holes could still clearly be correlated to each other and to the downhole logging data, the composite depth scale was extended using the estimated gap sizes relative to the logging profiles. When the correlation between different holes was no longer possible, the composite depth scale was stopped. To estimate the sizes of inferred gaps for Sites U1554, U1562, and U1564, the MS profiles from downhole logging were compared with the MS data from the WRMSL. For Site U1602, the downhole

logging MS data could not be easily correlated with the MSP data measured on the cores and was therefore not used to assess the size of potential gaps in the recovered cores. Comparison of the lower resolution NGR signals from the downhole logging and core point measurements suggests that there are no large stratigraphic recovery gaps for the spliced interval at Site U1602. However, because of the relatively low resolution of both NGR records and the edge effect for NGR as measured on cores, it was difficult to estimate the sizes of the gaps in correlation. Consequently, when it was not possible to tie to another core, the next core used in the composite was simply appended without modifying the distance between cores. At Sites U1555 and U1563, single holes were cored through the sedimentary sequence, and therefore splices and composite depth scales were not constructed.

8. Paleomagnetism

Paleomagnetic investigations were conducted on archive-half sections during Expeditions 384, 395C, and 395. Discrete samples were collected and analyzed only during Expeditions 384 and 395. The primary objectives were to determine directions of natural remanent magnetization (NRM) components, including magnetic polarity, and downhole variation of magnetic properties. Shipboard polarities were used to infer magnetostratigraphy in near real-time to inform operational decision making.

Routine measurements were carried out on archive halves using in-line stepwise alternating field (AF) demagnetization on a 2G Enterprises Model-760R-4K SRM equipped with direct-current superconducting quantum interference devices (DC-SQUIDS) and an in-line, automated AF demagnetizer capable of peak fields of 80 mT. Measurements of archive halves were conducted using the SRM software (IMS-SRM Version 10.2 for Expeditions 384 and 395C; IMS-SRM Version 14.0 for Expedition 395) assuming a sample area of 17.5 cm² for conversion to volume-normalized magnetization units (A/m).

The spatial resolution for archive-half measurements is a function of the integrated response function, with effective lengths of 7.36 cm for the X-axis, 7.22 cm for the Y-axis, and 9.12 cm for the Z-axis (Acton et al., 2017). The practical noise level of the SRM is $\sim 1 \times 10^{-9}$ Am² and is primarily controlled by the magnetization of the core liner and the background magnetization of the measurement tray. In soft sediments, discrete samples were collected with Natsuhara-Giken cubes (2 cm external edge length and internal volume of ~ 7 cm³) (Figure F15B). Cubes were hand-pushed or extracted from the working half of the core with the up arrow on the cube pointing upcore. In lithified sediments and hard rocks, 2 cm cubes (8 cm³ sample volume) were cut with a parallel saw. All discrete samples were subjected to AF demagnetization treatments using the DTECH (model D-2000) AF demagnetizer or thermally demagnetized using a thermal specimen demagnetizer (ASC Scientific model TD-48SC) and were measured on a spinner magnetometer (AGICO JR-6A). To avoid contamination by the ambient magnetic field prior to shipboard measurements, the

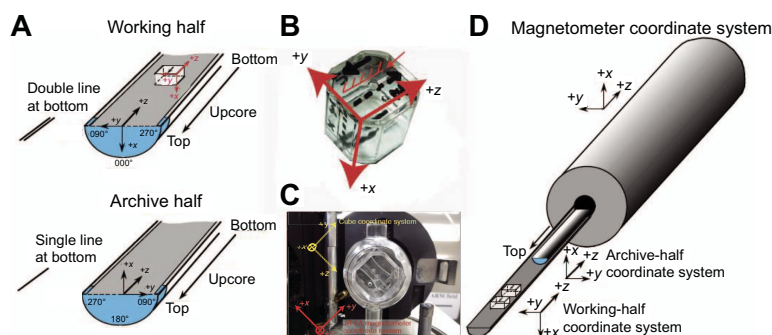


Figure F15. A. IODP paleomagnetic sample coordinates (modified after Richter et al., 2007). B. Natsuhara-Giken sampling cubes (7 cm³ volume) with sample coordinate system. Red etched arrow is parallel to the up arrow (oriented toward the top of the core) on the sample cube and points in $-z$ -direction. C. Measurement positions and coordinates used in the JR-6A spinner magnetometer aboard *JOIDES Resolution*. D. SRM coordinate system used aboard *JOIDES Resolution*.

discrete samples were stored inside a cylinder made of three mu-metal shields, providing a suitable low-field environment.

Ocean drilling cores generally carry secondary remanence components or overprints, such as a viscous remanent magnetization, resulting in a steep downward-pointing component imparted by the drilling process (Acton et al., 2002b). To separate these overprints from the characteristic remanent magnetization (ChRM), stepwise AF demagnetization was performed. Low AF values were selected to balance the competing goals of timely core processing and identifying and/or removing any drilling overprints, and preserving the NRM for high-resolution measurements during postcruise research. Archive-half and discrete data collected on the pass-through SRM and spinner magnetometer, respectively, were uploaded to the LIMS database.

Stepwise demagnetization data were analyzed using principal component analysis (PCA) to define the ChRM (Kirschvink, 1980). Zijderveld demagnetization plots (Zijderveld, 1967), intensity of magnetization versus demagnetization steps, and equal area projections and PCA were conducted using the PuffinPlot software (Version 1.4.1; Lurcock and Florindo, 2019).

8.1. Magnetic measurements on archive-half sections

The NRM of archive-half sections was measured using the SRM. Stepwise AF demagnetization was performed on most archive-half sections using the SRM in-line AF demagnetizer, which applies a field to the X -, Y -, and Z -axes of the SRM in this fixed order (Figure F15).

The response functions of the pick-up coils of the DC-SQUID sensors have a full width of 7.25–9.15 cm at half height. Therefore, data collected within ~4 cm of piece margins (or voids) can be affected by edge effects and are treated with caution. For this reason, basalt fragments with dimensions smaller than 8 cm were not analyzed.

The resolution and the demagnetization step sequence were modified during the three expeditions because of time constraints imposed by the laboratory workflow. Resolution varied from 1 to 5 cm spacing for sedimentary material and from 1 to 2 cm spacing for basalts, with a tray speed of 10 cm/s. Demagnetization steps were variable, ranging from NRM-only measurements (when multiple holes were drilled at the same depth intervals) to demagnetizations up to 40 mT. The resolution, measurement sequence steps, and spacing of each hole can be found in Table T7.

Measurement of basalt NRM and subsequent demagnetization steps was either 1 or 2 cm. Demagnetization went up to 25 or 30 mT, and steps were mostly every 5 mT (Table T7). During Expeditions 395C and 395, to avoid flux jumps and an excessive load on the SRM, selected pieces of core (>8 cm) from each section were individually measured in the SRM. This procedure also prevented smaller pieces of basalts from being unintentionally demagnetized.

AF demagnetization results from sediments and basalts were evaluated as downhole variations with depth. Inclination data were plotted downcore together with the NRM intensity and the low-field MS (or κ) measured on archive halves using the SHMSL (see [Physical properties](#)). For the purposes of comparison, these MSP measurements are referred to as MS in Paleomagnetism in each site chapter.

8.2. Magnetic measurements on discrete samples

During Expedition 384, a small set of discrete samples were taken from the working-half sections for MAD and magnetic property measurements (Blum et al., 2020). During Expedition 395, one to three discrete samples per 10 m were collected from working halves for both the sediments and the basalts, only at depth intervals that were not previously cored during Expeditions 384 or 395C. For the sediments, discrete sample locations were chosen preferentially in fine-grained intervals where drilling deformation was minimal or not visible.

Incremental AF demagnetization was performed until samples were completely demagnetized, generally up to 45 mT for the lower coercivity samples and up to 100 mT for high-coercivity samples. Thermal demagnetization was performed up to 400°–600°C at 25°–50°C steps until complete demagnetization was reached.

During Expedition 384, the anisotropy of magnetic susceptibility (AMS) was measured on an AGICO KLY4 instrument at a field of 200 A/m using the SUFAR (AGICO) program. The AGICO KLY4 measures AMS by rotating the sample along three axes, stacking the data, and calculating the best-fit second-order tensor. Expedition 395 used an AGICO MFK2 instrument operating at a 425 A/m field. Both instruments also measure the volume-normalized calibrated bulk susceptibility (χ). Data processing occurred in the same manner across both expeditions. AMS is a second-order tensor that can be used as a proxy for the orientation of the paramagnetic (mainly phyllosilicates) and ferromagnetic minerals in the sediments. It can be interpreted in terms of depositional processes because settling particles typically produce an oblate magnetic fabric with the minimum axis of susceptibility (κ_3) at the pole of the depositional plane, and the maximum (κ_1)

Table T7. Demagnetization parameters, Expedition 395. * = basement half cores, † = basement intervals smaller than 8 cm were not discarded from these measurements. [Download table in CSV format.](#)

Hole	Section(s)	Spacing (cm)	Demagnetization steps (mT)
384-			
U1554A	1H-1A to 1H-4A	1	0-2-4-6-8-10-12-14-16-18-20-25
U1554A	2H-1A to 8H-7A	1	0-2-6-10-15-20-25
U1554B	1H-1A to 8H-7A	1	0-2-6-10-15-20-25
U1554C	1H-1A to 2H-2A	1	0-2-4-6-8-10-12-14-16-18-20-22-25
U1554C	2H-3A to 8H-7A	1	0-2-6-10-15-20-25
U1555F†	1R-1A to 1R-2A	1	0-2-6-10-15-20-25
U1555F†	3R-1A to 9R-1A	1	0-5-10-15-20
U1555G†	2R-1A to 27R-3A	1	0-5-10-15-20
395C-			
U1554E	1H-1A to 25X-4A	1	0-10-15-20-25-35
U1554E	26X-1A to 34X-7A	2.5	0-15-20-25-35
U1554E	35X-1A to 61X-7A	2.5	0-15-20-25
U1554E	62X-1A	2.5	0-5-10-15-20-25-30
U1554F	3R-1A to 3R-3A	2	0-10-15-20-25
U1554F*	3R-4A to 32R-3A	2	0-10-15-20-25
U1555H	1H-1A to 20X-5A	1	0-10-15-20-25-35
U1555I	2R-1A to 3R-3A	1	0-10-15-20-25-35
U1555I	3R-4A	1	0-10-20-25-30
U1555I*	4R-1A to 41R-2A	2	0-5-10-15-20-25-30
U1562A	1H-1A to 57F-4A	2.5	0-10-15-20-25
U1562A	58X-1A to 65X-1A	2.5	0-15-20-25
U1562B*	2R-1A to 32R-2A	2	0-10-15-20-25
U1563A	1H-1A to 48X-1A	2.5	0-10-15-20-25
U1563A	48X-2A to 48X-4A	2.5	0-15-20-25
U1563B	2R-1A to 2R-3A	2	0-10-15-20-25
U1563B*	3R-1A to 28R-1A	2	0-10-15-20-25
U1564A	1H-1A to 1H-7A	5	0-15-20
U1564B	1H-1A to 3H-7A	5	0-15-20
U1564C	1H-11A to 75X-7A	5	0-15-20
395-			
U1554G	1H-1A to 40X-7A	5	NRM only
U1554H	1H-1A to 7H-6A	2.5	NRM only
U1554H	8H-1A to 34X-2A	2.5	0-10-15-20
U1554H	34X-3A to 38X-7A	5	0-10-15-20
U1562C	1H-1A to 1H-4A; 12H-2A to 53F-4A	5	0-10-15-20
U1562C	2H-1A to 12H-1A	2.5	0-10-15-20
U1564D	1H-1A to 51X-4A; 56X-1A to 74X-2A	2.5	0-10-15-20
U1564D	51X-5A to 55X-CCA	2.5	0-10-15-20-25-30
U1564E	1H-1A to 28X-7A	5	0-10-15-20
U1564F	2R-1A to 44R-1A	2.5	0-10-15-20-25-30
U1564F*	44R-2A to 68R-3A	1	0-5-10-15-20-25-30-35-40
U1564F*	69R-1A to 76R-2A	1	0-5-10-15-20-25
U1602A	1H-1A to 1H-6A	2.5	0-10-15-20
U1602B	1H-1A to 38F-4A	2.5	0-10-15-20
U1602C	1H-1A to 33F-4A	2.5	NRM only
U1602C	34F-1A to 39F-3A	2.5	0-10-15-20-25
U1602D	1H-1A to 52X-5A	2.5	0-10-15-20
U1602D	47X-CCA; 48X-CCA; 49X-CCA; 50X-CCA; 51X-CCA; 52X-6A to 66X-1A	2.5	0-10-15-20-25
U1602E	2R-1A to 31R-3A; 40R-6A; 52R-1A to 52R-3A	2.5	0-10-15-20-25
U1602E	31R-4A to 40R-5A; 41R-1A to 51R-2A; 52R-4A to 71R-3A; 72R-2A to 73R-1A; 74R-2A	2.5	0-10-15-20-25-30
U1602E	72R-1A; 73R-2A to 74R-1A; 74R-3A to 88R-2A	2.5	0-5-10-15-20-30

and intermediate (κ_2) susceptibility axes are girdled ($\kappa_1 \approx \kappa_3$), defining a planar, near horizontal, gravity-induced settling fabric. If sediments are deposited by flowing water, the resulting AMS ellipsoid is characterized by a magnetic foliation oriented with the current; it can be either a horizontal or tilted (imbricated) foliation, and/or characterized by clustering of the κ_1 parallel to the flow direction. Disturbance by slumping or other deformation may yield triaxial fabrics whereby the three axes have different values ($\kappa_1 \neq \kappa_2 \neq \kappa_3$).

During Expedition 395, a subset of discrete samples was measured for anhysteretic remanent magnetization (ARM) and isothermal remanent magnetization (IRM). An ARM of 50 μT bias AC field at a 100 mT demagnetizing DC was imparted along the Z-axis of the samples using the DTECH AF demagnetizer, and remaining magnetization was measured using the JR-6A spinner magnetometer. The acquired ARM and IRM were subsequently demagnetized with the DTECH AF demagnetizer using the same steps used to demagnetize the NRM.

IRM was imparted to discrete samples using the ASC Scientific IM-10 impulse magnetizer. Fields of 100, 300, 500, and 1000 mT were applied to the samples. After each step, the acquired magnetization of the cubes was measured with the SRM. After the 1000 mT step, samples were demagnetized with the DTECH AF demagnetizer using the same steps used for NRM. The remaining magnetization after each step was measured using the SRM. After their complete demagnetization, a -100 mT field along the Z-axis was applied and the remaining magnetization was measured using the SRM.

Thermal demagnetization was performed on a subset of basement discrete samples. After measuring the NRM using the JR-6A spinner magnetometer, samples were heated to 50° and 100°C using the ASC Scientific TD-48 SC oven. The remaining NRM was measured after each temperature step using the JR-6A spinner magnetometer. Samples were then subjected to the MAD protocol for physical properties tests (see [Physical properties](#)) and returned to the paleomagnetic laboratory for further heating at 25° or 50°C increments up to 600°C, when most samples were fully demagnetized.

8.3. Coordinates

All magnetic data are reported relative to IODP orientation conventions as follows: $+x$ is into the face of the working half, $+y$ points toward the left side of the face of the working half, and $+z$ points downcore. The relationship of the SRM coordinates (X -, Y -, and Z -axes) to the data coordinates (x -, y -, and z -directions) is as follows: for archive halves, x -direction = X -axis, y -direction = $-Y$ -axis, and z -direction = Z -axis; for working halves, x -direction = $-X$ -axis, y -direction = Y -axis, and z -direction = Z -axis (Figure F15).

8.4. Core orientation

Orientation of APC cores was achieved with the FlexIT Tool 0937 for a subset of cores from Expedition 384 and an Icefield MI-5 (2007, 2043, or 2052) for all other cores. These tools consist of triaxial magnetometers and accelerometers. These sensors provide an azimuthal correction for the core barrel that, combined with the local magnetic declinations, allows the measured NRM declinations to be transformed into true geographic coordinates. In the orientation deployment, the tool is connected to the core barrel with the double lines on the core liner at a fixed and known angle relative to its sensors. After Expedition 384, misalignment of 180° for the Icefield MI-5 2043 was avoided by regularly checking the alignment of the keys and using each Icefield tool with a specific pressure barrel and end seal (Blum et al., 2020).

8.5. Magnetostratigraphy reference scale and interpretations

The magnetostratigraphy at each site was constructed by correlating observed polarity sequences with a reference GPTS. The GPTS used for Expeditions 395C and 395 (Table T8) is the GPTS2020 synthesis of astronomical tuning of Cenozoic through the latest Cretaceous polarity zones presented in Ogg (2020).

The magnetozones were established from pass-through measurements after AF demagnetization using the inclinations from the maximum demagnetization step. The geomagnetic polarity sequence was then verified by the inclination for the ChRMs from the discrete samples.

For Holes U1562A, U1564D, U1602D, and U1602E, the edge effect was removed to better refine the magnetostratigraphy (Richter et al., 2007). For sedimentary rocks that formed in high latitudes, no polarity ambiguity arises and inclination only can be used to estimate the magnetic

Table T8. Cenozoic magnetic polarity chron nomenclature and age model as used in the GPTS (Ogg, 2020). For consistency throughout this volume, we use the stage boundaries as documented in table 29.8 in Raffi et al. (2020), although we note that in places these are not fully consistent with the reversal ages that are associated with the stage boundary. GSSP = Global Boundary Stratotype Section and Points. [Download table in CSV format.](#)

Period	Epoch	Age/stage	Base age (Ma)	Chron	Polarity chron/subchron	Base of chron/subchron (Ma)	Duration (My)	Remarks		
Quaternary	Holocene		11.8 ka		Present	0.000				
	Pleistocene	late (Tarantian)	0.13	C1	C1n (Brunhes)	0.773	0.773	Base of Middle Pleistocene (Ionian) is base of Brunhes Chron		
					C1r.1r (Matuyama)	0.990	0.217			
		middle (Ionian)	0.773		C1r.1n (Jaramillo)	1.070	0.080			
					C1r.2r	1.180	0.110			
		early (Calabrian)	1.80		C1r.2n (Cobb Mountain)	1.215	0.035			
					C1r.3r	1.775	0.560			
					C2n (Olduvai)	1.934	0.159		Base of Calabrian is in lower part of Olduvai Chron	
					C2r.1r	2.116	0.182			
		early (Gelasian)	2.59		C2	C2r.1n (Feni)	2.140		0.024	Formerly named Reunion
						C2r.2r (Matuyama)	2.595		0.455	Base of Pleistocene is near base of Matuyama Chron
	Neogene	Pliocene	late (Piacenzian)	3.60	C2A	C2An.1n (Gauss)	3.032	0.437	Gauss Normal Chron (C2An) contains two reversed intervals: Kaena (Chron 2An.1r) and Mammoth (Chron 2An.2r)	
C2An.1r (Keana)						3.116	0.084			
C2An.2n						3.207	0.091			
C2An.2r (Mammoth)						3.330	0.123			
C2An.3n (Gauss)						3.596	0.266	Base of Piacenzian is base of Chron C2An.3n		
C2Ar (Gilbert)						4.187	0.591	Gilbert Reversed Chron spans Chrons C2Ar through C3r		
early (Zanclean)			5.33	C3	C3n.1n (Cochiti)	4.300	0.113			
					C3n.1r	4.493	0.193			
					C3n.2n (Nunivak)	4.631	0.138			
					C3n.2r	4.799	0.168			
					C3n.3n (Sidufjall)	4.896	0.097			
					C3n.3r	4.997	0.101			
Miocene		late (Messinian)	7.246	C3A	C3n.4n (Thvera)	5.235	0.238	Base of Pliocene is in uppermost Chron C3r		
					C3r (Gilbert)	6.023	0.788			
					C3An.1n	6.272	0.249			
					C3An.1r	6.386	0.114			
					C3An.2n	6.727	0.341			
					C3Ar	7.140	0.377			
		late (Tortonian)	11.65	C3B	C3Bn	7.214	0.110			
					C3Br.1r	7.262	0.048	Base of Messinian is in lowermost Chron C3Br.1r		
					C3Br.1n	7.305	0.043			
					C3Br.2r	7.454	0.151			
					C3Br.2n	7.499	0.043			
					C3Br.3r	7.537	0.038			
C4n.1n	7.650	0.113								
Miocene	late (Tortonian)	11.65	C4	C4n.1r	7.701	0.051				
				C4n.2n	8.125	0.424				
				C4r.1r	8.257	0.132				
				C4r.1n	8.300	0.043				
				C4r.2r	8.771	0.471	Cryptochron C4r.2r-1 is within Chron C4r.2r (~8.661–8.699 Ma)			
				C4An	9.105	0.334				
	C4A	C4Ar.1r	9.311	0.206						
		C4Ar.1n	9.426	0.115						
		C4Ar.2r	9.647	0.221						
	C5	C4Ar.2n	9.721	0.074						
		C4Ar.3r	9.786	0.065						
		C5n.1n	9.937	0.151						
C5n.1r		9.984	0.047							
C5n.2n		11.056	1.072							
C5r.1r		11.146	0.090							
C5	11.65	C5	C5r.1n	11.188	0.042					
			C5r.2r	11.592	0.404	Subchron C5r.2r-1 is within Chron C5r.2r (~11.263–11.308 Ma)				
			C5r.2n	11.657	0.065	Base of Tortonian is near base of Chron C5r.2n				

polarity. The quality of the paleomagnetic data was improved by removing those intervals affected by core disturbance (e.g., soupy or flow-in intervals). Any polarity changes occurring at the beginning and end of core sections are treated with caution.

The polarities were indexed in numerical order from the top to bottom of each hole with the prefixes *n* for normal and *r* for reversed polarities. When possible, the interpretation of magnetic polarity intervals was provided, adopting the naming and numbering convention of the reference GPTS (Ogg, 2020). For the younger part of the timescale (Pliocene–Pleistocene), the traditional names were used to refer to chrons and subchrons (e.g., Brunhes, Jaramillo, Olduvai).

9. Geochemistry and microbiology

A full suite of shipboard geochemical data were collected during Expeditions 395 and 395C; however, only hydrocarbon gas concentration data were collected during Expedition 384. Unless noted, methods were identical for Expeditions 395 and 395C. Routine measurements included headspace analysis of hydrocarbon gases, in situ pore water oxygen measurements, IW chemistry (e.g., salinity, pH, alkalinity, major cations and anions, nutrients, and major and minor elements), loss on ignition (LOI), total carbon (TC), total inorganic carbon (TIC), total sulfur (TS; Expedition 395 only), and elemental compositions of sediments and basement rocks using ICP-AES. Additional geochemical analyses of basement rock chemistry were conducted using a handheld pXRF. All data generated by shipboard analyses were uploaded to the LIMS database. Samples for microbiological analyses, focused on culture-independent approaches, were obtained alongside geochemical measurements for shore-based processing and analyses.

9.1. Headspace hydrocarbon gas chemistry

Routine analyses of hydrocarbon gas concentrations in sediment cores is standard IODP procedure and ensures safe drilling operations (Kvenvolden and McDonald, 1986; Pimmel and Claypool, 2001). During Expeditions 395 and 395C, sediment samples for headspace gas monitoring were typically taken from the top of Section 3 (below the IW sample taken from the base of Section 2), or from the same whole-round core used for IW or microbiological sampling. During Expedition 384, sediments for headspace gas analyses were taken from the top of Section 7. Soft-sediment sampling consisted of a ~ 5 cm³ plug collected using a graduated syringe and extruded into a 21.5 cm³ glass serum vial with a crimped-seal aluminum cap and fluoropolymer/silicone septum. Consolidated or lithified samples were collected as chips of sediment that were placed in the vial and sealed. Vials were then heated in an oven at 80°C for 30 min.

A 5 cm³ aliquot of the evolved hydrocarbon gas was extracted from the headspace vial with a standard gas syringe and then manually injected into an Agilent 7890 Series II gas chromatograph (GC) equipped with a flame ionization detector set at 250°C to quantify concentrations of methane (C₁), ethane (C₂), ethylene (C₂₌), propane (C₃), and propylene (C₃₌). The injector consists of a 1/16 inch Valco union with a 7 μm screen connected to a Valco-to-Luer lock syringe adapter. This injector connects to a 10-port Valco valve that was switched pneumatically by a digital valve interface. The injector temperature was set at 120°C. Samples were introduced into the GC through a 0.25 cm³ sample loop connected to the Valco valve. The valve can be switched automatically to back flush the column. The GC column (2 mm inner diameter; 6.3 mm outer diameter) was packed with 80/100 mesh HayeSept (Restek). The GC oven program was maintained at 80°C for 8.25 min with a subsequent heat-up to 150°C at 40°C/min. Helium was used as the carrier gas, and the initial helium flow in the column was 30 mL/min. The helium flow was then ramped to 60 mL/min after 8.25 min to accelerate elution of C₃ and C₃₌. The run time was 15 min. The GC was also equipped with an electronic pressure-control module to control the overall flow into the GC. Data were collected and evaluated using the Hewlett Packard 3365 ChemStation data processing software. The chromatographic response was calibrated daily using nine gas standards with variable quantities of low-molecular weight hydrocarbons provided by MESA Calibration Gas Standards. Table T9 lists precision and detection limits for the headspace gas analyses during Expeditions 384, 395, and 395C. Concentrations of hydrocarbon gases are reported in parts per million by volume.

9.2. Interstitial water chemistry

Whole-round samples 5–20 cm in length were cut on the catwalk for IW extraction, immediately capped, and transferred to the chemistry laboratory for squeezing. IW samples were typically taken from the bottom of Section 2 (Expedition 395) or Section 4 (Expedition 395C). During Expedition 395, high-resolution IW sampling (bottom of Sections 1, 3, 4, 5, and 6) was conducted on 10 cm whole-round samples in the first core at each site (Holes U1564D, U1554G, and U1602B) for shipboard and shore-based measurements. Exposed surfaces of each whole-round sample were carefully scraped under ambient laboratory conditions using stainless steel knives to minimize contamination due to seawater, drilling disturbances, and/or sediment smearing along the insides of the core liners. When sampling sediment collected using the XCB or RCB systems, sediment for pore water extraction was carefully selected to avoid disturbed materials or infill. The selected sediment samples were transferred to titanium squeezers and put in a Carver hydraulic laboratory press where they were squeezed to extract IW at pressures up to 30,000 force pounds ($\sim 1.335 \times 10^6$ N) (Manheim and Sayles, 1974). A minimum of 30 min of squeezing was required for all cores, and >12 h of squeezing was required to extract sufficient IW from deeper XCB or RCB cores. IW samples were first passed through a nanopure water–precleaned Whatman Number 1 filter above a titanium screen into a 60 mL high-density polyethylene (HDPE) syringe that had been acid-cleaned with 10% HCl. A 0.45 μ m polyethersulfone membrane filter was attached to the syringe tip upon collection of IW from the squeezers. The collected fluids were then filtered through a 0.2 μ m polyethersulfone membrane filter into appropriate containers and processed for shipboard and postcruise analyses. Following IW extraction, squeeze cake residues were sampled for shipboard analyses (e.g., TC, TS, and TIC). Total organic carbon (TOC) was determined by subtracting the TIC weight percent from the TC weight percent. The squeeze cake residues were

Table T9. Precision and detection limits for procedures used for IW, HS, and sediment geochemistry, Expeditions 384, 395, and 395C. * = calculated as 3 \times standard deviation of blank. † = based on replicate analyses of standards. RSD = SD/average \times 100. ND = not determined, NA = not available. NGA-FID = natural gas analyzer with flame ionization detector, NGA-TCD = natural gas analyzer with thermal conductivity detector. [Download table in CSV format.](#)

Instrument	Analyte	Unit	Limit of determination*	Precision (%)†	Standards
Extec RE300 ExStik ORP Meter	eH	mV	ND	1.6	240 mV ORP Test Solution
Titration	Alkalinity	mM	ND	2.0	100% IAPSO
Titration	pH	None	NA	1.4	100% IAPSO
Ion chromatography	Na	mM	0.063	0.5	100% IAPSO
Ion chromatography	Cl ⁻	mM	0.0075	0.7	100% IAPSO
Ion chromatography	Br ⁻	mM	0.017	1.2	100% IAPSO
Ion chromatography	SO ₄ ²⁻	mM	0.027	0.7	100% IAPSO
Ion chromatography	K ⁺	mM	<0.01	1.3	100% IAPSO
Ion chromatography	Ca ²⁺	mM	<0.01	1.8	100% IAPSO
Ion chromatography	Mg ²⁺	mM	<0.01	0.6	100% IAPSO
UV-Visible spectrophotometry	NH ₄ ⁺	μ M	0.2	ND	NH ₄ Cl
UV-Visible spectrophotometry	PO ₄ ³⁻	μ M	0.5	ND	KH ₂ PO ₄
TECAN plate reader spectrophotometer	NH ₄ ⁺	μ M	1.0	10	NH ₄ Cl
TECAN plate reader spectrophotometer	PO ₄ ³⁻	μ M	2.7	ND	KH ₂ PO ₄
Coulometry	TIC	wt%	NA	0.5	100% reagent grade CaCO ₃
Coulometry	CaCO ₃	wt%	NA	0.6	100% reagent grade CaCO ₃
CHNS analyzer	C	wt%	ND	0.9	Buffalo River Sediment
CHNS analyzer	N	wt%	ND	8.6	Buffalo River Sediment
Coulometry/CHNS	TOC	wt%	NA	NA	NA
NGA-FID	Methane	ppmv	1	1.7	MESA Calibration Gas Mixture
NGA-FID	Ethane	ppmv	0	2	MESA Calibration Gas Mixture
NGA-FID	Ethane	ppmv	0	2.3	MESA Calibration Gas Mixture
NGA-FID	Propene	ppmv	0	2	MESA Calibration Gas Mixture
NGA-FID	Propane	ppmv	0	15	MESA Calibration Gas Mixture
NGA-FID	iso-butane	ppmv	0	11.7	MESA Calibration Gas Mixture
NGA-FID	n-butane	ppmv	0	3	MESA Calibration Gas Mixture
NGA-FID	iso-pentane	ppmv	0	7.4	MESA Calibration Gas Mixture
NGA-FID	n-pentane	ppmv	0	5.3	MESA Calibration Gas Mixture
NGA-FID	iso-hexane	ppmv	0	16	MESA Calibration Gas Mixture
NGA-FID	n-hexane	ppmv	0	10	MESA Calibration Gas Mixture
NGA-TCD	Nitrogen	ppmv	0	0.1	Laboratory air
NGA-TCD	Oxygen	ppmv	0	0.1	Laboratory air

also sampled for postcruise analyses and stored at 4°C. Squeezers were cleaned between samples with tap water, rinsed with 18.2 MΩ deionized water, and dried with compressed air.

9.2.1. Interstitial water analysis

IW samples were analyzed on board following the protocols in Gieskes et al. (1991), Murray et al. (2000), and the IODP user manuals for shipboard instrumentation.

9.2.1.1. Alkalinity, pH, Salinity, and Eh

Alkalinity, pH, salinity, and Eh were measured immediately on IW extracted by squeezing, following the procedures described in Gieskes et al. (1991). Salinity was measured with a Fisher Model S66366 optical refractometer. International Association for the Physical Sciences of the Oceans (IAPSO) standard seawater (salinity = 35) and 18.2 MΩ water (salinity = 0) were used to calibrate salinity. IW pH and alkalinity were determined using a Metrohm 794 Basic Titrino Autotitrator with a glass pH electrode. A 3 mL sample was titrated against 0.1 N HCl at 25°C to reach an endpoint of pH = 4.2. The IAPSO standard seawater (alkalinity = 2.325 mM; certified value) and laboratory standards (5 to 100 mM Na₂CO₃ alkalinity, made by mixing different proportions of 0.7 M KCl and 0.1 M Na₂CO₃) were used for calibration. The IAPSO standard was analyzed at the beginning and end of the sequence and after every 10 samples. Repeated measurements of IAPSO seawater for alkalinity yielded precision better than 2.5%. Eh was measured on an Extec RE300 ExStik ORP Meter (Cole-Parmer) on 2 mL of IW under ambient conditions. Calibration of Eh measurements were made with repeat measurements of 18.2 MΩ water (Eh = 0 mV) and Hanna Instruments H1702L ORP standard solution (Eh = 240 mV) (Table T9).

9.2.1.2. Ion chromatography

Sulfate (SO₄²⁻), chloride (Cl⁻), bromide (Br⁻), sodium (Na⁺), magnesium (Mg²⁺), potassium (K⁺), and calcium (Ca²⁺) concentrations were analyzed using ion chromatography (Metrohm 850 Professional IC) using 100 μL of squeezed IW diluted by 100 times with 18.2 MΩ water. For anions (Cl⁻, SO₄²⁻, and Br⁻), a Metrosep C6 column (100 mm long; 4 mm inner diameter) was used with 3.2 mM Na₂CO₃ and 1.0 mM NaHCO₃ solutions as eluents, whereas a Metrosep A Supp 7 column (150 mm long; 4 mm inner diameter) was used with 1.7 mM of HNO₃ and pyridine-2,6-dicarboxylic acid (PDCA) solutions as eluents for cations (Na⁺, K⁺, Mg²⁺, and Ca²⁺). The standards used were IAPSO in various dilutions (ranging 1%–150% IAPSO) to create a nine-point calibration curve. Reproducibility was checked on the repeated measurements of standard IAPSO and IAPSO dilution of 1:10 every 10 samples. Reproducibility (defined by standard deviation/average and relative standard deviation [RSD]) of repeated IAPSO measurements of IAPSO measurements ($n = 40$) was ≤1.8% for Cl⁻, SO₄²⁻, Na⁺, Mg²⁺, K⁺, Br⁻, and Ca²⁺ (Table T9).

9.2.1.3. Spectrophotometry of ammonium and phosphate

Aliquots of IW samples were diluted with 18 MΩ millipore water for analysis of ammonium (NH₄⁺) and phosphate (PO₄³⁻) using an Agilent Cary 100 UV-Vis spectrophotometer. Ammonium concentrations were determined using a colorimetric by phenol diazotization and subsequent oxidation by sodium hypochlorite to yield a blue color measured spectrophotometrically at a wavelength of 640 nm. Ammonium chloride (NH₄Cl) was used for calibration and standardization. Phosphate concentrations were measured through the reaction of orthophosphate with Mo (VI) and Sb (III) in an acidic solution, which formed an antimony-phosphomolybdate complex and was then reduced by ascorbic acid to form a blue color. After adding the mixed reagent solution and letting the samples react for 30 min, the absorbance was measured at 885 nm (Gieskes et al., 1991). Table T9 lists precision and detection limits for ammonium and phosphate standards.

9.2.1.4. Inductively coupled plasma–optical emission spectroscopy

Selected major and minor elements (Na, Ca, Mg, K, Li, B, P, Si, Ba, Fe, Mn, and Sr) were analyzed using the shipboard Agilent 5110 with an Agilent SPS4 autosampler inductively coupled plasma–optical emission spectroscope (ICP-OES) in atomic emission spectroscopy (AES) mode and is referred to as ICP-AES in this volume and in the LIMS/LORE database. Shipboard ICP-AES analyses for IW were modified from ODP Technical Note 29 (Murray et al., 2000) with updates related to the specifications of the current Agilent ICP-AES instrument. Internal standards were used to correct for instrument performance variations across the spectral range of the elements of interest. A 500 μL aliquot of each IW sample was diluted to 5 mL with 100 μL of an internal standard

solution containing 100 ppm Be, In, and Sc; 200 ppm Sb; and 4.4 mL of 2% HNO₃. Each batch of samples analyzed on the ICP-AES included blanks and reference samples of known concentrations. Each sample was analyzed three times in a sample run. Following each instrument run, the measured raw intensity values were automatically corrected for instrument drift and blank values, and calibration curves were calculated using Agilent's ICP Expert software (Version 7.3.0.1.9507).

Calibration curves for major cations (Na⁺, K⁺, Mg²⁺, and Ca²⁺) were established using a series of dilutions of IAPSO standard seawater (from 1:1 to 1:100 IAPSO:2% HNO₃). Standards for minor and trace element analyses (K, Li, B, Si, Ba, Fe, Mn, and Sr) were made from a stock multielement solution prepared from ultrapure primary standards (1000 ppm; SPEX CertiPrep reference standards) in 2% HNO₃ with 35 ppt NaCl. This stock solution was diluted using 2% HNO₃ + NaCl to produce a set of standards ranging 1%–100% of the stock solution elemental abundances. For consistency, calibration standards were diluted for ICP-AES measurement in the same way as the samples, which were run at a 10:1 dilution factor. The 1:1 standard was repeatedly analyzed with each batch of samples during the expedition. The ICP-AES plasma was ignited at least 30 min before the sample run to allow the instrument to stabilize. Each sample was analyzed three times from the same solution. For each run, the wavelengths with calibration curves showing the highest correlation coefficient (*r* value) for each element were used to determine concentrations. At the beginning of each ICP-AES batch run, a complete set of in-house and IAPSO standard dilutions were analyzed. Furthermore, known solutions of the IAPSO standard were run every six to eight samples to monitor instrument drift and accuracy. The elemental concentrations reported for each sample were average values from three replicate integrations for each sample. Reproducibility was typically better than 5% for all elements and mostly around 1%–3% (Table T10).

9.3. Oxygen measurements

During Expedition 395, dissolved oxygen concentrations were measured in sediments from Holes U1554G, U1562C, U1564D, U1564E, and U1602B to determine pore water dissolved oxygen profiles at each site. No dissolved oxygen measurements were made during Expeditions 384 and 395C. Oxygen concentrations were measured using a FireSting-O₂ optical meter following manufacturer instructions (Pyroscience sensor technology, Germany). O₂ sensors were calibrated daily using a two-point calibration with air-saturated deionized water (100% oxygen saturation) and an OXCAL O₂ calibration capsule (Pyroscience) solution (0% oxygen saturation). Oxygen measurements were determined using whole-core sections prior to splitting. A ~3 mm diameter hole was drilled in the core liner using a hand drill, and the oxygen microsensor was inserted manually ~2.5 cm into sediments at the desired measurement locations. The microsensor was placed 25–30 cm beneath the top of Section 2 for each core, the temperature sensor was placed 10 cm above the microsensor (~15–20 cm beneath the top of the section), and the signal was allowed to equilibrate to a steady value (~1 min on average, but sometimes up to 5 min). All calibration and measurement data were processed using the FireSting Logger Software (Version 2.365). After arriving on

Table T10. Shipboard ICP-AES method precision and detection limits for elements analyzed in interstitial waters, with the specific spectral lines used for each element, Expedition 395. * = calculated as 3× standard deviation of the IAPSO blank. † = based on replicate analyses of 100% IAPSO and 100% in house standards. [Download table in CSV format.](#)

Element (units)	Wavelength (nm)	Detection limit*	Precision (%) [†]
B (μM)	249.772	1.6	0.5
Ba (μM)	455.403	0.012	0.7
Ca (mM)	313.933	<0.001	0.6
Fe (μM)	238.204	0.24	0.8
K (mM)	766.491	<0.01	0.6
Li (μM)	670.783	0.4	0.6
Mg (mM)	277.983	0.012	0.5
Mn (μM)	257.61	0.044	0.3
Na (mM)	330.298	0.13	0.5
P (μM)	178.222	6.4	1.5
S (mM)	180.669	<0.001	0.2
Si (μM)	288.158	0.96	0.3
Sr (μM)	421.552	0.005	0.6

the catwalk, core sections were scanned with the STMSL by the physical properties team and immediately taken to the downhole logging laboratory, which allowed dissolved oxygen measurements to be taken <2 h after core arrival on deck. In lithified or firm sediments, the temperature and O₂ sensors could not be fully inserted into the core. A table of all O₂ data from Expedition 395 are included in GEOCHEM in [Supplementary material](#).

9.4. Sediment and basalt geochemistry

9.4.1. Inorganic and organic carbon, nitrogen, and sulfur

TIC was measured by quantifying the carbon dioxide evolved from an acidification process on a UIC Coulometrics 5017 CO₂ coulometer. Powdered bulk sediment was weighed (~10 mg) using a Cahn C-31 automated electrobalance system with two electronic balances and a computer averaging system that corrects for ship motion. The sediment was transferred to a clean sample vial, where it was reacted with 5.0 mL of 1 M HCl on a hot plate at 50°C for 2–5 min (depending on CaCO₃ content), until all CaCO₃ was converted to CO₂. Sample gas was then transferred using an N₂ carrier gas to a coulometer cell that was filled with a monoethanolamine solution and a colorimetric pH indicator. As the gas passed through the cell, CO₂ was quantitatively absorbed and reacted with the monoethanolamine to form a titratable acid. The increased acidity causes the color indicator to change, and the spectrophotometer tracked the change in light transmittance.

Weight percent calcium carbonate was calculated from the TIC content assuming that CO₂ was derived from calcium carbonate as follows:

$$\text{CaCO}_3 \text{ (wt\%)} = \text{coulometer reading (TIC; } \mu\text{g)} \times 8.333/\text{sample mass (mg)}.$$

This approach is based on the assumption that calcium carbonate is the only carbonate mineral present; therefore, the ratio of the molar mass of CaCO₃ (100.087 g/mol) and C (12.011 g/mol) equals 8.333. A standard reference material (>99.9% CaCO₃; Fisher Scientific) was used to determine analytical precision (TIC = 0.5 wt%; CaCO₃ = 0.6 wt%). Weight percent TOC was calculated by subtracting TIC from TC.

Concentrations of TOC, total nitrogen (TN), and TS (TS = Expedition 395 only) in sediments were determined using flash combustion on a ThermoScientific FlashSmart carbon-hydrogen-nitrogen-sulfur (CHNS) elemental analyzer. Approximately 15 mg of powdered sample was weighed into tin capsules on the Cahn C-31 automated electrobalance. To ensure complete combustion of sulfur, an equivalent mass of V₂O₅ catalyst was mixed with the sample before sealing the tin capsule. Samples were combusted in the elemental analyzer at 1020°C in a stream of helium. Nitrogen oxides were reduced to N₂ in the presence of reduced copper (650°C), and the CO₂, N₂, and SO₂ produced from the sample were separated on a GC column (2 m long). Sample gas intensities were detected using a thermal conductivity detector and normalized to a carbon-nitrogen-sulfur calibration standard (2.5-bis[5-tert-butyl-benzoxazol-2-yl]thiophene) (C = 72.53 wt%; N = 6.517 wt%; S = 7.44 wt%). Two reference standards (NIST 2704 and Buffalo River Sediment) were run every 10 samples to monitor for analytical drift and determine analytical precision (typically better than 5% for all elements).

9.4.2. X-ray diffraction

Approximately 5 cm³ of bulk sediment was collected for geochemical analyses from squeeze cake residue and/or directly sampled by the sedimentology team. Samples analyzed for bulk mineralogy were freeze-dried for >12 h and homogenized to a fine powder using an agate mortar and pestle. X-ray diffraction (XRD) analyses of bulk powders were performed using a Malvern Panalytical Aeris XRD system operated at 40 kV voltage, 15 mA current, and 5°–99° 2θ goniometer angle stepped through 0.0110° increments with a scan speed of 32.9 s/step. The divergence split for the operation was 0.23°.

Diffraction patterns of bulk samples were evaluated with either Malvern Panalytical HighScore Plus or Bruker EVA software, which allowed for basic peak characterization (e.g., background removal and characteristic peak intensity) and mineral identification. To identify minor mineral phases in the carbonate- and/or nannofossil-rich sediments at the base of the sedimentary sequence from

Hole U1564E, a small subset of samples was decarbonated using a 1 M sodium acetate buffer solution adjusted to pH 5.0 with acetic acid. Samples were broken into small pieces, which were placed into centrifuge tubes with 20 mL of buffer solution for 5 h. Following the leaching procedure, samples were centrifuged, the supernatant was decanted, and the remaining solids were mixed with a new buffer for another 5 h before final centrifugation and rinsing. These residual samples were then freeze-dried and subjected to the process described for bulk samples above. Remaining sample material was stored in a glass vial and archived.

9.4.3. Loss on ignition

As an initial estimate of the degree of alteration of basalt samples, 5.00 ± 0.05 g of each sample powder was weighed into a quartz crucible and then ignited to determine the weight loss on ignition. During Expeditions 395 and 395C, samples were heated for 4 h at 1025°C. Estimated precision is ± 0.02 g ($\pm 0.4\%$).

9.4.4. Bulk chemistry of sediment and basalt

Major oxide (Al_2O_3 , CaO , Fe_2O_3 , K_2O , MgO , MnO , Na_2O , P_2O_5 , SiO_2 , and TiO_2) and minor element (Ba, Cr, Cu, Ni, S, Sc, Sr, V, Y, Zn, and Zr) concentrations were determined using ICP-AES with the shipboard Agilent 5110. The shipboard ICP-AES analyses of samples closely followed the methods described by Murray et al. (2000). Each sediment, basalt, and reference material sample was treated according to the ICP Sample Preparation user guide (<https://tamu-eas.atlas-sian.net/wiki/spaces/LMUG/pages/7341017694/ICP+Sample+Preparation>). The calibration spreadsheet used during Expeditions 395C and 395 identifies sample types (e.g., blank, drift monitor, standard, check standard, or unknown), and, based on this information, completed all data corrections (internal standard, blank, and drift corrections, in that order). For bulk sediment geochemistry, ICP-AES measurements were taken from carbonate residues. For basalt samples, representative samples were cut from the working halves of cores recovered during Expeditions 395 and 395C for major and minor/trace element analyses. One sample of basalt was selected every ~ 10 m from the least altered material in the core to obtain a downhole record of the primary magmatic conditions. ICP-AES samples and a thin section billet were both taken from the same core interval where possible. Rock samples were then ultrasonicated in trace metal-grade 70% isopropyl alcohol for 15 min and in 18.2 M Ω deionized water for another 10 min. The cleaned rock pieces were dried for 12 h at 110°C and then crushed to <1 cm chips between two disks of Delrin plastic in a hydraulic press. The chips were powdered using a SPEX Shatterbox with a tungsten carbide grinding canister. As documented for previous IODP expeditions, contamination from the tungsten carbide mill is negligible for most of the elements analyzed during shipboard chemical analyses, although Co contamination during the powdering process is possible (Godard et al., 2009).

Powdered bulk sediment and basalt samples were weighed (100 ± 0.5 mg) and mixed with LiBO_2 flux (400.0 ± 0.5 mg). An aqueous LiBr solution (10 μL of 0.172 mM) was added to the flux and powder mixture as a nonwetting agent to prevent the fused bead from sticking to the crucible during cooling. Standard reference samples (AGV-1, BCR-2, BHVO-2, BIR-1, BRR-1, JB-1a, JB-2, JB-3, JGb-1, JR-1, RGM-1, and JA-1) (Table T11) and full procedural blanks were prepared as stock solutions and included with unknowns in each ICP-AES run. Standard stock solutions prepared at the final dilution factor for ICP analysis (5000:1) can last several weeks without deterioration (Coggon et al., 2024). Reference materials (BHVO-2, BCR-2, and BRR-1) were measured as check standards during each run to quantify instrument drift (Table T12). Elemental concentrations for reference materials are given in Imai et al. (1995) and Jochum et al. (2016); basalt samples and standard reference materials were not combusted prior to ICP-AES measurements because this approach may cause inconsistent results during standardization (Jochum et al., 2016).

Samples were fused in Pt-Au (95:5) crucibles for ~ 12 min at 1250°C in an internally rotating induction furnace (Bead Sampler NT-2100). After cooling, beads were transferred to 125 mL HDPE bottles and dissolved in 50 mL 10% HNO_3 , which was aided by shaking with a Burrell wrist-action bottle shaker for 1 h. Next, 0.5 mL of each solution was diluted with 4.4 mL of 10 wt% trace metal-grade HNO_3 and 0.1 mL of an internal standard solution containing Be, In (100 $\mu\text{g/g}$), and Sb (200 $\mu\text{g/g}$). The final dilution factor for the samples is $\sim 5000:1$. Check standards and drift and blank samples are measured 4–5 times through the course of each run. Each solution is analyzed 3 times,

and each analysis is reported as an average. The optical wavelengths that produced the best calibration curves, as defined by their correlation coefficients (*r* values), were used to calculate solution concentrations. For all major elements except potassium, multiple wavelengths per element had *r* values of 0.999X and were 10× above instrument detection limits in their linear dynamic ranges. Results from all such wavelengths, in many cases both axially and radially measured by the instrument, were used to calculate solution concentrations.

Table T11. Sediment and basalt ICP-AES standards and accepted values, Expeditions 395 and 395C. [Download table in CSV format.](#)

	Al ₂ O ₃ (%)	Ba (ppm)	CaO (%)	Co (ppm)	Cr (ppm)	Cu (ppm)	Fe ₂ O ₃ (%)	K ₂ O (%)	MgO (%)	MnO (%)	Na ₂ O (%)	Ni (ppm)	P ₂ O ₅ (%)	S (ppm)	Sc (ppm)	SiO ₂ (%)	Sr (ppm)	TiO ₂ (%)	V (ppm)	Y (ppm)	Zn (ppm)	Zr (ppm)	
AGV-1	17.15	1,226	4.94	15.3	10.1	60	6.77	2.92	1.53	0.09	4.26	16	0.49		12.2	58.84	662	1.05	121	20	88	227	
BCR-2	13.64	683	6.97	42	18	19	13.43	1.72	3.42	0.175	3.25	12	0.35		32.6	54.1	346	2.26	416	37	127	188	
BHVO-2	13.5	130	11.4	45	280	127	12.3	0.43	7.23		2.22	119	0.27		31.8	49.9	389	2.73	317	26	103	172	
BIR-1	15.35	7.7	13.24	51.4	382	126	11.26	0.027	9.68	0.171	1.75	166	0.046		44	47.77	108	0.96	313	16	71	22	
BRR-1	14.41	6.85	11.665				12.175	0.06	8.77	0.205	2.08		0.14		43.98	48.91	69	0.985		27.71		55.22	
GSP-2	14.9	1,340	2.1	7.3	20	43	4.9	5.38	0.96		2.78	17	0.29		6.3	66.6	240	0.66	52	28	120	550	
HISS-1	1.38		1.6	0.65	30	2.29	0.352	0.4	0.124	0.009	0.503	2.16				94.12	96.9	0.127	6.8			4.94	
JB-1b	14.38	397.4	9.6	27.76	352	117.7	9.02	1.32	8.14	0.147	2.63	75.4	0.256		25.9	51.11	119.7	1.23	357.6			485.3	
JB-2	14.64		9.82	38	28.1	225	14.25	0.42	4.62	0.218		16.6	0.101	17.9	53.5	53.25	178	1.19	575	24.9	108	51.2	
JB-2a	14.67	219	9.79	40	28	274	14.18	0.41	4.58	0.214	2.03	14.5	0.095			53.22	179	1.18	574	25.4	109	61.8	
JB-3	17.2		9.79	34.3	58.1	194	11.82	0.78	5.19	0.177		36.2	0.294	9.86	33.8	50.96	403	1.44	372	26.9	100	97.8	
JGB-1	17.49	64.3	11.9	60.1	57.8	85.7	15.06	0.24	7.85	0.189	1.2	25.4	0.056	1,910	35.8	43.66	327	1.6	635	10.4	109	32.8	
LKSD-1	7.8	430	10.8	11	31	44	4.11	1.1	1.7	0.1	2	16	0.2	15,700	9	40.1	250	0.5	50	19	331	134	
MESS-4	14.95	920	1.83	13	94.3	32.9	5.42	2.87	2.62	0.038	1.7	42.8	0.238	1,580	13.4	59.47	132	0.641	216	20	147	96	
NBS-1C	1.3	84	50.3	1.15	19		0.55	0.28	0.42	0.025	0.02		0.04		1.3	6.83	250	0.07				17.8	
NBS-99A	20.41	2,330	2.14				0.064	5.18	0.02		6.2		0.02			65.04		0.007					
PACS-3	12.43		2.64	12.1	90.6	326	5.87	1.51	2.32	0.056	4.74	39.5	0.215	11,700		55.83	267	0.737	129			376	
SCO-1	13.67	570	2.62	10.5	68	28.7	5.14	2.77	2.72	0.053	0.9	27	0.206			62.78	174	0.628	131	26	103	160	
SDC-1	15.8	630	1.4	18	64	30	6.32	3.28	1.69		2.05	38	0.16		17	65.8	180	1.01	102		103	290	
SDO-1	12.27	397	1.05	46.8	66.4	60.2	9.34	3.35	1.54	0.042	0.38	99.5	0.11		13.2	49.28	75.1	0.71	160	40.6	64.1	165	
SO-1	17.59	870	2.46	29	170	61		3.18	3.83	0.11	2.7	92	0.15		17.7	54.98	331	0.87	133	24.5	144	84	
STSD-2	16.1	540	4	19	116	47	7.5	2.1	3.1	0.1	1.7	53	0.3	600	16	53.7	400	0.8	101	37	246	185	
W-2	15.35	182	10.87	44	93	103	10.74	0.627	6.37	0.163	2.14	70	0.131		35	52.44	194	1.06	262	24	77	94	

Table T12. Reproducibility of major oxides and minor elements in ICP-AES check standards, Expeditions 395 and 395C. — = not applicable. [Download table in CSV format.](#)

	BHVO-2				BCR-2				BRR-1				BIR-1						
	Accepted	Exp 395	σ	Exp 395C	σ	Accepted	Exp 395	σ	Exp 395C	σ	Accepted	Exp 395	σ	Exp 395C	σ	Accepted	Exp 395	Exp 395C	σ
Major oxide elements (wt%):																			
SiO	49.60	48.81	0.75	39.66	3.52	54.10	53.18	0.62	54.00	—	48.91	49.56	0.48	50.27	0.84	47.77	—	40.98	2.66
TiO	2.73	2.77	0.03	2.73	0.03	2.26	2.27	0.02	2.27	—	0.99	1.03	0.02	1.04	0.03	0.96	—	0.97	0.01
Al	13.44	13.38	0.12	13.56	0.09	13.50	13.42	0.17	13.48	—	14.41	14.55	0.11	14.70	0.12	15.35	—	15.82	0.13
Fe	12.39	12.02	0.24	12.40	0.19	13.80	13.45	0.06	13.77	—	12.18	11.82	0.28	12.07	0.09	11.26	—	11.61	0.17
MnO	0.17	0.16	0.00	0.17	0.00	0.24	0.19	0.01	0.20	—	0.21	0.18	3.40	0.19	0.17	—	0.17	0.00	
MgO	7.26	7.01	0.16	7.18	0.08	3.59	3.52	0.07	3.60	—	8.77	8.42	0.24	8.74	0.09	9.68	—	9.56	0.10
CaO	11.40	11.17	0.17	11.40	0.11	7.12	7.03	0.05	7.11	—	11.67	11.80	0.11	11.95	0.19	13.24	—	13.40	0.15
Na	2.22	2.16	0.04	2.21	0.02	3.16	3.22	0.08	3.12	—	2.08	1.97	0.07	2.01	0.05	1.75	—	1.83	0.02
K	0.51	0.49	0.04	0.53	0.01	1.79	1.73	0.01	1.77	—	0.06	0.05	0.01	0.06	0.00	0.03	—	0.03	0.00
P	0.27	0.26	0.01	0.28	0.00	0.35	0.35	0.01	0.36	—	0.14	0.08	0.00	0.09	0.03	0.05	—	0.03	0.01
Sum	99.99	98.21	—	90.11	—	99.91	98.35	—	99.68	—	99.40	99.47	—	101.11	—	100.25	—	94.41	—
Minor elements (μg/g):																			
Sc	31.80	31.24	0.45	31.58	0.30	33.00	32.68	0.13	33.53	—	43.98	43.15	0.57	44.09	0.30	44.00	—	44.04	0.46
V	318	311.93	3.89	315	4	416	400.66	3.10	418	—	—	305.34	3.00	313	4	313	—	319	4
Cr	287	275.85	4.51	—	—	18	18.09	1.67	—	—	—	358.00	3.11	—	—	382	—	—	—
Ni	120	115.69	5.89	111	6	20	14.71	3.68	13	—	—	119.20	3.30	126	3	166	—	168	4
Zn	104	97.39	3.89	114	10	130	127.85	0.90	130	—	—	78.91	1.33	86	3	71	—	99	8
Rb	9.3	—	—	—	—	46.0	—	—	—	—	—	—	—	—	—	0.3	—	—	—
Sr	394	388.02	4.24	389	3	346	339.90	5.29	337	—	69	69.64	0.52	70	1	108	—	108	1
Y	25.9	26.40	0.38	26.1	0.4	37.0	36.32	0.23	36.1	—	27.7	27.57	0.66	27.6	0.5	16.0	—	16.4	0.6
Zr	171	169.86	1.75	161	3	188	185.87	1.58	187	—	55	56.63	1.20	57	2	16	—	15	1
Ba	131	132.56	2.29	133	1	683	688.72	7.11	684	—	7	7.37	0.34	7	1	7	—	7	0
<i>n</i>		4		10				4	1			5		4			0	10	

Analytical reproducibility on the ICP-AES for basalt analysis is a function of both the measurement precision of the chosen wavelengths (typical uncertainties are <1% to 2%) and the number of wavelengths calibrated for each element because each measured wavelength is an independent abundance determination. For the higher abundance major elements (Si, Al, Fe, Mg, and Ca), all of which are measured axially and/or radially on multiple wavelengths, precision was between $\pm 0.6\%$ and $\pm 1.1\%$, whereas the lower abundance major species (Na, K, Ti, and Mn) range $+0.7\%$ to $+1.9\%$ (ICP-AES; Table T13).

9.4.5. Basalt analysis using portable X-ray fluorescence spectrometer

An onboard handheld pXRF was used to quickly assess downhole compositional changes in recovered basalt. During Expedition 395 and 395C, pXRF was used to conduct qualitative geochemical assessments of basalt samples in the core through direct measurements on fresh-cut rock surfaces. Although the pXRF data were used to broadly identify cursory basalt geochemistry, these should be regarded as qualitative.

During Expedition 395C, shipboard XRF measurements were made with the Olympus Delta Premium DP-6000 Handheld XRF analyzer. During Expedition 395, a Bruker Tracer 5g Handheld XRF analyzer was used. These instruments are self-contained energy-dispersive XRF survey tools that include data correction packages tailored to a variety of applications (e.g., metals, plastics, soils and minerals, and consumer goods). Instrumental data correction methods combine Compton normalization strategies (specific to lower-Z elements) and fundamental parameters (FP)

Table T13. Precision and detection limits for ICP-AES basalt and sediment analysis, Expedition 395. * = Calculated as $3\times$ standard deviation of the blank. † = Based on replicate analyses of unknowns. (A) = axial, (R) = radial, (B) = both. [Download table in CSV format.](#)

Element (unit)	Wavelengths used (nm)	In-rock detection limit*	Precision (%) [†]
Al ₂ O ₃ (wt%)	308.215 (B)		
	396.152 (B)	0.19	0.59
Ba (ppm)	455.403 (B)	0.29	1.1
CaO (wt%)	315.887 (A)		
	317.933 (B)	0.12	0.78
	318.127 (A)		
Cr (ppm)	431.865 (B)		
	267.716 (A)	1	0.75
	327.395 (A)	2.5	1.2
Fe ₂ O ₃ (wt%)	238.204 (B)	0.005	1.1
	239.563 (A)		
	258.588 (B)		
K ₂ O (wt%)	259.940 (B)		
	766.491 (A)	0.001	0.73
	202.582 (A)		
MgO (wt%)	277.983 (B)		
	279.078 (B)	0.015	1.1
	280.270 (A)		
MnO (wt%)	257.610 (B)	0.002	0.89
Na ₂ O (wt%)	588.995 (A)		
	589.592 (B)	0.004	1.9
Ni (ppm)	231.604 (A)	8.3	1.9
P ₂ O ₅ (wt%)	213.618 (A)	0.021	5.2
Sc (ppm)	361.383 (A)	0.54	0.92
	424.682 (A)		
SiO ₂ (wt%)	251.611 (B)		
	288.158 (B)	0.024	0.84
Sr (ppm)	407.771 (B)		
	421.552 (B)	0.48	2.7
TiO ₂ (wt%)	334.941 (B)	<0.001	1.4
V (ppm)	368.520 (B)		
	292.401 (R)	9.1	1.1
Y (ppm)	326.769 (A)		
	371.029 (A)	0.54	0.64
Zn (ppm)	213.857 (A)	2.6	2.7
Zr (ppm)	327.307 (A)	9.4	2.2
	343.823 (A)		

methodologies, which solve a series of nonlinear equations for each analyzed element. The parameters used in the FP equations comprise metrics for the X-ray source, fluorescence intensities, absorption coefficients, and absorption edge effects for each wavelength analyzed, together with parameters for sample geometry (e.g., van Sprang, 2000).

Both the Olympus and Bruker pXRF instruments include geologic materials correction protocols: the Geochem analysis protocol on the Olympus instrument and the GeoExploration protocol on the Bruker instrument. These protocols, which include both FP and Compton normalization correction, optimize analysis for many higher atomic number species, as well as a number of key lower atomic weight elements. Many of the elements determined using pXRF basalts (Cd, Sb, As, Hg, W, Mo, Bi, Ag, Sn, Se, Pb, Th, and U) commonly occur at levels below the in-rock detection limits for these instruments, and a few (in particular V, Sc, and Ba) suffer from spectral interference problems that preclude reliable analysis at the levels likely to be encountered in common igneous rocks or marine sediments. Elements with low atomic numbers (Na, Mg, Si, and Al) are poor at generating X-rays and produce only low-energy, readily absorbed X-rays. Consequently, even though these species are high in abundance, their X-ray yields are poor and nonlinearly related to concentration. As such, pXRF is analytically useful for a subset of elements whose abundances are high enough for detection, and which produce X-rays that are sufficiently energetic for quantifiable analysis. This list of elements varies somewhat with rock type, but commonly includes K, Ca, Ti, V, Cr, Mn, Fe, Ni, Zn, Cu, Rb, Sr, Y, and Zr. Depending on the homogeneity of the sample material, purpose of the analysis, and time available, one or more measurements were made for each sample. Where multiple measurements were taken, these were averaged to provide a single sample analysis. Two powdered standard reference materials (BHVO-2 and BCR-2) were analyzed with each set of unknowns to track daily machine performance, which is consistent with past practice (e.g., Ryan et al. 2017; Johnston et al., 2018).

During Expeditions 395C and 395, pXRF measurements were made on the archive halves of the cores. The pXRF instrument was secured with a custom stand that minimized movement during each analysis and allowed for precise determination of the instrument position on the core section. An 8 mm spot size was used to integrate any small-scale heterogeneities in the basalt.

During Expedition 395, the GeoExploration Protocol with the Oxide 3-phase instrumental method was used following guidance provided from shore-based testing of the Bruker pXRF system at the GCR. As was noted during previous IODP expeditions, concentrations obtained using only the instrument's correction protocols do not align with recognized values for standard reference materials. TiO_2 was commonly 8%–10% low relative to accepted values, whereas K_2O was generally within a few percent of reference sample values. Most major oxide concentrations (e.g., SiO_2 , MgO , and Al_2O_3) were generally low relative to accepted values and varied considerably from run to run. More elements were accessible using the Bruker pXRF relative to the Olympus, a number of which are potentially useful in examining the sourcing of recovered basalts (Ti, Zr, Y, V, Zn, and Cu) and the potential extent of hydrothermal alteration (K, Ca, Sr, and Rb). When possible, the pXRF measurements were conducted on unaltered basalt; however, because of the near-pervasive alteration at Site U1564, it was not always possible to identify unaltered material.

9.5. Shore-based X-ray fluorescence scanning

Three different intervals totaling approximately 265 m of core from Expedition 395C were XRF scanned at the GCR using a fourth-generation Avaatech core scanner (Table T14).

Core sections were removed from the refrigerator and equilibrated to room temperature. Each section was lightly scraped with a clean glass slide to provide a fresh, flat surface, and clasts were removed. Plastic end caps were cut below the level of the sediment to allow the detector prism to land flush on the sediment. Each section was covered with a 4 μm thick layer of Ultralene plastic foil to provide a barrier between the sediment and the prism.

Each section was scanned at 2 cm intervals using three energies (10, 30, and 50 kV). Following standard IODP procedure, the measured area was 10 mm downcore and 12 mm across the core. No filter was used for the 6 s, 10 kV, 0.16 mA measurements. A thick palladium filter was used for

Table T14. Shore-based XRF scanning methods, Expedition 395C. [Download table in CSV format.](#)

Hole	Interval CSF-A (m)	10 kV	30 kV	50 kV
395C-				
U1554E	5H-1 to 15H-7 (94.82–199.54)	X	X	X
U1554F	3R-1 to 5R-2 (620.04–641.5)	X	X	X
U1563A	1H-1 (0–1.5) 10H-6 (90.95–92.44) 19H-7 to 45F-4 (178.03–310.02)	X	X	X

the 6 s, 30 kV (1.25 mA) measurements, and a copper filter was used for the 10 s, 50 kV (0.75 mA) measurements. Intervals disturbed by coring were not scanned.

The raw spectra of counts per channel were converted to elemental intensities using models created in the software program bAxil and batch processed using the software bAxilBatch. Data were examined, and counts with positive argon values (indicating a poor contact with the sediment or very low total counts) were removed.

9.6. Microbiological sample collection

Sediment samples were collected for shore-based microbiological (MBIO) analyses. Microbiological samples were collected from the top of Section 3 in each core during Expeditions 395C and 395 (i.e., at the same frequency as IW samples). Approximately 5 mL of sediment was sampled with an autoclaved, cut-end 5 mL syringe from the section of core adjacent to the core sampled for IW analyses. For sediments in harder intervals at deeper depth, an additional 2 cm whole-round sample was taken next to the IW sample and aseptically sampled for microbiological analyses. This sediment was split into a 1 mL sample mixed with 5 mL artificial seawater and 600 μ L 10 \times cryoprotectant glycerol-TE (glyTE), and the remaining \sim 4 mL of sediment was left in the syringe. Approximately 0.1 g of sediment was also mixed with 0.9 mL artificial seawater and 1 μ L of Redox-Sensor Green (ThermoFisher) and incubated under anoxic conditions for 30 min with shaking before 100 μ L of glyTE was mixed in. All sediment samples were flash frozen with liquid nitrogen and stored at -80°C before shipment to shore-based laboratories. Hard rock samples from Expedition 395C (Holes U1554F, U1555H, U1555I, U1562A, U1562B, and U1563B) were selected immediately after cores were shaken onto ethanol-sterilized half liners and placed into a sterile sample bag before being stored at -80°C before shipment to shore-based laboratories. For Expedition 395 (Hole U1564F), whole-round hard rock samples were further processed before freezing. After selection, samples were rinsed in 0.2 μ m filtered 70% ethanol twice, followed by a 100% ethanol rinse and then drying in a flame-sterilized metal box on a clean bench equipped with a tabletop air filtration unit (KOACH T 500-F, Koken Ltd., Japan). Pristine pieces of inner hard rock samples were chipped with a flame-sterilized chisel to remove the exteriors of core samples that came into contact with drilling fluid (approximately 10–20 cm^3). A sample (\sim 1 cm^3) of each whole round was then crushed and processed following the sediment split sample protocols outlined above, and all pieces of hard rock processed for microbiological analyses were flash frozen in liquid nitrogen before being stored at -80°C prior to shipment to shore-based laboratories.

10. Downhole measurements

Downhole measurements were used to estimate the in situ physical, chemical, and structural properties of the formations penetrated by boreholes and can provide stratigraphic, lithologic, mineralogical, and geochemical insights into the drilled sequence of rocks. Downhole measurements can include wireline logging data, which provide a variety of continuous formation measurements with depth, or spot-depth measurement logs such as formation temperature logging and vertical seismic imaging. Collectively, this provides information on formation properties at a scale between that of geophysical surveys and laboratory measurements from core material. Accordingly, wireline logging data are useful for calibration and interpretation of geophysical survey data (e.g., downhole seismic velocity measurements), and they provide data for the integrated

understanding of physical properties and seismic information and the in situ conditions of recovered core samples. These data can also provide a complementary data set to be jointly interpreted alongside core measurements, including filling gaps where core recovery is incomplete.

The suite of downhole measurements collected in holes drilled as part of Expeditions 384, 395C, and 395 are detailed in Table T15.

10.1. Wireline logging

During wireline logging operations, up to four Schlumberger tool strings were deployed after completion of coring operations (Figure F16; Table T15). Logging data were recorded as the tool string was lowered and raised in the borehole (downlogs and uplogs, respectively) on a seven-conductor wireline cable that moves the string at various constant speeds, typically 250–550 m/h, depending on logistical constraints. During Expeditions 384, 395C, and 395, four different tool strings were deployed. The triple combo tool string included five tools: the Magnetic Susceptibility Sonde (MSS), High-Resolution Laterolog Array (HRLA), Accelerator Porosity Sonde (APS), Hostile Environment Litho-Density Sonde (HLDS), and Hostile Environment Natural Gamma Ray Sonde (HNGS). The FMS-sonic tool string included four tools: the FMS, Dipole Sonic Imager (DSI), General Purpose Inclinometry Tool (GPIT), and HNGS. The UBI tool string included the UBI, GPIT, and HNGS. The VSI tool string included two tools: the VSI and HNGS. All four tool strings were equipped with the HNGS to allow correlation between different tool strings and logging runs. Given the configuration of the tool strings, only the tool at the very bottom of the string reaches the bottom of the hole, leading to offsets in the greatest depth measured between the tools on the individual tool string.

The triple combo tool string measured formation MS, resistivity (shallow, medium, and deep into the formation), porosity, density, NGR (referred to as gamma log in Downhole measurements in the site chapters), and spectral gamma radiation (K, Th, and U). The FMS-sonic tool string provided a microresistivity borehole image, formation (V_p) and shear wave velocity (V_s), borehole orientation (deviation and horizontal azimuth), formation gamma log, and spectral gamma radiation. The UBI tool string collected an acoustic borehole image, measured borehole orientation (deviation and horizontal azimuth), collected a formation gamma log, and measured spectral gamma radiation. The VSI tool string acts as a receiver for acoustic energy generated by a seismic source deployed from the vessel, and the attached HNGS provides formation gamma log counts and spectral gamma radiation counts.

Each tool string contained an Enhanced Digital Telemetry Cartridge (EDTC) (Figure F16), which combines a high-speed telemetry downhole modem with a scintillation gamma ray detector. The EDTC provided high-speed (>1 Mbps) communication between the borehole tools in the hole and the Schlumberger multi-tasking acquisition and imaging system (MAXIS) aboard *JOIDES Resolution*. The gamma ray detector provided a total formation gamma radiation count, which can be correlated with similar measurements made using the HNGS in other tool strings. Additionally, the EDTC contained a single-axis accelerometer that recorded Z-axis acceleration, which can be used to measure downhole tool motion and assist with speed corrections on wireline logs in postacquisition data processing. During wireline logging operations, incoming data were recorded and monitored in real time on the MAXIS logging computer by the Schlumberger logging engineer aboard *JOIDES Resolution*, during which initial processing of data was performed. Once logging operations concluded on site, acquired data were sent to the LDEO-BRG for further processing. General wireline logging operations, processing, and quality control methods are discussed here; however, selected additional details and notes are given in the site chapters because processing methods varied between Expeditions 384, 395C, and 395.

Prior to downhole logging, the holes underwent various preparation procedures, documented in detail in Operations in the site chapters. Procedures included wiper trips to clear the hole, flushing debris from the hole by circulating high-viscosity mud and then filling it with a seawater-based logging gel (e.g., sepiolite mud mixed with seawater and weighted with barite) to stabilize the borehole walls, and flushing mud from the hole with seawater prior to a UBI tool string pass.

Table T15. Downhole logging, Expeditions 384, 395C, 395. NA = not available. [Download table in CSV format.](#)

Hole	Tool string	Logging pass	From depth WSF (m)	To depth WSF (m)	Pipe depth WSF (m)	Notes
384-						
U1555G	MSS-B/HRLA/APS/HLDS/HNGS	Downlog	0	258	203	Caliper closed
	MSS-B/HRLA/APS/HLDS/HNGS	Repeat (uplog)	254.5	308	203	Recorded open hole
	MSS-B/HRLA/APS/HLDS/HNGS	Main (uplog)	0	297	203	
	FMS/DSI/GPIT/HNGS	Downlog	0	297	203	Caliper closed
	FMS/DSI/GPIT/HNGS	Repeat	251	297	203	Reference pass
	FMS/DSI/GPIT/HNGS	Main	0	297	203	
	VSI/HNGS	NA	235.1	295.6	203	2 stations acquired, 10 shots at each station
395C-						
U1555H	Formation Temperature	NA	24	119		4 measurements (Cores 4H, 7H, 10H, and 13H)
U1555I	MSS-B/HRLA/APS/HLDS/HNGS	Downlog	0	371	85	Reference pass, caliper closed
	MSS-B/HRLA/APS/HLDS/HNGS	Uplog	220	371	85	Tool stuck
U1563A	Formation Temperature	NA	35.9	121.4		4 measurements (Cores 4H, 7H, 10H, and 13H)
U1563B	MSS-B/HRLA/APS/HLDS/HNGS	Downlog	0	277	~85.5	Caliper closed
	MSS-B/HRLA/APS/HLDS/HNGS	Repeat (uplog)	170	314	~85.5	Recorded open hole
	MSS-B/HRLA/APS/HLDS/HNGS	Main (uplog)	0	316	~85.5	Reference pass
	VSI/HNGS	NA	69	122	~85.5	4 stations acquired
	FMS/DSI-2/GPIT/HNGS	Downlog	0	277	~85.5	Caliper closed
	FMS/DSI-2/GPIT/HNGS	Repeat (uplog)	140	309	~85.5	Recorded open hole
	FMS/DSI-2/GPIT/HNGS	Main (uplog)	0	311	~85.5	
U1554E	MSS-B/HRLA/APS/HLDS/HNGS	Downlog	0	647	~70.7	Reference pass, caliper closed
	MSS-B/HRLA/APS/HLDS/HNGS	Repeat (uplog)	527	647	~70.7	Recorded open hole
	MSS-B/HRLA/APS/HLDS/HNGS	Main (uplog)	0	647	~62.8	
	FMS/DSI-2/GPIT/HNGS	Downlog	0	647	~72	Caliper closed
	FMS/DSI-2/GPIT/HNGS	Repeat (uplog)	122	647	~72	Recorded open hole
	FMS/DSI-2/GPIT/HNGS	Main (uplog)	0	647	~62	
	Formation Temperature	NA	66	161		4 measurements (Cores 2H, 5H, 8H, and 11H)
U1554F	MSS-B/HRLA/APS/HLDS/HNGS	Downlog	0	764	590	Casing at 603.5 m WSF, caliper closed
	MSS-B/HRLA/APS/HLDS/HNGS	Repeat (uplog)	655	781	590	Casing at 603.5 m WSF
	MSS-B/HRLA/APS/HLDS/HNGS	Main (uplog)	0	781	590	Casing at 603.5 m WSF, reference pass
	FMS/DSI-2/GPIT/HNGS	Downlog	0	782	590	Casing at 603.5 m WSF, caliper closed
	FMS/DSI-2/GPIT/HNGS	Repeat (uplog)	650.5	781	590	Casing at 603.5 m WSF, recorded open hole
	FMS/DSI-2/GPIT/HNGS	Main (uplog)	0	781	590	Casing at 603.5 m WSF
	UBI/GPIT/HNGS	Downlog	0	776	590	No image, casing at 603.5 m WSF
	UBI/GPIT/HNGS	Uplog	631	775	590	Recorded open hole, casing at 603.5 m WSF
	UBI/GPIT/HNGS	Uplog	586	775	590	Recorded open hole, casing at 603.5 m WSF
	UBI/GPIT/HNGS	Uplog	0	584	590	No image, casing at 603.5 m WSF
U1562A	Formation Temperature	NA	21	116		4 measurements (Cores 4H, 7H, 10H, and 13H)
U1562B	MSS-B/HRLA/APS/HLDS/HNGS	Downlog	0	559	86	Caliper closed
	MSS-B/HRLA/APS/HLDS/HNGS	Repeat (uplog)	136	559	86	
	MSS-B/HRLA/APS/HLDS/HNGS	Main (uplog)	0	560	86	Reference pass
	FMS/DSI-2/GPIT/HNGS	Downlog	0	485	86	Caliper closed
	FMS/DSI-2/GPIT/HNGS	Repeat (uplog)	419	558	86	
	FMS/DSI-2/GPIT/HNGS	Main (uplog)	0	558	86	
	VSI/HNGS	NA	81	113	86	4 stations acquired (420, 428.5, 459.4, and 556.1 m DSF)
	UBI/GPIT/HNGS	Uplog	408	553	86	No image
	UBI/GPIT/HNGS	Uplog	410	553	86	
	UBI/GPIT/HNGS	Uplog	0	407	86	
U1564C	MSS-B/HRLA/APS/HLDS/HNGS	Downlog	0	593	79	Caliper closed
	MSS-B/HRLA/APS/HLDS/HNGS	Repeat (uplog)	483	631	77.5	Recorded open hole
	MSS-B/HRLA/APS/HLDS/HNGS	Main (uplog)	0	632	77.5	Reference pass
	FMS/DSI-2/GPIT/HNGS	Downlog	0	596	79	Caliper closed
	FMS/DSI-2/GPIT/HNGS	Uplog	0	629	79	
	Formation Temperature	NA	26	140		5 measurements (Cores 4H, 7H, 10H, 13H, and 15H)/no data
395-						
U1554H	Formation Temperature	NA	37.9	147.1		5 measurements (Cores 4H, 7H, 10H, 13H, 16H)
U1564D	Formation Temperature	NA	38	123.5		4 measurements (Cores 4H, 7H, 10H, 13H)
U1564E	Formation Temperature	NA	34.3	119.8		4 measurements (Cores 4H, 7H, 10H, 13H)
U1564F	MSS-B/HRLA/APS/HLDS/HNGS	Downlog	0	1117.1	~60	MSS-B and APS malfunctioned; casing at 551 m WSF
	MSS-B/HRLA/APS/HLDS/HNGS	Repeat (uplog)	1057.2	1171.2	~60	Recorded open hole; MSS-B and APS malfunctioned; casing at 551 m WSF
	MSS-B/HRLA/APS/HLDS/HNGS	Main (uplog)	0	1170.6	~60	MSS-B and APS malfunctioned; casing at 551 m WSF
	FMS/DSI-2/GPIT/HNGS	Downlog	508	1116.2	~60	Caliper closed; DSI-2 damaged; casing at 551 m WSF
	FMS/DSI-2/GPIT/HNGS	Repeat (uplog)	539.5	1169.3	~60	DSI-2 damaged; casing at 551 m WSF
	FMS/DSI-2/GPIT/HNGS	Main (uplog)	528.3	1169.6	~60	DSI-2 damaged; casing at 551 m WSF
	UBI/GPIT/HNGS	Downlog	524.3	1165.6	~60	No image; casing at 551 m WSF
	UBI/GPIT/HNGS	Uplog	987.6	1164.4	~60	Recorded open hole; high resolution UBI images; casing at 551 m WSF
	UBI/GPIT/HNGS	Uplog	539.8	1163.9	~60	Low resolution UBI images; casing at 551 m WSF
U1602B	Formation Temperature	NA	33.7	119.2		4 measurements (Cores 4H, 7H, 10H, 13H)
U1602E	MSS-B/HRLA/APS/HLDS/HNGS	Downlog	31.7	1277.8	76	Caliper closed

10.1.1. Wireline-logged properties and tool measurement principles

The wireline-logged properties and the principles of the tools used to measure them are described below and detailed in Table T16. Detailed information on individual tools and their geologic applications may be found in Serra (1984, 1986, 1989), Schlumberger (1989, 1994), Rider (1996), Goldberg (1997), Lovell et al. (1998), Helm-Clark et al. (2004), and Ellis and Singer (2007). A complete list of acronyms for the Schlumberger wireline tools and the various measurements made by each of these tools can be found in Table T17 and at <https://www.apps.slb.com/cmd/index.aspx>.

10.1.1.1. Magnetic susceptibility

The MSS is a nonstandard wireline tool designed by the Lamont-Doherty Earth Observatory (LDEO). It measures the ease with which formations are magnetized when subjected to a magnetic field and is often related to the concentration and composition (size, shape, and mineralogy) of magnetic minerals (principally magnetite) in the formation. The MSS measures borehole MS at two vertical (i.e., depth) resolutions. The MSS incorporates a single-coil electric inductor sensor

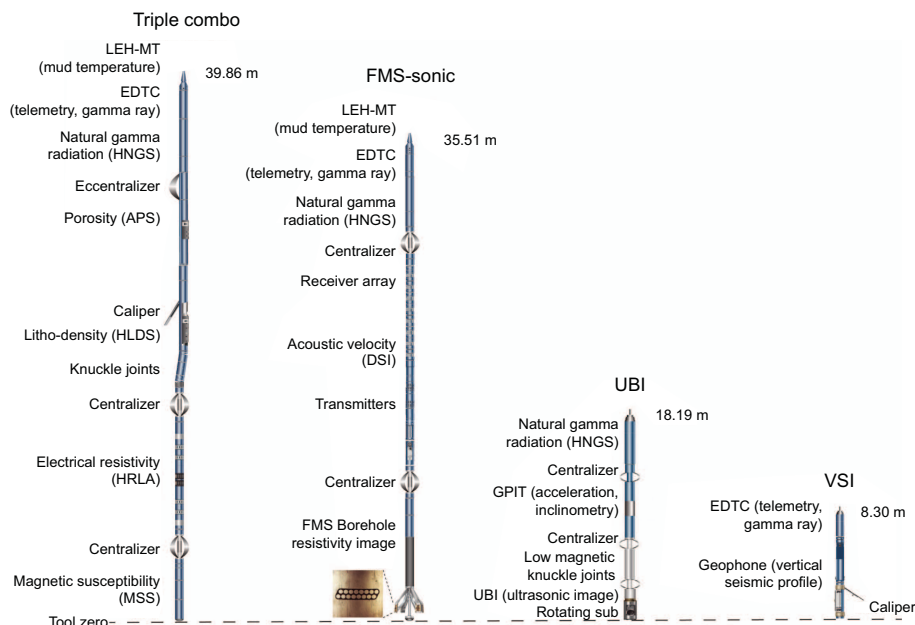


Figure F16. Wireline tool string diagrams, Expeditions 395C and 395. Tool combinations were modified at some sites based on operational conditions. Diagrams are not to scale. LEH-MT = logging equipment head-mud temperature tool.

Table T16. Downhole measurements, Expeditions 384, 395C, and 395. All tool and tool string names except MSS are trademarks of Schlumberger. NA = not applicable. [Download table in CSV format.](#)

Tool string	Tool	Measurement	Depth of investigation (cm)	Approximate vertical resolution (cm)
Triple combo	EDTC	Total gamma ray	61	30
	HNGS	Spectral gamma ray	24	51
	HLDS	Bulk density	15	38
	APS	Neutron porosity	18	36
	HRLA	Resistivity	127 (deepest, R5)	30
	MSS-DR	Magnetic susceptibility (deep reading)	20	40
FMS-sonic	EDTC	Total gamma ray	61	30
	HNGS	Spectral gamma ray	24	51
	DSI	Acoustic velocity	Variable	274
	GPIT	Tool orientation and acceleration	NA	NA
	FMS	Microresistivity	25	0.5
UBI	EDTC	Total gamma ray	61	30
	HNGS	Spectral gamma ray	24	51
	GPIT	Tool orientation and acceleration	NA	NA
	UBI	Acoustic images	Variable	0.50–2.0

that, when positioned against the borehole wall, is capable of measuring inductance as affected by the volume susceptibility of the formation over the volume of investigation. The sensor is pushed against the borehole wall using a bowspring that eccentricizes the tool. The coil is incorporated in a resonant circuit to produce a frequency that changes linearly with borehole susceptibility. This frequency is measured with the MSS microprocessor and converted into MS by applying scale and offset calibration constants. The MSS provided ~40 cm vertical resolution measurements with a ~20 cm depth of horizontal investigation. The MSS also contains a deep-reading sensor that employs three coils arranged coaxially along the length of the tool. This sensor provided a complimentary MS measurement that has a reduced sensitivity to the quality of the contact of the sensor with the borehole wall.

The MSS was run as the lowermost tool in the triple combo tool string using a specially developed data translation cartridge that enabled the MSS to be run in combination with Schlumberger wireline tools.

MSS data were plotted as uncalibrated instrument units on linear grids in 10^{-5} SI units. MSS measurements can be affected by temperature (higher temperatures lead to higher MS) and borehole size and shape (borehole sizes larger than 9 $\frac{3}{8}$ inches or those experiencing washouts can lower MS measurements). For quality control and environmental correction of MSS data, the tool also measured internal tool temperature, Z-axis acceleration, and low-resolution borehole conductivity.

Table T17. Acronyms and units used for downhole wireline tools and measurement, Expeditions 384, 395C, and 395. [Download table in CSV format.](#)

Tool	Output	Description	Unit
EDTC		Enhanced Digital Telemetry Cartridge	
	GR	Total gamma ray	gAPI
	ECGR	Environmentally corrected gamma ray	gAPI
	EHGR	High-resolution environmentally corrected gamma ray	gAPI
HNGS		Hostile Environment Natural Gamma Ray Sonde	
	HSGR	Standard (total) gamma ray	gAPI
	HCGR	Computed gamma ray (HSGR minus uranium contribution)	gAPI
	HFK	Potassium	wt%
	HTHO	Thorium	ppm
	HURA	Uranium	ppm
APS		Accelerator Porosity Sonde	
	APLC	Near/array limestone corrected porosity	Dec. fraction
	STOF	Computed standoff	Inch
	SIGF	Formation capture cross section	Capture units
HLDS		Hostile Environment Litho-Density Sonde	
	RHOM	Bulk density	g/cm ³
	PEFL	Photoelectric effect	barn/e ⁻
	LCAL	Caliper (measure of borehole diameter)	Inch
	DRH	Bulk density correction	g/cm ³
HRLA		High-Resolution Laterolog Array	
	RLA	Apparent resistivity from computed focusing mode	Ω m
	RT_HRLT	True resistivity	Ω m
	RM_HRLT	Borehole fluid resistivity	Ω m
MSS		Magnetic Susceptibility Sonde	
	LSUS	Magnetic susceptibility, deep reading (DR)	Uncalibrated unit
FMS		Formation MicroScanner	
	C1, C2	Orthogonal hole diameters	Inch
	P1AZ	Pad 1 azimuth	Degree (°)
		Spatially oriented resistivity images of borehole wall	
GPIT		General Purpose Inclinometry Tool	
	DEVI	Hole deviation	Degree (°)
	HAZI	Hole azimuth	Degree (°)
	F_x, F_y, F_z	Earth's magnetic field (three orthogonal components)	Oersted
	A_x, A_y, A_z	Acceleration (three orthogonal components)	m/s ²
DSI		Dipole Sonic Imager	
	DTCO	Compressional wave slowness	μ /ft
	DTSM	Shear wave slowness	μ /ft
	DT1	Shear wave slowness, Lower dipole	μ /ft
	DT2	Shear wave slowness, Upper dipole	μ /ft
UBI		Ultrasonic Borehole Imager	
	HAZI	Borehole azimuth	Degree (°)
		Spatially oriented acoustic images of borehole wall	

10.1.1.2. Porosity

Formation porosity was measured with the APS. A neutron source allows epithermal neutron measurements to be made while shielding the detector. This setup allows determination of porosity values that are less influenced by environmental conditions such as hole size and shape and the salinity of the borehole fluid. The near-array ratio epithermal porosity is the primary porosity measurement generated by the tool. The tool's source-to-detector spacing is optimized to provide formation hydrogen index measurements that are free of formation matrix density effects. Five detectors in the tool provide information on porosity, gas detection, clay content, improved vertical resolution, and borehole corrections.

When measuring porosity in formations comprised of clay or hydrous alteration minerals, a correction to the porosity provided by the tool is required to account for the bound H₂O in these minerals. The tool needs to be eccentricized in the hole to acquire good quality readings, which was achieved through use of an in-line centralizer. Calipers were closed during all tool descents, which precludes the collection of porosity data during the down logging runs. Poor connection between the tool and the borehole wall can result in attenuation of the formation signal by the borehole fluid and generate overestimates of formation porosity. As borehole size increases, epithermal count rates from the formation become increasingly masked by the borehole signal. In fluid-filled holes, the fluid salinity (chlorine is a strong neutron absorber) and density (additives such as barite increase mud density) can yield lower porosity determinations. When acquiring data with the APS through drilling pipe, because iron is a strong neutron absorber, increased porosity determination can be expected.

10.1.1.3. Electrical resistivity

The HRLA provided six resistivity measurements with different depths of investigation (≤ 127 cm), including the borehole (mud) resistivity and five measurements of formation resistivity with increasing penetration into the formation. The tool sends a focused current into the formation and measures the intensity necessary to maintain a constant drop in voltage across a fixed interval, providing direct resistivity measurements. The array has one central (source) electrode and six electrodes above and below it that serve alternatively as focusing and returning current electrodes. By rapidly changing the roles of these electrodes, a simultaneous resistivity measurement at six penetration depths is achieved. The HRLA is designed to ensure that all signals are measured at exactly the same time and tool position to reduce the sensitivity to shoulder bed effects when crossing sharp boundaries of beds that are thinner than the electrode spacing. The HRLA is designed to eliminate the need for a surface reference electrode, thus improving formation resistivity evaluation compared to traditional dual induction tools and allowing a wide range of formation resistivities to be measured (e.g., in high-porosity sediments as well as in basalt). The HRLA needs to maintain good contact with the borehole wall for optimal results, so knuckle joints are used to centralize the tool. The HRLA, unlike traditional laterolog tools, is sensitive to both vertical and horizontal resistivity. As such, different depths of investigation resistivity measurements (shallow, medium, and deep) can allow identifying when formation resistivity anisotropy exists (assuming no invasion). The HRLA provides resistivity data at a vertical resolution of 30.48 cm.

10.1.1.4. Gamma log

The HNGS was used on all tool strings to measure natural radioactivity in the formation. The HNGS uses two bismuth-germanate scintillation detectors to measure the gamma log of a formation, measured in American Petroleum Institute gamma radiation units (gAPI). The HNGS also uses 256-window spectroscopy to resolve the obtained gamma spectrum into the three most common components of naturally occurring radiation: potassium (⁴⁰K), thorium (²³²Th), and uranium (²³⁸U). The high-energy part of the spectrum is divided into three energy windows, each covering a characteristic peak of the three radioactive components, and the concentration of each component is determined from the count rates in each window: K in weight percent and Th and U in ppm. The computation of the elemental abundances uses a least-squares method of extracting U, Th, and K elemental concentrations from the spectral measurements. The HNGS filters out gamma ray energies below 500 keV (using only the higher energy gamma rays), eliminating sensitivity to bentonite or KCl in the drilling mud and improving measurement accuracy. The HNGS also provides a measure of the uranium-free or computed gamma ray measured in gAPI. The HNGS provides data at a vertical resolution of 30.48 cm and has a depth of investigation of 61 cm.

The depth of investigation is affected by hole size, mud density, formation bulk density (denser formations display a slightly lower radioactivity) and the energy of the gamma rays (higher energy gamma rays can reach the tool detector from deeper within the formation). HNGS data are corrected for borehole diameter variations during acquisition with the MAXIS system, and other effects can be investigated using other wireline measurements such as caliper and density data.

The EDTC contains a sodium iodide scintillation gamma detector that measures the total natural gamma ray emissions of the formation. These gamma log measurements are similarly affected by borehole size, mud density, and formation bulk density, which should be considered when using this data for scientific interpretation. Both tools were operated while the tool string passed through the remaining drill-pipe in the hole, measuring a subdued data set. If the results of the uplog and downlog agree, quantitative interpretations can be made on that data set.

10.1.1.5. Density and photoelectric factor

Formation density was measured using the HLDS. The HLDS contains a cesium (^{137}Cs) gamma ray source (662 keV) and far- and near-gamma ray detectors mounted on a shielded skid or pad that is pressed against the borehole wall by a hydraulically activated decentralizing arm. Gamma rays emitted by the source undergo Compton scattering, by which gamma rays are scattered by electrons in the formation. The number of scattered gamma rays that reach the detectors is proportional to the density of electrons in the formation, which is in turn related to bulk density. The HLDS provided data at a vertical resolution of 38.1 cm, but the depth of investigation, reported to be in the range of tens of centimeters, is difficult to quantify. The density measured in the downlog runs is unreliable because it cannot be corrected for the borehole shape as the caliper arms are closed.

The HLDS also provides the photoelectric effect (PEF), a measure of the photoelectric absorption of low-energy gamma radiation. Photoelectric absorption of gamma rays occurs when their energy falls below 150 keV as a result of being repeatedly scattered by electrons in the formation. PEF is determined by comparing the counts from the far detector in the high-energy region, where only Compton scattering occurs, with those in the low-energy region, where count rates depend on both reactions. The far detector on the HLDS is used for this as it has a greater depth of investigation.

Good contact between the tool and borehole wall and the tool pad is essential to generate high-confidence data from the HLDS; poor contact results in underestimation of density values. Caliper measurements of the borehole were used to assess contact quality. Borehole shape impact on density measurements was automatically corrected during acquisition and is reported as a corrected bulk density log. In the deeper parts of the hole, the PEF log should be used with caution, especially in sections of borehole with washouts, because barium in the logging mud masks the signal despite a correction for the influence of such mud.

10.1.1.6. Borehole resistivity images

The FMS-sonic provided high-resolution, electrical resistivity-based images of the borehole walls. These images allowed the identification of a range of geologic and stress field related borehole wall features and measurements of their orientation, width, and relative resistive response. Data from such wireline logs can be used for a range of geologic applications from facies characterization to geomechanical analyses. The tool consists of four orthogonal imaging pads each containing 16 microelectrode buttons that are pressed against the borehole wall during logging. The electrodes are arranged in two diagonally offset rows of eight electrodes each. A focused current is emitted from the four pads into the formation, and current intensity variations are measured by the array of buttons on each of the pads at a sampling interval of 2.5 mm. The maximum extension of the caliper arms on which the pads are mounted is 40.6 cm. In holes or sections of holes with a diameter >40.6 cm, pad contact with the borehole wall will be inconsistent and FMS image quality may appear out of focus and too conductive. Irregular (rough) borehole walls will also adversely affect the images if contact with the wall is poor. Approximately 30% of the circumference of a borehole with a diameter of 25 cm was imaged during a single pass with the FMS. Multiple uplog and downlog passes with the tool were performed in an effort to capture greater circumference of

the borehole with the FMS image. The maximum depth of investigation for the FMS is 25 cm, and it has a vertical resolution of 5 mm.

Processing of the measurements recorded by the tool was performed onshore by the LDEO-BRG. FMS acquisition parameters and current intensity data collected by the buttons were quality controlled, and the latter were checked for consistency or deviations across buttons and across pads, as well as checked for dead buttons or pads. The FMS data analysis procedure used the deviation, hole azimuth, accelerometer, and magnetometer data from the GPIT to orient the images to magnetic north. Each of these data streams was quality controlled, and appropriate corrections were applied when possible, including corrections for magnetic declination during acquisition and using accelerometer and magnetometer X-Y plane crossplots to assess and adjust data for minor tool decentralization issues. Current intensity measurements, which reflect microresistivity variations in the formation, were transformed into high-resolution false-colored images of variable intensity. Speed corrections using accelerometer data from the GPIT were applied to the images to reduce image quality deterioration from any stick and pull events during logging or misalignment of button data to remove zigzag effects. A button correction was applied if dead buttons were present, which replaces a defective button trace with the adjacent good button trace. An EMEX voltage correction is applied when the current response is outside of the operating range to prevent reporting of false relative formation conductivity. A static normalization was performed on the images to improve the overall visual image quality, and a dynamic normalization (using a 2 m window) was performed on the images to highlight features in sections where resistivity anomalies were subdued relative to the overall resistivity range in the section. During all stages of the image log processing, the image was visually inspected for artifacts (Lofts and Bourke, 1999).

10.1.1.7. Acoustic velocity

The DSI measured the transit times between sonic transmitters and an array of eight receivers. Borehole formation velocities (V_p , V_s , and Stoneley slowness) can be measured using the DSI in a variety of manners depending on tool recording mode during acquisition. During Expeditions 384 and 395C, the DSI was operated in P and S monopole and upper and lower dipole modes, and during Expedition 395 it was operated in P and S monopole and upper and lower dipole modes with Stoneley mode added for Hole U1564F. In P and S monopole mode, the monopole transmitter is excited by a high-frequency pulse to measure V_p and V_s . In upper and lower dipole mode, the DSI measures V_s using firings from the upper and lower dipole transmitter, respectively. The DSI has a vertical resolution of 1 m at a 15.24 cm sampling interval and a 23 cm depth of investigation.

The DSI incorporates both monopole and crossed-dipole transmitters with an eight-station array of electronically configurable hydrophones for monopole and dipole reception. Low- and high-frequency acoustic pulses drive the monopole transducer for Stoneley wave excitation and V_s and V_p measurements, respectively. A low-frequency acoustic pulse drives each dipole transducer for the creation of shear waves. A low-frequency transducer option (capable of excitation <1 kHz) is used for large diameter holes or for acoustically slow formations and shear wave generation. The receiver section of the tool contained eight receiver stations spaced 15.24 cm apart and spanned 106.7 cm of the tool string. Each station contains hydrophone pairs, one oriented in line with the upper dipole transmitter and one in line with the lower dipole transmitter. Outputs from each pair are differenced for dipole reception and summed for monopole reception. The tool acquisition cartridge performs automatic gain control and digitizes eight separate waveforms from more than one firing and then transmits the signal uphole. Threshold detectors allow for detection of compressional first-motion and derivation of compressional slowness. The DSI dipole also allows for detection of V_s in soft and hard formations.

The direct velocity measurements are a combination of replicate measurements and therefore are free from the effects of formation damage, or enlarged borehole diameter (Schlumberger, 1989). Depths of investigation (i.e., into the borehole wall) depend on formation type and V_s and V_p slowness, the variable spacings between various transmitter and receiver pairs, and the wavelength and frequency of the acoustic pulse and whether it is a head wave or guided wave, all of which is dynamically modified for borehole and borehole fluid conditions during acquisition.

10.1.1.8. Tool inclinometry

During wireline logging, a three-axis accelerometer and a three-axis magnetometer in the GPIT recorded vertical and horizontal tool motion and magnetic field measurements. This information was then used to define the inclinometry of the tool in terms of deviation (DEVI; from vertical), hole azimuth (HAZI), and relative bearing (RB). These data were used to accurately define the tool system axis with respect to Earth's gravity and magnetic fields. Inclinometry data were used to determine the acceleration and orientation of the FMS-sonic and UBI tool strings, mainly for the purpose of producing borehole image logs oriented to magnetic north.

10.1.1.9. Borehole acoustic images

Acoustic images of the borehole wall were generated from measurements taken using the UBI. Acoustic-based images of the borehole wall allow the identification of a range of geologic and stress field related borehole wall features and measurements of their orientation, width, and relative acoustic response. Data from such wireline logs can be used for a range of geologic applications from facies characterization to geomechanical analyses.

The UBI features a high-resolution transducer, which emits ultrasonic pulses at a frequency of 500 kHz that are reflected by the borehole surface and then received by the same transducer, recording the amplitude and traveltime of the reflected signal. These acoustic pulses are sent out through the drilling fluid in the borehole to interact with borehole wall formation. These acoustic waves are attenuated to various degrees based on a combination of (1) the reflection coefficient of the borehole fluid/borehole wall interface, (2) the lithology of the borehole wall, and (3) the morphology of the borehole wall. The nonattenuated part of the acoustic pulse is reflected back to the tool, where it is received by the same transducer, and this returned signal is used to generate images of the borehole wall. Two images were generated: an image that displays variations in returning amplitude of the acoustic wave and an image that displays variations in acoustic pulse two-way traveltime around the borehole. Traveltime data were also converted into a measure of borehole radius using the velocity of the acoustic pulse on the borehole fluid (provided as slowness) and the tool radius (4.285 cm). As with the resistivity image logs, the acoustic image log processing sequence used inclinometry data from the GPIT to orient images to true magnetic north. The continuous rotation of the transducer as it logs the borehole produces a 360° image of the inside of the borehole wall.

Processing of acoustic image log data was performed onshore by the LDEO-BRG. The UBI processing sequence used the deviation, hole azimuth, accelerometer, and magnetometer data from the GPIT to orient the images to magnetic north; these data were quality controlled, and appropriate corrections were applied when possible. Corrections included those for magnetic declination during acquisition and the use of accelerometer and magnetometer X-Y plane crossplots to assess and adjust data for minor tool decentralization issues. Speed corrections using accelerometer data from the GPIT were performed on the images to reduce image quality deterioration from stick and pull events during logging. When the UBI is eccentric in the borehole, the amplitude response is increased in the directions where the distance to the borehole wall is decreased and vice versa. Similarly, the traveltime will be reduced in directions where the tool is closer to the borehole wall. An eccentricity correction was applied to correct for both these issues; for amplitude, the correction removed low-order angular harmonic components of the signal with a periodicity equal to 1.5 revolutions. For traveltime image data, defects from eccentricity such as early picks and missing data were corrected using circular to elliptical models for the borehole or the casing and the eccentricity radius and orientation were used to correct for image distortion. The distance and direction of points on the borehole wall are initially given with the tool axis as the origin. A radius eccentricity correction procedure calculated the geometrical center of the points on the borehole wall, and the distance to those points was recalculated relative to the geometrical borehole center. Both corrected (XRAD) and uncorrected (RAD) radius images were provided as outputs. An azimuth equalization process removes preferential borehole enlargements at particular borehole azimuths, due to keyseat effects for example, by using the background response for all azimuths over a 3 m window. A static normalization was performed on the amplitude images to improve the overall visual image quality, and a dynamic normalization (using a 1 m long window) was performed on the amplitude images to highlight features in sections of the hole where amplitude anomalies were relatively subdued relative to the overall amplitude range in the section. During

each stage of the image log processing, the image was visually inspected for artifacts (Lofts and Bourke, 1999).

10.1.1.10. Vertical seismic profiles

During vertical seismic profile (VSP) experiments, the borehole VSI was anchored against the borehole wall at multiple stations to record the full waveform of elastic waves generated by a seismic source positioned just below the sea surface. These check-shot measurements relate depth in the hole to traveltimes in seismic reflection profiles and the depth of the stations was chosen according to the depth of interesting reflectors in the seismic profile. The VSI used during Expedition 395C contained a three-axis geophone that was anchored against the borehole wall at specified depths, with 5–10 air gun shots typically taken at each station. To minimize the impact on marine mammals, protected species observation protocols were followed during data collection. During Expedition 395C, the presence of whales in the exclusion zone prevented VSI operations in Holes U1554F and U1564C. VSPs were performed at four depths in Hole U1562B (Table T15). The seismic source was deployed 38 m from the moonpool (yielding a borehole offset of ~47 m) and 7–9 m below the sea surface using the aft port crane. When no protected species were observed, a soft ramp-up of the gun was performed to a maximum pressure of 2000 psi. The seismic source consisted of two 250-inch Sercel G III air guns in a parallel cluster spaced 1 m apart and fired at 2000 psi. All processing, including first arrival picking and stacking, was performed by the Schlumberger logging engineer during Expedition 395C. The data were then converted into SEG-Y format by the LDEO-BRG using code developed in-house. Stacks were generally calculated with at least nine good traces, and all the data in the SEG-Y format files were sorted into shot gathers. Because of frequent whale activity, time constraints, and washed out boreholes, no VSP data were collected during Expedition 395.

10.2. Formation temperature measurements

At all Expedition 395C and 395 sites, in situ formation temperature measurements were made at selected depths in the sediments to assess the thermal structure of the upper sedimentary section and to measure regional heat flow.

The APCT-3 tool fits directly into a modified coring shoe of the APC system and consists of a battery pack, a data logger, and a platinum resistance-temperature device calibrated over a temperature range of 0°–30°C. Before entering the borehole, the tool is held at the seafloor for 5–10 min to thermally equilibrate with bottom water. The lowest temperature recorded in the water column is preferred over the average temperature at the seafloor as an estimate of bottom water temperature because (1) this measurement is more repeatable and (2) the bottom water is expected to have the lowest temperature in the profile. After the APC system penetrates the sediment, it is held in place for ~10 min as the APCT-3 tool records the temperature of the formation at 1 s intervals. When the APC system is hydraulically inserted into the formation, there is typically an instantaneous temperature increase due to frictional heating. This heat gradually dissipates into the surrounding sediment as the temperature at the APCT-3 tool equilibrates toward the temperature of the sediment.

The equilibrium temperature of the sediment is estimated by applying a mathematical heat-conduction model to the temperature decay record (Horai and Von Herzen, 1985). The synthetic thermal decay curve for the APCT-3 tool is a function of the geometry and thermal properties of the probe and the sediment (Bullard, 1954; Horai and Von Herzen, 1985). The equilibrium temperature must be estimated by applying a fitting procedure in the TP-Fit software (Heesemann et al., 2006). However, when the APC system does not achieve a full stroke or when vessel heave pulls the APC system up from full penetration, the temperature equilibration curve is disturbed and temperature determination is less accurate. The nominal accuracy of the APCT-3 tool temperature measurements is $\pm 0.05^\circ\text{C}$. These temperature measurements, combined with measurements of thermal conductivity, were subsequently used to estimate heat flow at each site (see [Thermal conductivity](#)).

11. Age model

Age models for the sedimentary successions of at least one hole at each site were constructed using shipboard paleomagnetic and biostratigraphic age constraints, which were interpreted alongside information from sedimentology, physical properties, and reflection seismic profiles. These age models are considered preliminary because we expect them to be improved by (1) construction of composite depth scales by interhole splicing in some instances, (2) future refinement of paleomagnetic and biostratigraphic data, (3) astronomical tuning of sedimentologic and/or geochemical records, and (4) improved and synthesized interpretation of seismic reflection data and sediment accumulation patterns across the region in light of the drilled sedimentary record. The age models presented here are intended to guide sampling and future research.

For each site, paleomagnetic and biostratigraphic data were collated on a common geologic timescale. The timescale used for Expedition 395 is mostly taken from the GPTS of Ogg (2020), which was published as part of *Geologic Time Scale 2020* (Gradstein et al., 2020). Unfortunately, there are inconsistencies between various chapters in Gradstein et al. (2020), most notably between the GPTS presented by Ogg (2020) and that used in the Neogene timescale of Raffi et al. (2020), but also between both of those chapters and the Quaternary GPTS of Gibbard and Head (2020). For the Pleistocene, Ogg (2020) used calibrations from Channell et al. (2020) for most of the reversal ages between Subchrons C1r.1r and C2r.2r, whereas Raffi et al. (2020) used calibrations from the Geologic Time Scale 2016 (Ogg et al., 2016). For the early to middle Miocene, both Raffi et al. (2020) and Ogg (2020) referenced the orbitally tuned ages of magnetic reversals from Subchron C5Bn.1r to C5Dr.1n from Kochhann et al. (2016). However, only the data tables of Raffi et al. (2020) appear to have been updated to reflect this. For Expedition 395, we follow the GPTS of Ogg (2020) by including the revised Pleistocene reversal ages of Channell et al. (2020). Because of the lack of consistency between chapters in the Gradstein et al. (2020) volume, we avoid the term “Geologic Time Scale 2020” and refer to our paleomagnetic timescale as “Ogg (2020) with modifications from Kochhann et al. (2016).”

The first step in constructing each age model was to compile all available biostratigraphic and paleomagnetic age constraints on an age-depth plot. These points seldom fall on a straight line, which may be because individual age estimates are unreliable for one reason or another (diachrony of biohorizons or poor preservation, for example) or because of changes in sedimentation rate (inflection points) or hiatuses. The age-depth information was therefore considered in light of both sedimentologic information and the site survey seismic reflection data for each site. Sedimentologic descriptions can provide information on sudden lithologic changes or variations in bedding inclination; the presence of event beds such as turbidites or ash bands; and evidence for reworking, bioturbation, slumping, or mixing of sediment. Seismic reflection profiles can indicate lateral pinching out or condensation of strata or changes in the homogeneity of sediment, but they only provide an approximate guide to where in the succession such complexities might be expected. Combining this information, a series of age model tie points was selected. Together, these tie points constitute a preliminary age model for the hole or holes from which it is possible to infer a preliminary age from any sample depth.

Preliminary age models have two main components: (1) a series of interpolations (generally linear) between selected control points and (2) identification of the depth levels of possible hiatuses or zones of mixed sedimentation and/or slumping. Where the paleomagnetic records are clear, unambiguous, and consistent with the biostratigraphic data, each well-defined paleomagnetic reversal was used as a tie point. Biostratigraphic tie points were used mainly in intervals where paleomagnetic data are absent or ambiguous, usually the deeper parts of the holes cored using the XCB or the RCB systems. Only those biohorizons that are both clearly located in the succession and reasonably well calibrated to the geomagnetic polarity reversal record were used as age model tie points.

A list of the estimated depth levels of epoch and subepoch boundaries was made for each site by interpolation between neighboring tie points. The age of the oldest sediment in each hole was estimated so it can be compared with the estimated age of basement inferred from seafloor spreading rates and regional sea-surface magnetic anomaly surveys.

References

- Abrantes, F., Hodell, D.A., Alvarez Zarikian, C.A., Brooks, H.L., Clark, W.B., Dauchy-Tric, L.F.B., dos Santos Rocha, V., Flores, J.-A., Herbert, T.D., Hines, S.K.V., Huang, H.-H.M., Ikeda, H., Kaboth-Bahr, S., Kuroda, J., Link, J.M., McManus, J.F., Mitsunaga, B.A., Nana Yobo, L., Pallone, C.T., Pang, X., Peral, M.Y., Salgueiro, E., Sanchez, S., Verma, K., Wu, J., Xuan, C., and Yu, J., 2024. Expedition 397 methods. In Hodell, D.A., Abrantes, F., Alvarez Zarikian, C.A., and the Expedition 397 Scientists, Iberian Margin Paleoclimate. Proceedings of the International Ocean Discovery Program, 397: College Station, TX (International Ocean Discovery Program). <https://doi.org/10.14379/iodp.proc.397.102.2024>
- Acton, G., Morris, A., Musgrave, R., Zhao, X., and IODP SRM Personnel, 2017. Assessment of the New Superconducting Rock Magnetometer (SRM) on the JOIDES Resolution. http://iodp.tamu.edu/publications/JRSO/SRM_Workshop_2017.pdf
- Acton, G.D., Borton, C.J., and the Leg 178 Shipboard Scientific Party, 2002a. Palmer Deep composite depth scales for Leg 178 sites 1098 and 1099. In Barker, P.F., Camerlenghi, A., Acton, G.D., and Ramsay, A.T.S. (Eds.), Proceedings of the Ocean Drilling Program, Scientific Results. 178: College Station, TX (Ocean Drilling Program), 1–35. <https://doi.org/10.2973/odp.proc.sr.178.202.2001>
- Acton, G.D., Okada, M., Clement, B.M., Lund, S.P., and Williams, T., 2002b. Paleomagnetic overprints in ocean sediment cores and their relationship to shear deformation caused by piston coring. *Journal of Geophysical Research: Solid Earth*, 107:2067–2081. <https://doi.org/10.1029/2001JB000518>
- Agnini, C., Fornaciari, E., Raffi, I., Catanzariti, R., Pälke, H., Backman, J., and Rio, D., 2014. Biozonation and biochronology of Paleogene calcareous nannofossils from low and middle latitudes. *Newsletters on Stratigraphy*, 47(2):131–181. <https://doi.org/10.1127/0078-0421/2014/0042>
- Aksu, A.E., and Kaminski, M.A., 1989. Neogene and Quaternary planktonic foraminifer biostratigraphy and biochronology in Baffin Bay and the Labrador Sea. In Srivastava, S.P., Arthur, M., Clement, B., et al., Proceedings of the Ocean Drilling Program, Scientific Results. 105: College Station, TX (Ocean Drilling Program), 287–304. <https://doi.org/10.2973/odp.proc.sr.105.122.1989>
- Anthonissen, E.D., 2009. A new Pliocene biostratigraphy for the northeastern North Atlantic. *Newsletters on Stratigraphy*, 43/2:91–126.
- Backman, J., Raffi, I., Rio, D., Fornaciari, E., and Pälke, H., 2012. Biozonation and biochronology of Miocene through Pleistocene calcareous nannofossils from low and middle latitudes. *Newsletters on Stratigraphy*, 45(3):221–244. <https://doi.org/10.1127/0078-0421/2012/0022>
- Bartington Instruments, L., 2011. Operation Manual for MS2 Magnetic Susceptibility System: Oxford, UK (Bartington Instruments, Ltd.). <https://gmw.com/wp-content/uploads/2019/03/MS2-OM0408.pdf>
- Baumann, K.-H., and Freitag, T., 2004. Pleistocene fluctuations in the northern Benguela Current system as revealed by coccolith assemblages. Presented at the Calcareous nannofossil palaeoecology and palaeoceanographic reconstructions, Amsterdam, Netherlands. <https://doi.org/10.1016/j.marmicro.2004.04.011>
- Berggren, W.A., Kent, D.V., Swisher, C.C., III, Aubry, M.-P., Berggren, W.A., Kent, D.V., Aubry, M.-P., and Hardenbol, J., 1995. A revised Cenozoic geochronology and chronostratigraphy. In Berggren, W.A., Kent, D.V., Aubry, M.-P., and Hardenbol, J. (Eds.), *Geochronology, Time Scales and Global Stratigraphic Correlation*. SEPM Special Publication, 54. <https://doi.org/10.2110/pec.95.04.0129>
- Blum, P., 1997. Physical properties handbook: a guide to the shipboard measurement of physical properties of deep-sea cores. *Ocean Drilling Program Technical Note*, 26. <https://doi.org/10.2973/odp.tn.26.1997>
- Blum, P., Rhinehart, B., and Acton, G.D., 2020. International Ocean Discovery Program Expedition 384 Preliminary Report. International Ocean Discovery Program. <https://doi.org/10.14379/iodp.pr.384.2020>
- Bown, P.R., and Dunkley Jones, T., 2012. Calcareous nannofossils from the Paleogene equatorial Pacific (IODP Expedition 320 Sites U1331–1334). *Journal of Nannoplankton Research*, 32:3–51.
- Bullard, E.C., 1954. The flow of heat through the floor of the Atlantic Ocean. *Proceedings of the Royal Society of London, A: Mathematical and Physical Sciences*, 222(1150):408–429. <https://doi.org/10.1098/rspa.1954.0085>
- Chaisson, W.P., and Leckie, R.M., 1993. High-resolution Neogene planktonic foraminifer biostratigraphy of Site 806, Ontong Java Plateau (western equatorial Pacific). In Berger, W.H., Kroenke, L.W., Mayer, L.A., et al., Proceedings of the Ocean Drilling Program, Scientific Results. 130: College Station, TX (Ocean Drilling Program), 137–178. <https://doi.org/10.2973/odp.proc.sr.130.010.1993>
- Chaisson, W.P., and Pearson, P.N., 1997. Planktonic foraminifer biostratigraphy at Site 925: middle Miocene–Pleistocene. In Shackleton, N.J., Curry, W.B., Richter, C., and Bralower, T.J. (Eds.), Proceedings of the Ocean Drilling Program, Scientific Results. 154: College Station, TX (Ocean Drilling Program), 3–31. <https://doi.org/10.2973/odp.proc.sr.154.104.1997>
- Channell, J.E.T., Singer, B.S., and Jicha, B.R., 2020. Timing of Quaternary geomagnetic reversals and excursions in volcanic and sedimentary archives. *Quaternary Science Reviews*, 228:106114. <https://doi.org/10.1016/j.quascirev.2019.106114>
- Coggon, R.M., Teagle, D.A.H., Sylvan, J.B., Reece, J., Estes, E.R., Williams, T.J., Christeson, G.L., Aizawa, M., Albers, E., Amadori, C., Belgrano, T.M., Borrelli, C., Bridges, J.D., Carter, E.J., D'Angelo, T., Dinarès-Turell, J., Doi, N., Estep, J.D., Evans, A., Gilhooly, W.P., III, Grant, L.C.J., Guérin, G.M., Harris, M., Hojnacki, V.M., Hong, G., Jin, X., Jonnalagadda, M., Kaplan, M.R., Kempton, P.D., Kuwano, D., Labonte, J.M., Lam, A.R., Latas, M., Lowery, C.M., Lu, W., McIntyre, A., Moal-Darrigade, P., Pekar, S.F., Robustelli Test, C., Routledge, C.M., Ryan, J.G., Santiago Ramos, D., Shchepetkina, A., Slagle, A.L., Takada, M., Tamborrino, L., Villa, A., Wang, Y., Wee, S.Y., Widlansky, S.J., Yang, K., Kurz, W., Prakasam, M., Tian, L., Yu, T., and Zhang, G., 2024. Expedition 390/393 methods. In Coggon, R.M., Teagle, D.A.H., Sylvan, J.B., Reece, J., Estes, E.R., Williams, T.J., Christeson, G.L., and the Expedition 390/393 Sci-

- entists, South Atlantic Transect. Proceedings of the International Ocean Discovery Program, 390/393: College Station, TX (International Ocean Discovery Program). <https://doi.org/10.14379/iodp.proc.390393.102.2024>
- de Kaenel, E., and Villa, G., 1996. Oligocene-Miocene calcareous nannofossil biostratigraphy and paleoecology from the Iberia abyssal plain. In Whitmarsh, R.B., Sawyer, D.S., Klaus, A., and Masson, D.G. (Eds.), Proceedings of the Ocean Drilling Program, Scientific Results. 149: College Station, TX (Ocean Drilling Program). <https://doi.org/10.2973/odp.proc.sr.149.208.1996>
- Dearing, J.A., Dann, R.J.L., Hay, K., Lees, J.A., Loveland, P.J., Maher, B.A., and O'Grady, K., 1996. Frequency-dependent susceptibility measurements of environmental materials. *Geophysical Journal International*, 124(1):228–240. <https://doi.org/10.1111/j.1365-246X.1996.tb06366.x>
- Drury, A.J., Westerhold, T., Hodell, D., and Röhl, U., 2018. Reinforcing the North Atlantic backbone: revision and extension of the composite splice at ODP Site 982. *Climate of the Past*, 14(3):321–338. <https://doi.org/10.5194/cp-14-321-2018>
- Ellis, D.V., and Singer, J.M., 2007. *Well Logging for Earth Scientists* (2nd edition): New York (Elsevier). <https://doi.org/10.1007/978-1-4020-4602-5>
- Evans, H.B., 1965. GRAPE* - A Device For Continuous Determination Of Material Density And Porosity. Presented at the SPWLA 6th Annual Logging Symposium (Volume II).
- Expedition 339 Scientists, 2013. *Methods*. In Stow, D.A.V., Hernández-Molina, F.J., Alvarez Zarikian, C.A., and the Expedition 339 Scientists, Proceedings of the Integrated Ocean Drilling Program. 339: Tokyo (Integrated Ocean Drilling Program Management International, Inc.). <https://doi.org/10.2204/iodp.proc.339.102.2013>
- Flower, B.P., 1999. Data report: planktonic foraminifers from the subpolar North Atlantic and Nordic Seas: Sites 980–987 and 907. In Raymo, M.E., Jansen, E., Blum, P., and Herbert, T.D. (Eds.), Proceedings of the Ocean Drilling Program, Scientific Results. 162: College Station, TX (Ocean Drilling Program). <https://doi.org/10.2973/odp.proc.sr.162.038.1999>
- Fornaciari, E., Backman, J., and Rio, D., 1993. Quantitative distribution patterns of selected Lower to Middle Miocene calcareous nannofossils from the Ontong Java Plateau. In Berger, W.H., Kroenke, L.W., Mayer, L.A., et al., Proceedings of the Ocean Drilling Program, Scientific Results. 130: College Station, TX (Ocean Drilling Program), 245–256. <https://doi.org/10.2973/odp.proc.sr.130.009.1993>
- Fornaciari, E., and Rio, D., 1996. Latest Oligocene to early Middle Miocene quantitative calcareous nannofossil biostratigraphy in the Mediterranean region. *Micropaleontology*, 42(1):1–36. <https://doi.org/10.2307/1485981>
- Gibbard, P.L., and Head, M.J., 2020. The Quaternary period. In Gradstein, F.M., Ogg, J.G., Schmitz, M.D., and Ogg, G.M. (Eds.), *Geologic Time Scale 2020*. Dordrecht, Netherlands (Elsevier), 1217–1255. <https://doi.org/10.1016/B978-0-12-824360-2.00030-9>
- Gieskes, J.M., Gamou, T., and Brumsack, H.J., 1991. Chemical methods for interstitial water analysis aboard JOIDES Resolution. *Ocean Drilling Program Technical Note*, 15. <https://doi.org/10.2973/odp.tn.15.1991>
- Godard, M., Awaji, S., Hansen, H., Hellebrand, E., Brunelli, D., Johnson, K., Yamasaki, T., Maeda, J., Abratis, M., Christie, D., Kato, Y., Mariet, C., and Rosner, M., 2009. Geochemistry of a long in-situ section of intrusive slow-spread oceanic lithosphere: results from IODP Site U1309 (Atlantis Massif, 30°N Mid-Atlantic-Ridge). *Earth and Planetary Science Letters*, 279(1–2):110–122. <https://doi.org/10.1016/j.epsl.2008.12.034>
- Goldberg, D., 1997. The role of downhole measurements in marine geology and geophysics. *Reviews of Geophysics*, 35(3):315–342. <https://doi.org/10.1029/97RG00221>
- Graber, K.K., Pollard, E., Jonasson, B., and Schulte, E. (Eds.), 2002. Overview of Ocean Drilling Program engineering tools and hardware. *Ocean Drilling Program Technical Note*, 31. <https://doi.org/10.2973/odp.tn.31.2002>
- Gradstein, F.M., Ogg, J.G., Schmitz, M.D., and Ogg, G.M. (Eds.), 2020. *The Geologic Time Scale 2020*: Amsterdam (Elsevier BV). <https://doi.org/10.1016/C2020-1-02369-3>
- Hagelberg, T., Shackleton, N., Pisias, N., and the Shipboard Scientific Party, 1992. Development of composite depth sections for Sites 844 through 854. In Mayer, L., Pisias, N., Janecek, T., et al., Proceedings of the Ocean Drilling Program, Initial Reports. 138: College Station, TX (Ocean Drilling Program), 79–85. <https://doi.org/10.2973/odp.proc.ir.138.105.1992>
- Hagelberg, T.K., Pisias, N.G., Shackleton, N.J., Mix, A.C., and Harris, S., 1995. Refinement of a high-resolution, continuous sedimentary section for studying equatorial Pacific Ocean paleoceanography, Leg 138. In Pisias, N.G., Mayer, L.A., Janecek, T.R., Palmer-Julson, A., and van Andel, T.H. (Eds.), Proceedings of the Ocean Drilling Program, Scientific Results. 138: College Station, TX (Ocean Drilling Program). <https://doi.org/10.2973/odp.proc.sr.138.103.1995>
- Harms, J.C., and Choquette, P.W., 1965. Geologic evaluation of a gamma-ray porosity device. Presented at the SPWLA 6th Annual Logging Symposium, Dallas, TX, May 1965.
- Heesemann, M., Villinger, H.W., Tréhu, A.T.F.M., and White, S., 2006. Data report: testing and deployment of the new APCT-3 tool to determine in situ temperatures while piston coring. In Riedel, M., Collett, T.S., Malone, M.J., and the Expedition 311 Scientists, Proceedings of the Integrated Ocean Drilling Program. 311: Washington, DC (Integrated Ocean Drilling Program Management International, Inc.). <https://doi.org/10.2204/iodp.proc.311.108.2006>
- Helm-Clark, C.M., Rodgers, D.W., and Smith, R.P., 2004. Borehole geophysical techniques to define stratigraphy, alteration and aquifers in basalt. *Journal of Applied Geophysics*, 55(1):3–38. <https://doi.org/10.1016/j.jappgeo.2003.06.003>
- Hilgen, F., Aziz, H.A., Bice, D., Iaccarino, S., Krijgsman, W., Kuiper, K., Montanari, A., Raffi, I., Turco, E., and Zachariasse, W.-J., 2005. The global boundary stratotype section and point (GSSP) of the Tortonian Stage (Upper Miocene) at Monte Dei Corvi. *International Union of Geological Sciences*, 28(1):6–17. <https://doi.org/10.18814/epiugs/2005/v28i1/001>

- Hilgen, F.J., Abdul Aziz, H., Krijgsman, W., Raffi, I., and Turco, E., 2003. Integrated stratigraphy and astronomical tuning of the Serravallian and lower Tortonian at Monte dei Corvi (Middle–Upper Miocene, northern Italy). *Palaeogeography, Palaeoclimatology, Palaeoecology*, 199(3):229–264. [https://doi.org/10.1016/S0031-0182\(03\)00505-4](https://doi.org/10.1016/S0031-0182(03)00505-4)
- Horai, K., and Von Herzen, R.P., 1985. Measurement of heat flow on Leg 86 of the Deep Sea Drilling Project. In Heath, G.R., Burckle, L. H., et al., Initial Reports of the Deep Sea Drilling Project. 86: Washington, DC (US Government Printing Office), 759–777. <https://doi.org/10.2973/dsdp.proc.86.135.1985>
- Iaccarino, S., 1985. Mediterranean Miocene and Pliocene planktonic foraminifera. In Bolli, H.M., Saunders, J.B., and Perch-Nielsen, K. (Eds.), *Plankton stratigraphy. 1: New York* (Cambridge University Press).
- Imai, N., Terashima, S., Itoh, S., and Ando, A., 1995. 1994 compilation of analytical data for minor and trace elements in seventeen GSJ geochemical reference samples, “igneous rock series”. *Geostandards Newsletter*, 19(2):135–213. <https://doi.org/10.1111/j.1751-908X.1995.tb00158.x>
- Jochum, K.P., Weis, U., Schwager, B., Stoll, B., Wilson, S.A., Haug, G.H., Andreae, M.O., and Enzweiler, J., 2016. Reference values following ISO guidelines for frequently requested rock reference materials. *Geostandards and Geoanalytical Research*, 40(3):333–350. <https://doi.org/10.1111/j.1751-908X.2015.00392.x>
- Johnston, R., Ryan, J.G. and the Expedition 366 Scientists, 2018. pXRF and ICP-AES characterization of shipboard rocks and sediments; protocols and strategies. In Fryer, P., Wheat, C.G., Williams, T., and the Expedition 366 Scientists, *Proceedings of the International Ocean Discovery Program. 366: College Station, TX* (International Ocean Discovery Program). <https://doi.org/10.14379/iodp.proc.366.110.2018>
- Jutzeler, M., White, J.D.L., Talling, P.J., McCanta, M., Morgan, S., Le Friant, A., and Ishizuka, O., 2014. Coring disturbances in IODP piston cores with implications for offshore record of volcanic events and the Missoula megafloods. *Geochemistry, Geophysics, Geosystems*, 15(9):3572–3590. <https://doi.org/10.1002/2014GC005447>
- Kirschvink, J.L., 1980. The least-squares line and plane and the analysis of palaeomagnetic data. *Geophysical Journal International*, 62(3):699–718. <https://doi.org/10.1111/j.1365-246X.1980.tb02601.x>
- Kochhann, K.G.D., Holbourn, A., Kuhnt, W., Channell, J.E.T., Lyle, M., Shackford, J.K., Wilkens, R.H., and Andersen, N., 2016. Eccentricity pacing of eastern equatorial Pacific carbonate dissolution cycles during the Miocene Climatic Optimum. *Paleoceanography*, 31(9):1176–1192. <https://doi.org/10.1002/2016PA002988>
- Kvenvolden, K.A., and McDonald, T.J., 1986. Organic geochemistry on the *JOIDES Resolution*—an assay. *Ocean Drilling Program Technical Note*, 6. <https://doi.org/10.2973/odp.tn.6.1986>
- Le Maitre, R.W., Steckeisen, A., Zanettin, B., Le Bas, M.J., Bonin, B., and Bateman, P. (Eds.), 2002. *Igneous Rocks: A Classification and Glossary of Terms* (Second edition): Cambridge, UK (Cambridge University Press). <https://doi.org/10.1017/CBO9780511535581>
- Lirer, F., Foresi, L.M., Iaccarino, S.M., Salvatorini, G., Turco, E., Cosentino, C., Sierro, F.J., and Caruso, A., 2019. Mediterranean Neogene planktonic foraminifer biozonation and biochronology. *Earth-Science Reviews*, 196:102869. <https://doi.org/10.1016/j.earscirev.2019.05.013>
- Lofts, J.C., and Bourke, L.T., 1999. The recognition of artefacts from acoustic and resistivity borehole imaging devices. In Lovell, M., Williamson, G., and Harvey, P. (Eds.), *Borehole Imaging: Applications and Case Histories*. Geological Society Special Publication, 159: 59–76. <https://doi.org/10.1144/GSL.SP.1999.159.01.03>
- Lourens, L., Hilgen, F., Shackleton, N.J., Laskar, J., and Wilson, D., 2004. The Neogene period. In Smith, A.G., Gradstein, F.M. and Ogg, J.G., *A Geologic Time Scale 2004*. Cambridge, UK (Cambridge University Press), 409–440. <https://doi.org/10.1017/CBO9780511536045.022>
- Lourens, L.J., Antonarakou, A., Hilgen, F.J., Van Hoof, A.A.M., Vergnaud-Grazzini, C., and Zachariasse, W.J., 1996. Evaluation of the Plio-Pleistocene astronomical timescale. *Paleoceanography*, 11(4):391–413. <https://doi.org/10.1029/96PA01125>
- Lovell, M.A., Harvey, P.K., Brewer, T.S., Williams, C., Jackson, P.D., and Williamson, G., 1998. Application of FMS images in the Ocean Drilling Program: an overview. In Cramp, A., MacLeod, C.J., Lee, S.V., and Jones, E.J.W. (Eds.), *Geological Evolution of Ocean Basins: Results from the Ocean Drilling Program*. Geological Society, London, Special Publication, 131: 287–303. <https://doi.org/10.1144/GSL.SP.1998.131.01.18>
- Lurcock, P.C., and Florindo, F., 2019. New developments in the PuffinPlot paleomagnetic data analysis program. *Geochemistry, Geophysics, Geosystems*, 20(11):5578–5587. <https://doi.org/10.1029/2019GC008537>
- Manheim, F.T., and Sayles, F.L., 1974. Composition and origin of interstitial waters of marine sediments, based on deep sea drill cores. In Goldberg, E.D., *The Sea* (Volume 5): *Marine Chemistry: The Sedimentary Cycle*. New York (Wiley), 527–568. <http://pubs.er.usgs.gov/publication/70207491>
- Marsaglia, K., Milliken, K., and Doran, L., 2013. IODP digital reference for smear slide analysis of marine mud, Part 1: Methodology and atlas of siliciclastic and volcanogenic components. *Integrated Ocean Drilling Program Technical Note*, 1. <https://doi.org/10.2204/iodp.tn.1.2013>
- Marsaglia, K., Milliken, K., Leckie, R., Tentori, D., and Doran, L., 2015. IODP smear slide digital reference for sediment analysis of marine mud, Part 2: Methodology and atlas of biogenic components. *Integrated Ocean Drilling Program Technical Note*, 2. <https://doi.org/10.2204/iodp.tn.2.2015>
- Martini, E., 1971. Standard Tertiary and Quaternary calcareous nannoplankton zonation. *Proceedings of the Second Planktonic Conference, Roma*, 1970:739–785.
- Murray, R.W., Miller, D.J., and Kryc, K.A., 2000. Analysis of major and trace elements in rocks, sediments, and interstitial waters by inductively coupled plasma–atomic emission spectrometry (ICP–AES). *Ocean Drilling Program Technical Note*, 29. <https://doi.org/10.2973/odp.tn.29.2000>
- Ogg, J.G., 2020. *Geomagnetic Polarity Time Scale*. In Gradstein, F.M., Ogg, J.G., Schmitz, M., and Ogg, G. (Eds.), *Geologic Time Scale 2020*. Amsterdam (Elsevier), 159–192. <https://doi.org/10.1016/B978-0-12-824360-2.00005-X>
- Ogg, J.G., Ogg, G.M., and Gradstein, F.M., 2016. *A Concise Geologic Time Scale 2016*: New York (Elsevier).

- Okada, H., and Bukry, D., 1980. Supplementary modification and introduction of code numbers to the low-latitude coccolith biostratigraphic zonation (Bukry, 1973; 1975). *Marine Micropaleontology*, 5(3):321–325. [https://doi.org/10.1016/0377-8398\(80\)90016-X](https://doi.org/10.1016/0377-8398(80)90016-X)
- Olafsson, G., 1992. Oligocene/Miocene morphometric variability of the *Cyclargolithus* group from the equatorial Atlantic and Indian Oceans. *Memorie di Scienze Geologiche*, 43:283–295.
- Parnell-Turner, R., Briais, A., and LeVay, L.J., 2023. Expedition 395 Scientific Prospectus Addendum: Reykjanes Mantle Convection and Climate. International Ocean Discovery Program. <https://doi.org/10.14379/iodp.sp.395add.2023>
- Parnell-Turner, R., Briais, A., and LeVay, L., 2020. Expedition 395 Scientific Prospectus: Reykjanes Mantle Convection and Climate. International Ocean Discovery Program. <https://doi.org/10.14379/iodp.sp.395.2020>
- Parnell-Turner, R.E., Briais, A., LeVay, L.J., and the Expedition 395 Scientists, 2025. Supplementary material, <https://doi.org/10.14379/iodp.proc.395supp.2025>. In Parnell-Turner, R.E., Briais, A., LeVay, L.J., and the Expedition 395 Scientists, Reykjanes Mantle Convection and Climate. Proceedings of the International Ocean Discovery Program, 395: College Station, TX (International Ocean Discovery Program).
- Parnell-Turner, R.E., Briais, A., LeVay, L.J., Cui, Y., Di Chiara, A., Dodd, J.P., Dunkley Jones, T., Dwyer, D., Eason, D.E., Friedman, S.A., Hemming, S.R., Hochmuth, K., Ibrahim, H., Jasper, C., Karatsolis, B.T., Lee, S., LeBlanc, D.E., Lindsay, M.R., McNamara, D.D., Modestou, S.E., Murton, B., OConnell, S., Pasquet, G.T., Pearson, P.N., Qian, S.P., Rosenthal, Y., Satolli, S., Sinnesael, M., Suzuki, T., Thulasi Doss, T., White, N.J., Wu, T., Yang Yang, A., dos Santos Rocha, V., Pearman, C., and Tian, C.Y., 2025. Expedition 395 summary. In Parnell-Turner, R.E., Briais, A., LeVay, L.J., and the Expedition 395 Scientists, Reykjanes Mantle Convection and Climate. Proceedings of the International Ocean Discovery Program, 395: College Station, TX (International Ocean Discovery Program). <https://doi.org/10.14379/iodp.proc.395.101.2025>
- Pasini, G., and Colalongo, M.L., 2004. The Pliocene-Pleistocene boundary-stratotype at Vrica, Italy. In Van Couvering, J., *The Pleistocene Boundary and the Beginning of the Quaternary Cambridge* (Cambridge University Press), 15–46.
- Pearson, P.N., and Chaisson, W.P., 1997. Late Paleocene to Middle Miocene planktonic foraminifer biostratigraphy of the Ceara Rise. In Shackleton, N.J., Curry, W.B., Richter, C., and Bralower, T.J. (Eds.), *Proceedings of the Ocean Drilling Program, Scientific Results. 154: College Station, TX (Ocean Drilling Program)*, 33–68. <https://doi.org/10.2973/odp.proc.sr.154.106.1997>
- Perch-Nielsen, K., 1985. Cenozoic calcareous nannofossils. In Bolli, H.M., Saunders, J.B., and Perch-Nielsen, K. (Eds.), *Plankton Stratigraphy (Volume 1)*. Cambridge, UK (Cambridge University Press), 427–554.
- Pimmel, A., and Claypool, G., 2001. Introduction to shipboard organic geochemistry on the JOIDES Resolution. *Ocean Drilling Program Technical Note*, 30. <https://doi.org/10.2973/odp.tn.30.2001>
- Poore, R.Z., 1979. Oligocene through Quaternary planktonic foraminiferal biostratigraphy of the North Atlantic: DSDP Leg 49. In Luyendyk, B.P., Cann, J.R., et al., *Initial Reports of the Deep Sea Drilling Project. 49: Washington, DC (US Government Printing Office)*, 447–517. <https://doi.org/10.2973/dsdp.proc.49.115.1979>
- Poore, R.Z., and Berggren, W.A., 1975. Late Cenozoic planktonic foraminiferal biostratigraphy and paleoclimatology of Hatton-Rockall Basin; DSDP Site 116. *Journal of Foraminiferal Research*, 5(4):270–293. <https://doi.org/10.2113/gsjfr.5.4.270>
- Raffi, I., Backman, J., Fornaciari, E., Pälike, H., Rio, D., Lourens, L., and Hilgen, F., 2006. A review of calcareous nannofossil astrobiochronology encompassing the past 25 million years. *Quaternary Science Reviews*, 25(23):3113–3137. <https://doi.org/10.1016/j.quascirev.2006.07.007>
- Raffi, I., Wade, B.S., Pälike, H., Beu, A.G., Cooper, R., Crundwell, M.P., Krijgsman, W., Moore, T., Raine, I., Sardella, R., and Vernyhorova, Y.V., 2020. The Neogene Period. In Gradstein, F.M., Ogg, J.G., Schmitz, M.D., and Ogg, G. (Eds.), *Geologic Time Scale 2020*. (Elsevier), 1141–1215. <https://doi.org/10.1016/B978-0-12-824360-2.00029-2>
- Reagan, M.K., Pearce, J.A., Petronotis, K., Almeev, R., Avery, A.A., Carvallo, C., Chapman, T., Christeson, G.L., Ferré, E.C., Godard, M., Heaton, D.E., Kirchenbaur, M., Kurz, W., Kutterolf, S., Li, H.Y., Li, Y., Michibayashi, K., Morgan, S., Nelson, W.R., Prytulak, J., Python, M., Robertson, A.H.F., Ryan, J.G., Sager, W.W., Sakuyama, T., Shervais, J.W., Shimizu, K., and Whattam, S.A., 2015. Expedition 352 methods. In Reagan, M.K., Pearce, J.A., Petronotis, K., and the Expedition 352 Scientists, Izu-Bonin-Mariana Fore Arc. Proceedings of the International Ocean Discovery Program, 352: College Station, TX (International Ocean Discovery Program). <https://doi.org/10.14379/iodp.proc.352.102.2015>
- Richter, C., Acton, G., Endris, C., and Radsted, M., 2007. Handbook for shipboard paleomagnetists. *Ocean Drilling Program Technical Note*, 34. <https://doi.org/10.2973/odp.tn.34.2007>
- Rider, M.H., 1996. *The Geological Interpretation of Well Logs (Second edition)*: Houston, TX (Gulf Publishing Company).
- Rio, D., Raffi, I., and Villa, G., 1990. Pliocene-Pleistocene calcareous nannofossil distribution patterns in the western Mediterranean. In Kastens, K.A., Mascle, J., et al., *Proceedings of the Ocean Drilling Program, Scientific Results. 107: College Station, TX (Ocean Drilling Program)*, 513–533. <https://doi.org/10.2973/odp.proc.sr.107.164.1990>
- Rio, D., Sprovieri, R., and Raffi, I., 1984. Calcareous plankton biostratigraphy and biochronology of the Pliocene-Lower Pleistocene succession of the Capo Rossello area, Sicily. *Marine Micropaleontology*, 9(2):135–180. [https://doi.org/10.1016/0377-8398\(84\)90008-2](https://doi.org/10.1016/0377-8398(84)90008-2)
- Rosenthal, Y., Holbourn, A.E., Kulhanek, D.K., Aiello, I.W., Babila, T.L., Bayon, G., Beaufort, L., Bova, S.C., Chun, J.-H., Haowen, D., Drury, A.J., Dunkley Jones, T., Eichler, P.P.B., Fernando, A.G.S., Gibson, K.A., Hatfield, R.G., Johnson, D.L., Kumagai, Y., Tiegang, L., Linsley, B.K., Meinicke, N., Mountain, G.S., Opdyke, B.N., Pearson, P.N., Poole, C.R., Ravelo, A.C., Sagawa, T., Schmitt, A., Wurtzel, J.B., Jian, X., Yamamoto, M., and Zhang, Y.G., 2018. Expedition 363 methods. In Rosenthal, Y., Holbourn, A.E., Kulhanek, D.K., and the Expedition 363 Scientists, Western Pacific

- Warm Pool. Proceedings of the International Ocean Discovery Program, 363: College Station, TX (International Ocean Discovery Program). <https://doi.org/10.14379/iodp.proc.363.102.2018>
- Rothwell, R.G., 1989. Minerals and Mineraloids in Marine Sediments: An Optical Identification Guide: London (Elsevier). <https://doi.org/10.1007/978-94-009-1133-8>
- Ruddiman, W.F., Kidd, R.B., Baldauf, J.G., Clement, B.M., Dolan, J.F., Eggers, M.R., Hill, P.R., Keigwin, L.D., Jr., Mitchell, M., Philipps, I., Robinson, F., Salehipour, S.A., Takayama, T., Thomas, E., Unsold, G., and Weaver, P.P.E., 1987. Initial Reports of the Deep Sea Drilling Project, 94: Washington, DC (US Government Printing Office). <https://doi.org/10.2973/dsdp.proc.94.1987>
- Ryan, J.G., Shervais, J.W., Li, Y., Reagan, M.K., Li, H.Y., Heaton, D., Godard, M., Kirchenbaur, M., Whattam, S.A., Pearce, J.A., Chapman, T., Nelson, W., Prytulak, J., Shimizu, K., and Petronotis, K., 2017. Application of a handheld X-ray fluorescence spectrometer for real-time, high-density quantitative analysis of drilled igneous rocks and sediments during IODP Expedition 352. *Chemical Geology*, 451:55–66. <https://doi.org/10.1016/j.chemgeo.2017.01.007>
- Schlumberger, 1989. Log Interpretation Principles/Applications, SMP-7017: Houston (Schlumberger Education Services).
- Schlumberger, 1994. IPL Integrated Porosity Lithology, SMP-9270: Houston (Schlumberger Education Services).
- Serra, O., 1984. Fundamentals of Well-log Interpretation (Volume 1): The Acquisition of Logging Data: Amsterdam (Elsevier).
- Serra, O., 1986. Fundamentals of Well-Log Interpretation (Volume 2): The Interpretation of Logging Data: Amsterdam (Elsevier).
- Serra, O., 1989. Formation MicroScanner Image Interpretation, SMP-7028: Houston (Schlumberger Education Services).
- Shipboard Scientific Party, 1987. Site 646. In Srivastava, S.P., Arthur, M., Clement, B., et al., Proceedings of the Ocean Drilling Program, Initial Reports. 105: College Station, TX (Ocean Drilling Program), 419–674. <https://doi.org/10.2973/odp.proc.ir.105.105.1987>
- Shipboard Scientific Party, 2003. Leg 202 summary. In Mix, A.C., Tiedemann, R., Blum, P., et al., Proceedings of the Ocean Drilling Program, Initial Reports. 202: College Station, TX (Ocean Drilling Program). <https://doi.org/10.2973/odp.proc.ir.202.101.2003>
- Sierro, F.J., Hernandez-Almeida, I., Alonso-Garcia, M., and Flores, J.A., 2009. Data report: Pliocene-Pleistocene planktonic foraminifer bioevents at IODP Site U1313. In Channell, J.E.T., Kanamatsu, T., Sato, T., Stein, R., Alvarez Zarikian, C.A., Malone, M.J., and the Expedition 303/306 Scientists, Proceedings of the Integrated Ocean Drilling Program. 303/306: College Station, TX (Integrated Ocean Drilling Program Management International, Inc.). <https://doi.org/10.2204/iodp.proc.303306.205.2009>
- Sissingh, W., 1977. Biostratigraphy of Cretaceous calcareous nannoplankton. *Geologie en Mijnbouw*, 56:37–65.
- Speijer, R.P., Pälke, H., Hollis, C.J., Hooker, J.J., and Ogg, J.G., 2020. The Paleogene Period. In Gradstein, F.M., Ogg, J.G., Schmitz, M., and Ogg, G. (Eds.), *Geologic Time Scale 2020*. (Elsevier), 1087–1140. <https://doi.org/10.1016/B978-0-12-824360-2.00028-0>
- Spiegler, D., 1999. Bolboforma biostratigraphy from the Hatton-Rockall Basin (North Atlantic). In Raymo, M.E., Jansen, E., Blum, P., and Herbert, T.D., Proceedings of the Ocean Drilling Program, Scientific Results, 162. College Station, TX (Ocean Drilling Program), 35–49. <https://doi.org/10.2973/odp.proc.sr.162.013.1999>
- Spiegler, D., and Jansen, E., 1989. Planktonic foraminifer biostratigraphy of Norwegian Sea sediments: ODP Leg 104. In Eldholm, O., Thiede, J., Taylor, E., et al., Proceedings of the Ocean Drilling Program, Scientific Results. 104: College Station, TX (Ocean Drilling Program), 681–696. <https://doi.org/10.2973/odp.proc.sr.104.157.1989>
- Spiegler, D., and Spezzaferri, S., 2005. Bolboforma — an overview. *Paläontologische Zeitschrift*, 79(1):167–181. <https://doi.org/10.1007/BF03021760>
- Sun, Z., Jian, Z., Stock, J.M., Larsen, H.C., Klaus, A., Alvarez Zarikian, C.A., Boaga, J., Bowden, S.A., Briais, A., Chen, Y., Cukur, D., Dadd, K.A., Ding, W., Dorais, M.J., Ferré, E.C., Ferreira, F., Furusawa, A., Gewecke, A.J., Hinojosa, J.L., Höfig, T.W., Hsiung, K.-H., Huang, B., Huang, E., Huang, X.-L., Jiang, S., Jin, H., Johnson, B.G., Kurzwski, R.M., Lei, C., Li, B., Li, L., Li, Y., Lin, J., Liu, C., Liu, C., Liu, Z., Luna, A., Lupi, C., McCarthy, A.J., Mohn, G., Ningthoujam, L.S., Nirrengarten, M., Osono, N., Peate, D.W., Persaud, P., Qiu, N., Robinson, C.M., Satolli, S., Sauerlich, I., Schindlbeck, J.C., Skinner, S.M., Straub, S.M., Su, X., Tian, L., Van der Zwan, F.M., Wan, S., Wu, H., Xiang, R., Yadav, R., Yi, L., Zhang, C., Zhang, J., Zhang, Y., Zhao, N., Zhong, G., and Zhong, L., 2018. Expedition 367/368 methods. In Sun, Z., Jian, Z., Stock, J.M., Larsen, H.C., Klaus, A., Alvarez Zarikian, C.A., and the Expedition 367/368 Scientists, South China Sea Rifted Margin. Proceedings of the International Ocean Discovery Program, 367/368: College Station, TX (International Ocean Discovery Program). <https://doi.org/10.14379/iodp.proc.367368.102.2018>
- Teske, A., Lizarralde, D., Höfig, T.W., Aiello, I.W., Ash, J.L., Bojanova, D.P., Buatier, M.D., Edgcomb, V.P., Galerne, C.Y., Gontharet, S., Heuer, V.B., Jiang, S., Kars, M.A.C., Khogekumar Singh, S., Kim, J.-H., Koornneef, L.M.T., Marsaglia, K.M., Meyer, N.R., Morono, Y., Negrete-Aranda, R., Neumann, F., Pastor, L.C., Peña-Salinas, M.E., Pérez Cruz, L.L., Ran, L., Riboulleau, A., Sarao, J.A., Schubert, F., Stock, J.M., Toffin, L.M.A.A., Xie, W., Yamanaka, T., and Zhuang, G., 2021. Expedition 385 methods. In Teske, A., Lizarralde, D., Höfig, T.W., and the Expedition 385 Scientists, Guaymas Basin Tectonics and Biosphere. Proceedings of the International Ocean Discovery Program, 385: College Station, TX (International Ocean Discovery Program). <https://doi.org/10.14379/iodp.proc.385.102.2021>
- van Sprang, H.A., 2000. Fundamental parameter methods in XRF spectroscopy. In Blanton, T., Brehm, L., and Schmelting, M. (Eds.), *JCPDS-International Centre for Diffraction Data 2000. Advances in X-ray Analysis*, 42: 1–10.

- Von Herzen, R., and Maxwell, A.E., 1959. The measurement of thermal conductivity of deep-sea sediments by a needle-probe method. *Journal of Geophysical Research*, 64(10):1557–1563.
<https://doi.org/10.1029/JZ064i010p01557>
- Wade, B.S., Pearson, P.N., Berggren, W.A., and Pälike, H., 2011. Review and revision of Cenozoic tropical planktonic foraminiferal biostratigraphy and calibration to the geomagnetic polarity and astronomical time scale. *Earth-Science Reviews*, 104(1–3):111–142. <https://doi.org/10.1016/j.earscirev.2010.09.003>
- Weaver, P.P.E., 1987. Late Miocene to recent planktonic foraminifers from the North Atlantic: Deep Sea Drilling Project Leg 94. In Ruddiman, W.F., Kidd, R. B., Thomas, E., et al., Initial Reports of the Deep Sea Drilling Project. 94: Washington, DC (US Government Printing Office), 703–727. <https://doi.org/10.2973/dsdp.proc.94.114.1987>
- Weaver, P.P.E., and Clement, B.M., 1986. Synchronicity of Pliocene planktonic foraminiferal datums in the North Atlantic. *Marine Micropaleontology*, 10(4):295–307. [https://doi.org/10.1016/0377-8398\(86\)90033-2](https://doi.org/10.1016/0377-8398(86)90033-2)
- Weaver, P.P.E., and Clement, B.M., 1987. Magnetobiostratigraphy of planktonic foraminiferal datums: Deep Sea Drilling Project Leg 94, North Atlantic. In Ruddiman, W.R., Kidd, R. B., Thomas, E., et al., Initial Reports of the Deep Sea Drilling Project. 94: Washington, DC (US Government Printing Office), 815–829.
<https://doi.org/10.2973/dsdp.proc.94.120.1987>
- Wei, W., 1991. Evidence for an earliest Oligocene abrupt cooling in the surface waters of the Southern Ocean. *Geology*, 19(8):780–783. [https://doi.org/10.1130/0091-7613\(1991\)019<0780:EFAEOA>2.3.CO;2](https://doi.org/10.1130/0091-7613(1991)019<0780:EFAEOA>2.3.CO;2)
- Wei, W., and Wise, S.W., 1989. Paleogene calcareous nannofossil magnetobiochronology: results from South Atlantic DSDP Site 516. *Marine Micropaleontology*, 14(1):119–152. [https://doi.org/10.1016/0377-8398\(89\)90034-0](https://doi.org/10.1016/0377-8398(89)90034-0)
- Wentworth, C.K., 1922. A scale of grade and class terms for clastic sediments. *The Journal of Geology*, 30(5):377–392.
<https://doi.org/10.1086/622910>
- White, J.D.L., McPhie, J., and Skilling, I., 2000. Peperite: a useful genetic term. *Bulletin of Volcanology*, 62:65–66.
<https://doi.org/10.1007/s004450050293>
- Young, J.R., 1998. Neogene. In Bown, P.R., *Calcareous Nannofossil Biostratigraphy*. Dordrecht, Netherlands (Kluwer Academic Publishing), 225–265.
- Young, J.R., and Bown, P.R., 2014. Some emendments to calcareous nannoplankton taxonomy. *Journal of Nannoplankton Research*, 33(1):39–46.
- Zijderveld, J.D.A., 1967. AC demagnetization of rocks: analysis of results. In Runcorn, S.K.C., Creer, K.M., and Collinson, D.W. (Eds.), *Methods in Palaeomagnetism. Developments in Solid Earth Geophysics*, 3: 254–286.
<https://doi.org/10.1016/B978-1-4832-2894-5.50049-5>